



UNIVERSITA' DEGLI STUDI DI
NAPOLI FEDERICO II

Scuola Politecnica e delle Scienze di Base
Department of Chemical, Materials and Industrial Production Engineering

XXXV° Ph.D. Programme in:
Industrial Products and Processes Engineering

Ph.D. Thesis

**Micro-mechanical CFRP Interface
Characterization via an Original
Numerical-Experimental Approach**

Ph.D. Supervisors

Ch.mo Prof. Luigi Carrino

Ch.mo Prof. Luca Esposito

Ph.D Course Coordinator

Ch.mo Prof. Andrea D'Anna

Ph.D. Student

Ing. Matteo Bruno

Academic Year 2021/2022

*Chi nun tene coraggio,
nun se cocca ch'e femmene belle.*

- Neapolitan proverb -

Contents

1	Introduction	4
1.1	Composite materials in the field of industry	4
1.2	Fibre reinforced polymers	7
1.3	Certification and testing	12
1.4	Multiscale numerical tools	14
1.5	UD FRP composites failure mechanisms	16
1.6	Fibre-matrix interface in composite	19
	1.6.1 Interface and interphase definition	19
	1.6.2 Interface testing methods	20
	1.6.3 Role of interface in damage mechanisms	28
1.7	Motivation and objectives of the work	33
1.8	Dissertation structure	34
2	Experimental Methods	36
2.1	Micro-cantilever test introduction	36
2.2	Material	39
2.3	Specimens design and manufacturing	40
2.4	Testing mode	46
3	Experimental Results	50
3.1	Mode I test results	50
3.2	Matrix carved specimens results	56

3.3	Mode II test results	58
4	Computational Methods	64
4.1	Introduction	64
4.2	Numerical model	65
4.3	Cohesive zone model	67
4.3.1	Contact detection	67
4.3.2	Contact pairing algorithms	69
4.3.3	Cohesive model theoretical approach	70
4.3.4	Cohesive model definition	78
5	Computational Results	80
5.1	Numerical model validation	80
5.1.1	Boundaries condition verification	80
5.1.2	Material properties verification	82
5.1.3	Indenter positioning uncertainty effect	84
5.2	Interface properties identification	88
5.3	Damage modes contribution	92
5.4	Effect of friction	98
6	Analytical Method	102
6.1	Theoretical approach	102
6.1.1	Beam deformation field	103
6.1.2	Analytical solution adaptability	107
6.2	Theory applicability	109
6.2.1	Timoshenko Beam consistency	109
6.2.2	Adapted solution calibration	110
6.3	Interface strength calculation	112
6.4	Interface toughness tracing	113
6.4.1	Griffith theory	113
6.4.2	Energy release rate definition	116
6.4.3	Energy release rate calculation	117

7	Analytical Results	120
7.1	Elastic solution validation	120
7.2	Interface strength determination	122
7.3	Toughness calculation	123
7.3.1	Compliance vs debonded length relation	123
7.3.2	Resistance curve definition	124
8	Conclusions and future work	128
8.1	Achievements	128
8.2	Conclusions	129
8.3	Future work	130

Acronyms

AFM	atomic force microscope
BK	Benzeggagh-Kenane
CFRP	carbon-fibre reinforced polymer
CZM	cohesive zone model
FEA	finite element analysis
FEM	finite element model
FIB	focused ion beam
FRP	fibre reinforced polymers
GFRP	glass-fibre reinforced polymer
GLT	global load transfer
HM	high modulus
HS	high strength
MCT	micro-cantilever test
RVE	representative volume element
SEM	scanning electron microscope
UD	unidirectional

Abstract

Fibre to matrix interface properties play a fundamental role in fiber reinforced polymers damage mechanisms, contributing to the complexity of composite materials failure prediction. In the present dissertation an original micro-mechanical experimental approach, based on micro-cantilever tests, was proposed for the in-situ interface testing. The adoption of computational models, supporting the experimental campaign evidences, allowed the interface properties identification. The proposed computational models were first validated on the base of the experimental results and thus adopted to investigate the interface debonding behaviour as well as the experimental method consistency in isolate both the opening (mode I) and sliding (mode II) damage mode. An analytical approach, describing the deformation behaviour of the micro-cantilever specimens, was concurrently developed. It represented the base for the development of a leaner combined experimental-analytical approach for the interface properties identification. Its application to the experimental campaign evidences provided results perfectly in line with those numerically retrieved.

Acknowledgement

In primo luogo, ci tengo a ringraziare i miei supervisori: il Prof. Luca Esposito per essere stato un supporto costante sia scientificamente che umanamente durante questo percorso; ed il Prof. Luigi Carrino per aver reso possibile il mio dottorato e creduto nelle potenzialità di questa attività.

I would also like to thank the IMDEA materials institute sincerely, particularly in the person of Prof. Carlos Gonzalez, for making this project possible and always encouraging me in my work. Dr. Davide Mocerino for his sincere friendship, for sharing his enthusiasm in the work and for involving me in this research. My thanks also include Dr Miguel Monclus and Dr Manuel Avella for their support during the experimental activities.

Ringrazio poi tutto il gruppo di costruzione di macchine della Federico II, i Professori Armentani, Perrella, Cricrì, Pucillo e Penta che quotidianamente hanno contribuito alla mia formazione professionale e personale con un consiglio, una parola di sprone o semplicemente condividendo un piatto di pasta. Grazie per l'anarchico rigore del nostro lavoro. Non posso poi non spendere qualche parola per i colleghi ed amici tutti del DICMaPI. In particolare, ringrazio il Dr Antonio Viscusi per essere stato una guida in questo percorso e per avermi sempre parato il c**o.

Se siete giunti a leggere queste righe è però altrettanto merito dei miei genitori, che mi hanno sempre spronato ad andare avanti, anche quando non si capiva bene dove si stesse andando, e della mia ragazza che è stata capace di sopportare molto e condividere con sincero entusiasmo la mia scelta di vita.

A tutti voi, sinceramente grazie!

Chapter 1

Introduction

1.1 Composite materials in the field of industry

The term *composite* refers to a wide range of materials, consisting of two or more components, whose coexistence gives the resulting material special properties not present in the components when taken individually [1]. Generally, one of the two components has a reinforcing function and therefore has strong mechanical properties with the purpose of ensuring stiffness and strength to the material. One of the other constituents is a material that can enclose the reinforcement, give shape to the artefact and ensure the distribution of stresses so that the material behaves as a whole. This component is called the Matrix. Various composite materials exist in nature, for example the wood is derived from the union of lignin (reinforcement) with cellulose (matrix). Many composites are also normally adopted in construction since the early stage of humankind. From mud and straw bricks, where the straw works as a binder and the mud gives the necessary strength in compression, to reinforced concrete, which is the result of combining concrete (matrix) and iron rods (reinforcements). The properties of a composite material depend on the constituents properties, geom-

etry and phase distribution. One of the most important parameters is the reinforcement volume or weight fraction. The distribution of the reinforcement determines the characteristics of the system. The less uniform the reinforcement, the more heterogeneous the material and the higher the probability of failure in weaker areas. The geometry and orientation of the reinforcement, on the other hand, influence the anisotropy of the system. The composite phases have different roles depending on the type and application of the composite. In the case of low to medium performance composites, the reinforcement, usually short fibres or particles, gives some stiffening but only locally reinforces the material. The matrix on the other hand, is the main constituent to support loads and defines the mechanical properties of the material. In the case of high-performance structural composites, the reinforcement is normally continuous and forms the skeleton of the material, determining stiffness and strength in the reinforcement direction. The matrix phase provides protection, support for the reinforcement and the transfer of local stresses. The interface, although small in size, can play an important role in controlling the fracture mechanism, fracture toughness and, above all, the stress-strain behaviour of the material.

In the modern era the high performance structural components are typically made by a polymeric matrix and a reinforcement in form of continuous fibres. From an historical point of view, the concept of fibre reinforcement is very old. There are even references in the Bible to reinforcing bricks with straw in ancient Egypt. Iron bars were used to reinforce masonry in the 19th century and this led to the development of reinforced concrete. However, to have the first example of a composite polymer in the modern era, we will have to wait for the first fibreglass boat built in 1942, at the same time that fibre reinforced polymers (FRP) found use in aeronautics and electrical components. In the early 1960s, the application of advanced composites for military aircraft components began with the introduction of the first high-strength boron and carbon fibres. Since the late 1970s, the

applications of polymer composites have greatly expanded in the fields of aeronautics, automotive and biomedical applications, as graphically reported in Figure 1.1.

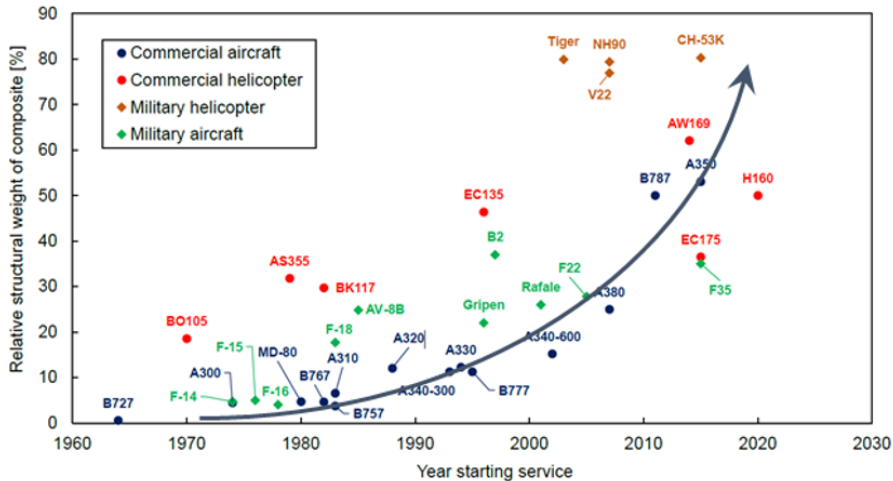


Figure 1.1: Evolution of structural composite materials applications in commercial and military aircraft and rotorcraft [2].

The example of the application of composite materials that signified a radical technological discontinuity is the *Boeing 787 Dreamliner* aircraft (the first airliner flew in 2013) in which composite materials are also used extensively in the primary structures (around 50 per cent), enabling a weight saving of more than 20 per cent. The continuous technological evolution that has made it possible to create innovative composite materials with increasingly high-performance characteristics and the growing sensitivity of the market to energy saving, have made polymer matrix composites particularly versatile and suitable for various applications. As mentioned, due to their limited size, the fibres have an uncommon structural perfection; this feature, combined with the intrinsic properties of the constituent materials, ensures high mechanical strength, a very high elastic modulus, a very low specific weight, and linear elastic behaviour up to fracture. The most important fibres for use in composites can be glass, carbon, organic like linen

and hemp or mineral like basalt. They are found in composites either in the form of continuous fibres arranged parallel in a plane, or in the form of chopped fibres arranged with random orientation or, finally, they can be woven in a weft-ordered configuration and arranged in a plane. For high-end applications requiring high strength and stiffness composite laminates made by stacking several unidirectional (UD) plies are still the reference configuration. Fibres diameter are usually in the order of $5 \div 20\mu m$, plies thickness is in the range of $100 \div 300\mu m$ and the whole laminate has a thickness greater than several millimeters. Due to the thousands of fibres arranged in the same direction the single plies results highly anisotropic. Benefiting from this, the properties of the final laminate, depending on the stacking sequence of the individual plies, can be tailored in order to fulfill the desired properties. For a long time, the most commonly used fibres in structural composite applications were glass fibres. Although they have good strength and low density characteristics, they have a relatively low modulus of elasticity. For this reason, about 25 years ago, experiments began and organic composites were converted into carbon and graphite fibres and fabrics.

1.2 Fibre reinforced polymers

The high mechanical properties of carbon fibres derive from the special crystalline structure of graphite. The more arranged the crystal structure, the higher the material's properties. A graphite crystal has a structure composed of overlapping layers of planes made up of carbon atoms. The bonds between the same atoms in the same plane are strong (covalent bonds) while those between atoms in different planes are relatively weak (Van der Waals bonds). It is evident that crystals are strongly anisotropic structures and it will be the task of the manufacturing process to arrange the crystal structure in the desired direction. Of course, this is not easy so it is practically never possible

to obtain perfect crystals and precise orientation. Therefore, the resulting mechanical properties will be lower than the theoretical ones. Carbon fibres are obtained by graphitization organic textile fibres of rayon or polyacrylonitrile in an inert atmosphere at over 2000°C. The starting fibres are called precursors. During the graphitization process, the high heat and the state of tension to which the material is subjected cause the distortion of the crystalline structure and the disruption of its planarity. The resulting micro-domains tend to join, fold, twist, and split with each other. Therefore, the internal structure of carbon fibres is not purely homogeneous but it consists of various chaotic micro-domains from by the structural units [3]. The greater the tensile stress exerted, the higher the Young’s modulus of the product. On the other hand, the increase in modulus is balanced by a decrease in strength. Thus, there are both high-modulus carbon fibres, penalised in strength, and low-modulus, high-strength carbon fibres on the market. The two types are called high modulus (HM) and high strength (HS) respectively.

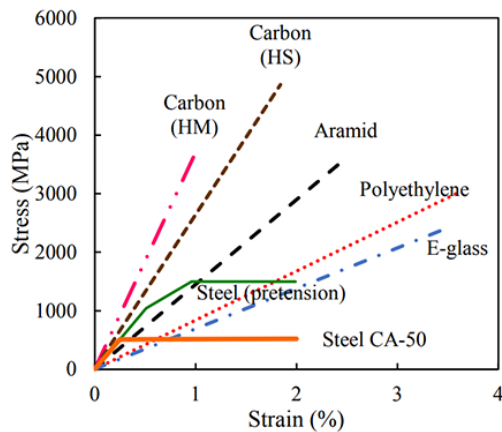


Figure 1.2: Comparison of stress-strain curves for the most common reinforcement fibres and steels with HS and HM carbon fibres [3].

A comparison of the stress-strain curves for HS and HM carbon fibres with other varieties of fibres (Aramid, E-glass, Polyethylene) and steels is shown in Figure 1.2. Compared to other types of fibres, carbon

fibres have three substantial advantages: a very high elastic modulus, a low density and a very low coefficient of thermal expansion. They are therefore supplanting the other fibres in all those fields where, in addition to low weight, high rigidity is required (aeronautical structures, sports equipment, etc.) or considerable dimensional stability under temperature variations (optical devices, radar, etc.). The production costs of carbon fibres are considerably higher than those of glass fibres, but their widespread use is justified by their high mechanical properties. As mentioned, polymer matrices have the function of wrapping and protecting reinforcing fibres, transforming them from the initial form of textile fibre to a rigid object of defined shape. In the industrial field, matrices can be of different natures depending on the reinforcement fibres with which they are used and the design requirements. They are usually grouped in two macro classes, thermoplastic and thermoset resins depending on whether or not the polymerisation process is reversible with heat. Due to their generally superior mechanical properties, thermoset resins have historically been more adopted in the structural field than thermoplastics counterpart. Among them, targeting low-cost applications, some inexpensive matrices with acceptable properties can be adopted. An example are the unsaturated polyester/styrene systems, which were adopted, reinforced with glass fibres, in the automotive field to produce the Chevrolet Corvette bodies. This class of resins can present some issues: it shrink a lot during cross-linking, can absorb water easily and its impact resistance is low, additionally it is not very chemically resistant. Another low-cost system is the so-called vinylester resin, which has some advantages over unsaturated polyesters. It does not absorb much water, and it hardly shrinks at all when catalysed. It also has good chemical resistance and high compatibility with fibreglass. Neither vinylester nor unsaturated polyesters are very good for high temperature applications, for which matrices such as epoxy resins must be used. Epoxy resins are made from the same monomer (diepoxide) as vinylester resins, but are re-

acted to a diamine group instead of the acrylic acid. Unlike the other types of resins mentioned above, which tend to form linear chains of monomers, in epoxy resin all the diepoxide and diamine molecules are linked to form a lattice. This confers the polymer a particularly high hardness and toughness, which, together with its excellent corrosion resistance and shape stability properties, make it particularly suitable for high performance and aircraft grade applications. On the other hand, epoxy resin shows some important drawbacks such as their cost and an higher viscosity than the other thermoset resins, which entails a technological difficulty of drapability leading to an additional production cost. Although with the advancement of technology, innovative solutions are being explored, involving the adoption of natural textile fibres combined with thermoplastic resins, in deference to the growing need for weight savings, recyclability of materials and environmental protection, for structural applications where outstanding stiffness and strength are required, epoxy resin and carbon fibres are still the best choice due to their superior performances and the level of quality guaranteed by established technological processes. The most typical processing route for carbon-fibre reinforced polymer (CFRP) composites, adopted in high performance structural applications, is the lay up of fibre laminates preimpregnated with uncured resin (prepreg). The resulting artifact is cured in an autoclave under controlled temperature and pressure. The prepreg ensures accurate control on the fibre volume fraction, while the pressure applied allows to eliminate entrapped air, leading to a very low porosity content ($< 1\%$).

As discussed, the advantages driving the adoption of fibre-reinforced polymer composites in structural applications are many, however they also have certain disadvantages that delayed their massive application until recently. Still today, their wider use is still restricted by the following limitations:

- the cost of building composite structures remains higher than their metal counterparts. Moreover, compared to steels, design

and development costs are much more uncertain due to the lack of maturity. Also the analysis methods are less reliable because of the reduced experience with this type of materials.

- the sensitivity to moisture absorption is particularly critical, as it affects the mechanical properties of the material and therefore its tolerability must be considered when designing. Epoxy resin shows a strong sensitivity to moisture due to the strong interaction between certain functional groups of the resin macromolecules and water molecules. The absorption of moisture also leads to a reduction in the material glass transition temperature (T_g), exposing it to further weakening.
- the aging effect due to the material exposure to heat sources and in particular to heating cycles that primarily affect the resin. The heating produces a progressive softening of the resin accompanied by thermal expansion and then shrinkage as it cools. Since the fibres do not show expansion or contraction phenomena, the discharge of residual stresses into the composite occurs. The problem can be exacerbated by the concomitant presence of moisture absorbed by the matrix.
- concentrated and out-of-plane loads represents critical conditions. The impact of hail and debris can even promote micro-crack nucleation, that can easily progress in matrix crack and/or delaminations. This is because the impact energy, unlike in metals where it is absorbed to perform plastic deformation work, in composites that do not exhibit plasticity is spent on forming fracture surfaces. Such sensitivity to micro-cracks and their degeneration in material macro damages, rises special concerns, since it is under the inspection tools detection sensitivity. Therefore the damage tolerance design has an important role in the FRP design.

- compared to metals, composite materials show a very low conductivity that expose them to be subjected to lightning strike damage. Therefore composite structures need to be protected to avoid the risk of this kind of damage, using solution that most of the time increase the weight of the structure.

1.3 Certification and testing

The reason for the increasing trend in use of FRP over the years, lies in the reduced manufacturing costs and increasing confidence, gained through applications on low-risk secondary structures. The expansion to more advanced and multiple applications, however, requires further cost reduction and an improvement in methods of analysis during development and certification. This issue is particularly felt in those industrial fields, such as aircraft, where high standards of safety and reliability are required. For these reasons, certification and testing are still among the highest nonrecurring costs in aircraft program, together with machining and prototyping [4]. The traditional certification procedure of composite structures, in the aerospace industry, follows the so called building block approach, here graphically schematized in Figure 1.3.

According to the block diagram, moving from the standardized material characterization tests (on the pyramid base) toward the full-scale tests (pyramid vertex), an increasing in test set-up complexity and costs occur. The firsts two levels on the pyramid bottom, consists in a standardized characterization of mechanical coupon and element tests. These result to be essentials to define the basic material properties and the response under single load conditions. These highly regulated tests are repeatable besides easy and cheap to perform. however, they do not provide accurate information about material behaviour on the structure scale, not considering the effect of the component geometry on the material response and the concurrence of different load con-

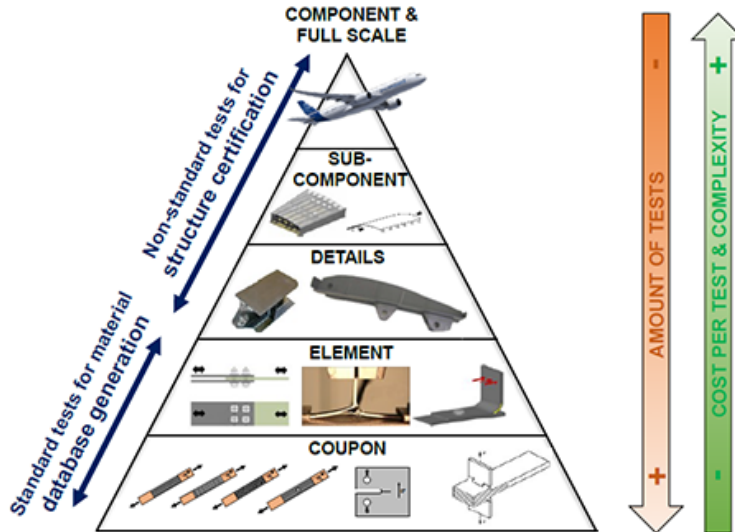


Figure 1.3: Building block diagram scheme for aerospace composite structures certification [2].

dition. Then, moving from the top of the pyramid to its base the reduction in costs and increase in the number of tests, goes together with a reduction in the capability to represent the actual loads acting on the structure or component in operating condition. This limitation in integrating material behaviour on different scales is the origin of the complexity and costs associated with certification process. Therefore, since the primary objective to enable the expansion of the application fields of composites is the simplification of the certification and testing process, the primary focus of scientific and industrial research the understanding of mechanisms linking the transferability of material behaviour on different scales.

1.4 Multiscale numerical tools

To simplify the decision-making process on every levels of the testing building block diagram, computational models are adopted. The numerical simulation methods play a central role in complementing and extending experimental results for the certification processes. The traditional approach to numerical modelling of a component or structure is of the type global-to-local (i.e. top-down). It was also a direct consequence of the need to contain the computational effort and the absence of detailed material behaviour models (damage models, dynamic response, interactions between constituents, etc.). On the bottom levels of the pyramid, the experimental results provide the basic material input for the numerical models, while on its upper levels the model can be validated and adopted to predict and deepen the material and structure response. Therefore, historically the calibrated model was adopted to perform first a linear finite element analysis (FEA) of the entire structure which was the starting point to define the global stress distribution and the most critical regions. Subsequently, local models of the regions of interest allowed detailed evaluations of local stresses and deformations. This approach has certain disadvantages related to the fact the foundation of the numerical model rests on a hierarchically high level of knowledge. In fact, the information provided by the standardised tests at the base of the pyramid on material response, is itself the combined behaviour of multiple constituent elements (reinforcement, matrix, interface, interphase, etc.). Since the characterisation is conducted on a scale at least an order of magnitude higher, the mechanisms underlying the failure phenomena cannot be appreciated. It is instead appreciable on the scale of the tests proposed in the present work. This results in the virtual test instrument being tied to the material on which the calibration was conducted, producing high inertia with respect to material innovation, because of the high cost and time needed for the experimental campaign required for the re-calibration.

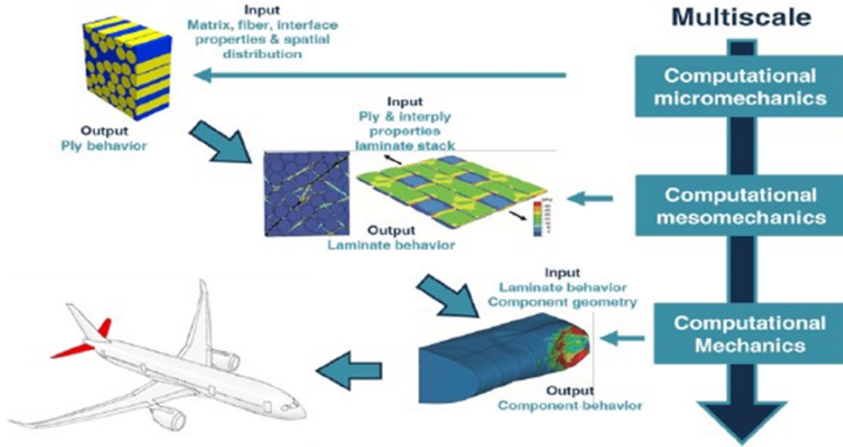


Figure 1.4: Bottom-up multiscale approach numerical modelling and virtual testing building block diagram

Over the years, both computing capacity and scientific and modelling knowledge exponentially grew. This made it possible to develop non-linear calculation procedures allowing the evaluation of stress-strain states in a much more accurate manner on computationally more expensive models [5]. This led the opportunity to radically overturn the pyramid, favouring a new bottom-up approach to the multiscale simulating strategy [6–8]. The traditional damage and failure phenomenological models needs to be replaced, in all the pyramid levels, by physically-based models capable to describe more in detail the real material behaviour. As reported in Figure 1.4, in composite material simulation many different scale levels are involved: the single ply level (μm scale), the laminate level (mm scale) and the components and structure level (m scale).

This relatively recent bottom-up strategy is based on the idea to be able to transfer information among these different scales, homogenizing the basic material properties into constitutive micromechanical models. Although micromechanical approaches have always been considered superior to purely phenomenological ones, both in terms of accuracy and effectiveness, the development of robust micromechanical models

is still hampered by the lack of experimental methodologies to measure the mechanical properties on the $nm - \mu m$ scales and the complexity of the microstructure geometry, which prevent the adoption of simple analytical approximation [9]. Nevertheless, the continuous growth of experimental techniques in the field of micro and nano scale testing, is gradually overcoming this issues.

1.5 UD FRP composites failure mechanisms

Since formed by two constituents, fibres and resin, presenting remarkably different properties, the prediction of damage initiation and propagation in CFRP materials results complex and challenging. The fibres demonstrate high stiffness and strength and a brittle failure mode with an highly anisotropic response. Otherwise, polymer matrices result to be much more weaker and less stiff than the fibres. A ductile damage mechanism characterize its compression failure behaviour, while the response in tension results to be essentially brittle [10]. The matrix yielding point is also sensitive to the degree of triaxiality, by mean it inversely depends on the tensile or compressive hydrostatic stress component. This behaviour was extensively studied in literature [7, 11–13] and also different yield criterion proposed and implemented in computational models [14, 15]. The coexistence of reinforcements and matrix lead to distinctive damage mechanism in UD FRP, as represented in Figure 1.5, where the surface of failure is reported on a representative volume element (RVE), for each of the possible loading configuration.

The failure under longitudinal tension or compression is mostly dominated by fibres. Although the compression failure mechanism, is also significantly affected by the matrix shear yielding and fibre-matrix debonding, as found in literature [16, 17]. Failure in longitudinal tension is essentially linear elastic up to the damage initiation and results

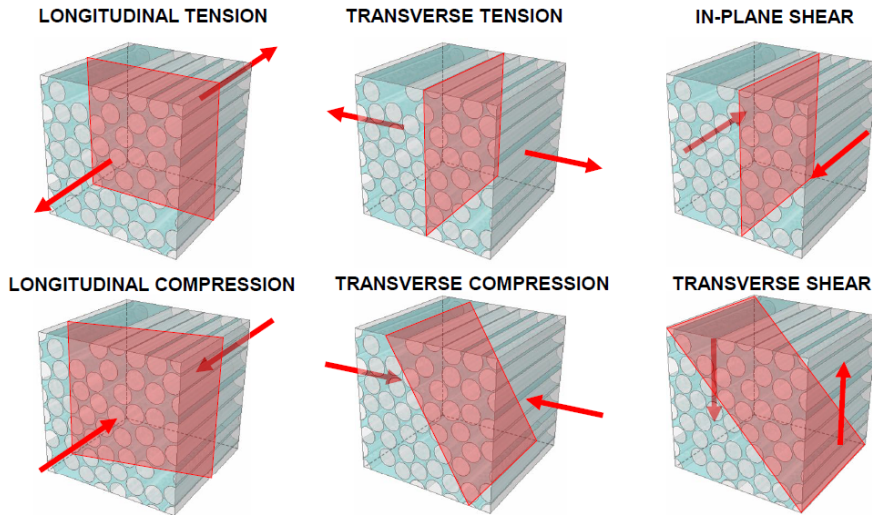


Figure 1.5: UD FRP failure surface scheme for each of the possible loading configuration [2].

in a brittle break on a plane perpendicular to the fibre direction and dominated by the fibre strength. It strongly depends on the size and distribution of the fibre pre-existing defects. On the other hand, in longitudinal compression the response is governed by the fibres kinking, a form of compression instability, that leads to the loss of load-bearing capability. This involves a slightly nonlinear response until the failure occurs. The kinking mechanism is promoted by fibres waviness due to a flawed manufacturing. *Herraez et al.* [17], observed the kinking triggering is also strongly correlated to the fibre-matrix interface properties. If it results weaker than the matrix, the interface failure initiate earlier the kinking. The fibre-matrix interface properties have an important role also in both transverse tension and compression failure mechanisms. Under transverse tension, the damage initiate at the fibre to matrix interface, where a stress concentration occurs. It is also favourite by residual interface stresses resulting from the manufacturing process, in those cases where the interface is weaker than the matrix [18]. Conversely if the interface strength results comparable or higher to

that of the matrix, the compressive residual stresses postpone the interface debonding. In these conditions, the damage is governed by matrix plastic deformation and the failure occurs once the matrix strength is reached. In both the discussed cases the failure surface is perpendicular to the applied load. In condition of transverse compression, an high degree of nonlinearity in the response before failure occurs. The plastic deformation are localized in shear bands due to the yielding of the matrix and to the fibre-matrix interface degradation [19]. The resulting failure surface results to be angled respect to the loading direction, with the magnitude of this angle depending to the combined interaction of matrix and fibre-matrix interface properties [20]. Lastly, the two shear failure mechanisms in Figure 1.5, also present a damage mechanism strongly influenced by the matrix and fibre-matrix interface behaviour. As demonstrated by *Totry et al.* [21, 22], the in-plane shear damage initiate, at the microscale, with the formation of shear debonding at the fibre to matrix interfaces that promote the propagation of plastic deformation bands along fibres direction. The consequent fracture surface is thus co-planar to the shear direction. In the case of transverse shear, the fracture surface is instead about 45° oriented respect to the shear axis. If the matrix is weaker than the fibre-matrix interface, the damage is triggered by the formation of plastic bands in the resin and the propagation on these one produce the failure. Otherwise, the damage is governed by the migration of the interface debonding among adjacent fibres through the matrix [18]. This heterogeneity in the failure mechanisms not only depends on the loading configuration, but also on the composite constituents and their interfacial properties. Furthermore, the described damage mechanisms interact with each other on the microscale of the individual ply. While on the higher scale of the laminate, consisting in a stack of plies with different fibres orientation, these damage mechanisms simultaneously occur further contributing to the FRP composites failure prediction complexity [23].

1.6 Fibre-matrix interface in composite

1.6.1 Interface and interphase definition

The adhesion of the fibrous phase to the polymeric matrix and its relationship to the properties of the composite has been object of continuous investigation from the origins of composite materials, since adequate interfacial properties are an essentials requirement for producing a composite with acceptable mechanical properties. Efforts to explain adhesion through chemical forces, electrostatic interactions, surface energy considerations, etc. resulted largely not exhaustive [24]. The attention was on the surface chemical aspect of adhesion, neglecting other related changes occurring in regions adjacent to the fibre-matrix interface. More recent findings evidenced as the complex transition zone between fibre and matrix can't be reduced to the interface surface only. This region, named interphase, also extends on both the surface sides, including a portion of both matrix and fibre results chemically and morphologically different if compared to the respective bulk materials. This regions may include impurities, non-polymerized resin or/and resin additives as well as voids and entrained gases. For these reasons, as proved by *L.D. Drzal* [25], the resulting fibre-matrix interfacial properties are always influenced by technological aspects involving fibres surface treatments and finishing, matrix mechanical and thermal properties as well as its volumetric shrinkage under polymerization. At the molecular level, fibre-matrix interaction is driven by the two phases chemical structures, by means van der Waals forces, acid-base interaction and chemical covalent bonds. The resulting bond strength depends on the interfacial bonds concentration and it is characterize by the work of adhesion which includes the contributions of all types of physical and chemical local and non-local interactions [26]. From the engineering point of view the problem take the form of identifying bond strengths and critical energy release rate. This means dealing with the problem at the single fibre level. Because

of the complexity in the physical and chemical phenomena that influence the morphology and characteristics of the interface, the problem of its characterisation is particularly challenging.

1.6.2 Interface testing methods

A large number of experimental methodologies have been proposed in literature to characterize the fibre-matrix interface properties. Some of these tests are performed on a higher scale than that of the fibres. It is the case of tensile tests with the load applied on the fibre transverse direction or the in-plane shear tests, both performed on the composite ply scale. These easy to perform experimental methods, supported by analytical models and computational tools, retrace to the interfacial properties starting from the sample fracture surface analysis [27]. More accurate tests are those performed on the micro-mechanic scale, which involves a single fibre. They aim to a proper isolation of the interface debonding phenomenon, reducing the influence of matrix failure and surrounding fibres. In contrast, they present difficulties in specimen preparation and test execution. The single fibre micro-mechanical tests may be classified in two main categories. One major group is represented by those tests in which the load is directly applied on the fibre, such as push-in, pull-out tests and microbond test. The remaining group consists of those tests in which is the matrix to be loaded, they are the fragmentation and cruciform specimen tests. The listed testing methodologies involve different stress fields at the interface as well as in both fibre and matrix. Therefore, the fibre-matrix adhesive bond strength and energy release rate, obtained with these methods, resulted often not surprisingly different for a given FRP. For all of these tests, since the average diameter of a single fibre in UD FRP, the use of specific equipment is required and also the specimen preparation, test execution as well as data acquisition result very difficult. Following, with the purpose to point out the state of the art in FRP interface test-

ing methodology, the most commonly adopted micro-mechanical single fibre tests will be described both from the experimental methods and analytical framework point of view.

The fibre push-in test is one of the easier to perform methods for interfacial properties obtaining. It is performed on a laminate cross section slide, placed on a holed holder, in which a single fibre is pushed through its site in the matrix by means of a nano-indenter. It allows to continuously monitor the applied load and the indenter tip displacements, providing a force-displacements curve as the one reported in Figure 1.6. In it three regions can be identified, corresponding to as many interface debonding evolution stages.

Stage I - Elastic pre-beonding deformation regime

Stage II - Debonding initiation and progress

Stage III - Post-debonding frictional sliding

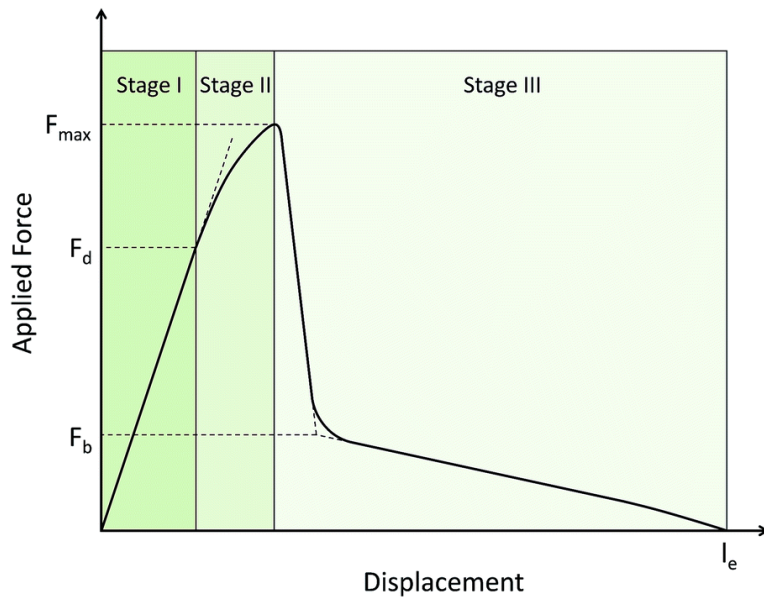


Figure 1.6

In Stage I, the pre-debonding interface stress field is characterized by a combination of normal pressure and shear along the fibre axis.

The fibre confinement leads to an additional component of pressure, whose maximum value is on the top of the interface surface, where the confinement transverse strain is maximum. A component of bending is also induced to the difference between the indenter diameter and the specimen holder hole diameter. This component increases for thinner specimens and larger hole diameters [28]. The resulting stress profile depends on the matrix and fibre elastic properties, the indenter geometry and applied load. The described stress field schematic is reported in Figure 1.7. The difference in the fibre and matrix thermal expansion coefficient may also induce a residual initial shear stress. Once

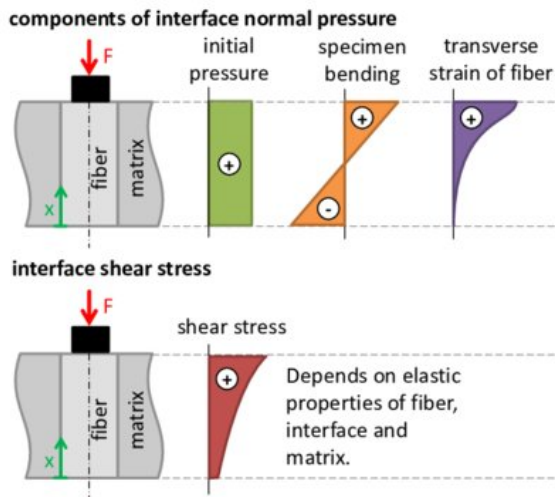


Figure 1.7: Push-in test interface stress field schematic during the elastic pre-debonding phase [28].

the interface strength is exceeded, the debonding initiates close to the fibre upper edge and propagates along its length until it become unstable (Stage II). In this phase the interface shows simultaneously a debonded region, on the top of the fibre, and a still bonded region. This cause a decrease in the specimen stiffness associated to a progressive reduction in the force-displacement curve slope. The entire interface surface debonding corresponds to an instantaneous drop of the

load value (Stage III). To this point the push-in force depends on the debonded in contact surfaces frictional properties and the amount of the normal pressure [29]. It is possible trace back the average interface shear strength from the values of force and displacement, according to the relation reported in equation (1.1).

$$\tau = \frac{F}{\pi DH} \quad (1.1)$$

Where F is the measured force, D and H respectively the fibre diameter and height. Considering the maximum value of measured force F_{max} in (1.1) the interfacial shear strength τ_s can be estimated. While considering the value of force F_b reached during the Stage III sliding, the respondent τ_f is the frictional shear stress. However, the shear strength computed in this way might not be the true bond strength, since the debonding not occurs instantly. The experimental literature suggested the more brittle is the interface failure, the more accurate the strength estimation. This means this testing methods results more appropriate for those composite that exhibit brittle and high modulus matrix, like ceramics. Nevertheless, despite this might seem surprising for a FRP, it has been reported [30] the boundary layers of epoxy near the fibres surface can exhibit a high elastic modulus and a brittle crack propagation. Starting from the force-displacement curve also the energy release rate can be inferred. The theoretical background proposed by *Kerans et al.* [31] has shown some limitation since both the propagation is considered linear elastic and no plasticity of the matrix is accounted.

The pull-out test consists in forcing a fibre to debond from the matrix by applying on it a tensile load. Differently from the push-in test, this is not a method directly applicable to the actual composite. The specimen, consisting in a single fibre embedded into a matrix block, is specifically prepared. The resulting force-displacement curve is quite similar to those described for the push-in test. It has a linear elastic

pre-debonding region, characterized by two interface stress component: shear and a negative pressure induced by the Poisson's necking effect. This produce a generally more brittle region of debonding initiation and propagation, if compared with the push-in test. The load tends to peak with small changes in slope and then sharply drop. In this case reduced value of frictional sliding force can be detected, since the absence of a confinement pressure. However, sometimes an improper propagation may result. As observed in literature [32], after initiation the debonding may kink into the matrix, resulting in a $2 \div 7\mu\text{m}$ thick layer of resin all around the fibre.

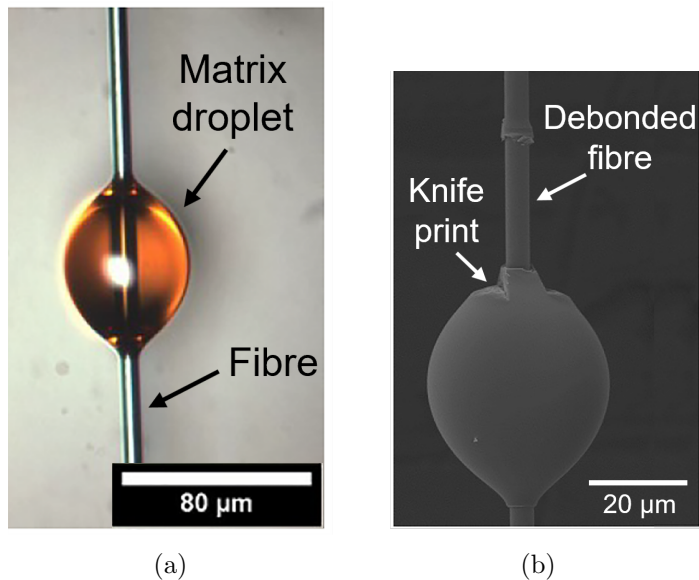


Figure 1.8: Optical image of a carbon fibre and epoxy resin microbond specimen (a) and SEM image of the tested specimen, with the knife print on the resin highlighted (b).

This improper outcomes of the test is associated to a higher value of frictional force. Based on the same principle is also the microbond test, consisting in a droplet of resin enveloping a fibre portion (Figure 1.8(a)). The fibre is loaded in tension between a couple of knife whose distance is bigger than the fibre diameter, but lower than the droplet one which remains constrained. As reported in Figure 1.8(b),

the presence of the knife may produce plastic deformation on the droplet as well as an additional matrix cracking. This can significantly affect the quality of the results. It was demonstrated also small variation in knife distance produces large difference in load magnitude and shear stress peak location along the fibre. In general larger the separation distance higher the bond strength overestimation. Numerical studies evidenced as the knife shape has an affect on the results, since induces a stress field in a droplet region close to the fibre interface [33].

An additional experimental methodology to estimate the interface shear strength, is represented by the single fragmentation test. It was widely adopted in literature to measure the effect of different surface treatments on the interface strength of carbon and glass fibres. The specimen consists in a dog-bone shaped block of resin incorporating a single fibre oriented along the specimen axis. It is loaded in tension and the load is transmitted to the fibre as interfacial shear stress. As the tensile stress rise a fragmentation process of the fibre starts. First the fibre brakes at its weakest point, then at successively weaker points. Since the external load transfer on the fibre is operated by the interface shear stress, the fragmentation process ends when the fibre fragments tensile strength reaches the interfacial shear strength. This condition is referred as saturation. The corresponding fibres fragment length is defined as critical length and denoted as l_c (Figure 1.9).

Assigned the fibre, matrix and specimen geometry, the greater l_c and fewer the number of fragment, weaker the interface strength and vice versa. An analytical interpretation of the test results was proposed by *Kelly and Tyson* [34]. They suggested the fibre fragment critical length l_c can be related to the fibre strength σ_f , the fibre diameter d and the shear strength τ_f , according to equation (1.2).

$$l_c = \frac{\sigma_f d}{2\tau_f} \quad (1.2)$$

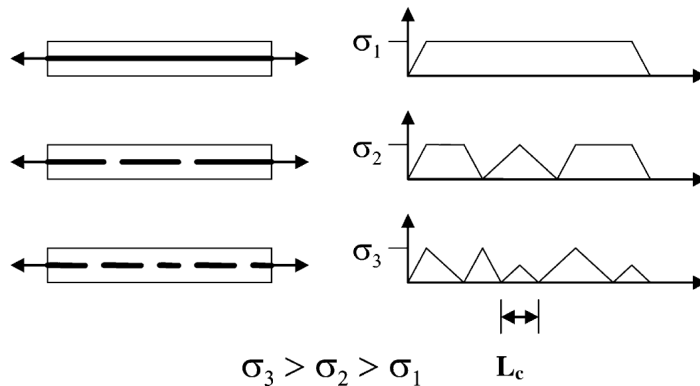


Figure 1.9: Fragmentation test at different stages and critical length scheme.

This analytical formulation is still the basis of the fragmentation test results interpretation and may have a threefold interpretation: first, in the form it is presented in equation (1.2), it allow to estimate l_c known the other parameters. Second, σ_f can be expressed in function of the fragment length. Third, τ_f can be computed at the saturation. Among them, the interfacial shear strength measurement is the most appealing and received in-depth studies to clarify the methodology. They evidenced as the fragmentation is a very complex testing method, involving several different micromechanical phenomena as well as difficulties in data acquisition. The major limitation are represented by:

- the critical length l_c definition. It results very hard, due to the statistical nature of the fibre strength and the reduced accessibility of the embedded fibre. The fragment lengths for transparent matrix composites are measured using a conventional optical microscope, while the acoustic emission technique is adopted for non-transparent matrices.
- also the tensile fibre strength σ_f is affected by statistical fluctuation and moreover its estimation, generally performed through

ex-situ tests, may be irrelevant to describe the *in-situ* effective properties.

- it was demonstrated the tensile strain needed for the saturation is up to three times the fibre failure strain. This means, in matrices with reduced failure strain the computed shear strength τ_f is not the interfacial one but corresponds to the matrix shear yielding.

Despite many analytical study were performed to improve the accuracy of the *Kelly and Tyson* proposed relation and spectroscopy and photo-elasticity technique were adopted to monitor the matrix behaviour close to the interface, fragmentation tests still presents significant limitations in fibre-matrix interface properties measurement.

The described testing method aim to estimate the interface response in shear mode only. To characterize the properties in normal mode, a stress field transverse to the fibre axis must be exerted on the interface surface. It can be achieved with the cruciform specimen test. It consists in a single fibre embedded in one of the two arms of a cross shape sample made by resin. As schematized in Figure 1.10, the other arm is clamped and loaded in tension. The angle ϕ between the two arms governs the load transmission direction on the interface, $\phi = 90^\circ$ allows to test normal mode, while different angle produce a shear and normal stress combination.

The distribution of stress σ_n at the interface is characterized by higher value around the middle of fibre length, which progressively decrease toward the extremity. This results an advantage, since it avoid the effect of stress concentration at the fibre ends that is the predominant cause of precocious debonding initiation in tests such as push-in and pull-out. Therefore, the interfaces in cruciform specimens can sustain a much higher stress before failure than the other presented specimens type.

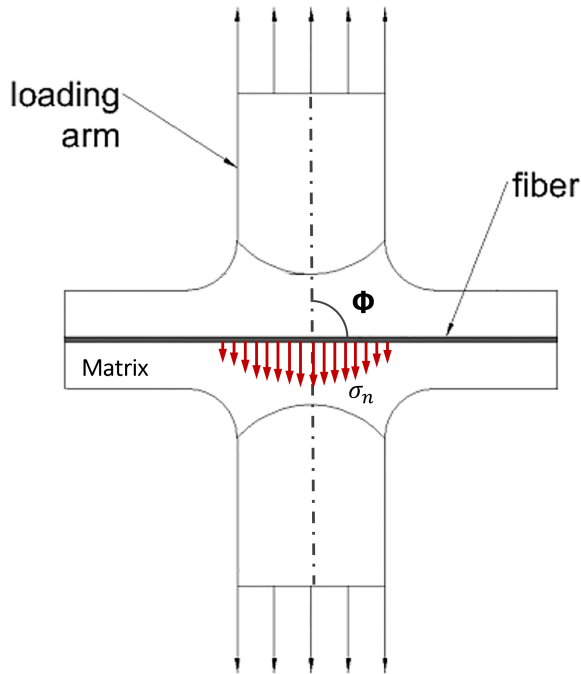


Figure 1.10: Cruciform specimen scheme.

1.6.3 Role of interface in damage mechanisms

As discussed in section 1.5, the fibre to matrix interface plays a fundamental role in the most of the FRP composite damage mechanisms. For this reason, in structural field its determination was experimentally tested and numerically investigated over time. In 1991 *Curtin* [35] proposed a failure model for ceramic matrix composites based on the global load transfer (GLT) principle, that estimate the strength of an unidirectional composites as a function of the fibres strength and interfacial strength. Further studies demonstrated this theory can be applied to UD FRP, but in a limited number of cases and with inaccurate results on the composite strength prediction [36, 37]. More detailed models were based on a local load transfer principle, considering the effect of stress concentration through a complex analytical formulation and the adoption of statistical Monte-Carlo simulation [38–41]. *Ha et al.* [42] demonstrated both the strength of the matrix

and the strength of the interface, govern the transverse final strength of an UD composite. *Koyanagi et al.* [43] investigated the unidirectional CFRP and GFRP composite strength, as a function of the fibre, matrix and interfacial strengths. They experimentally estimated the interfacial shear strength through two kind of micro testing: the fragmentation test and the push-out test, by finding the two methods may not be equivalent. They also applied the GLT model to analytically predict the UD composite strength and compared the results with a large amount of experimental outcomes on different UD composite materials, here reported in Figure 1.11.

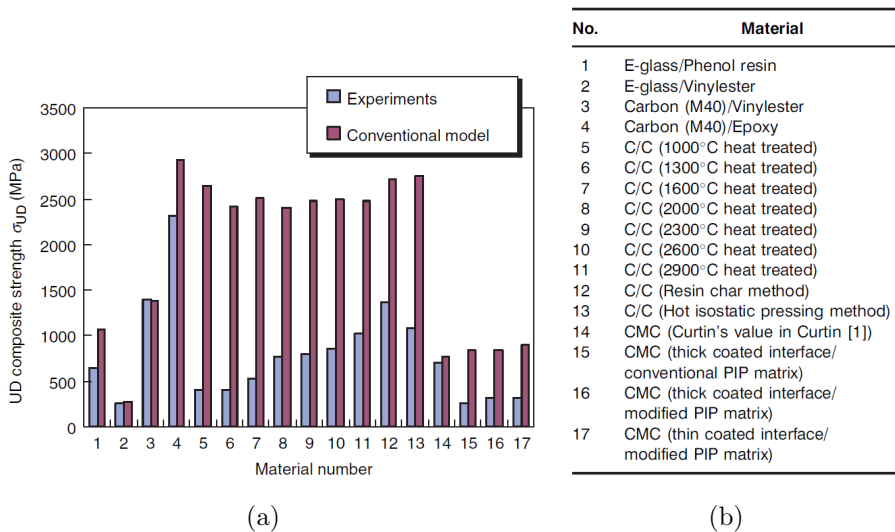
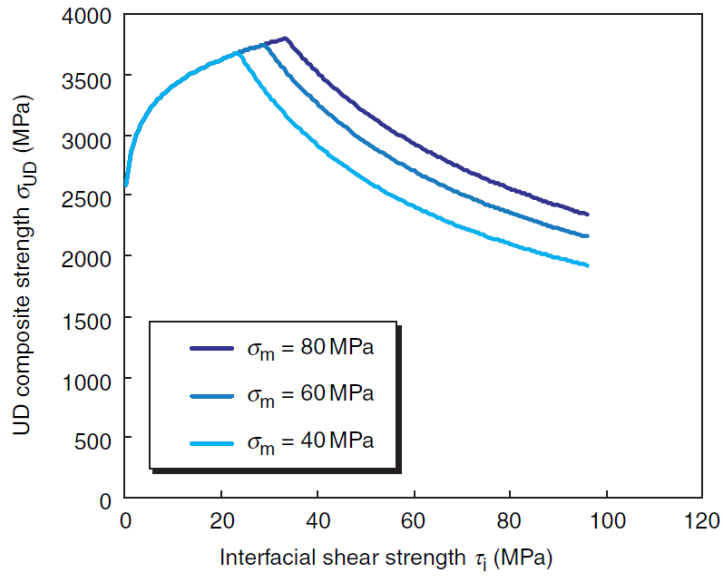


Figure 1.11: Graphical comparison between experimental and GLT predicted strengths for several UD composites (a) and list of investigated UD composite (b) [43].

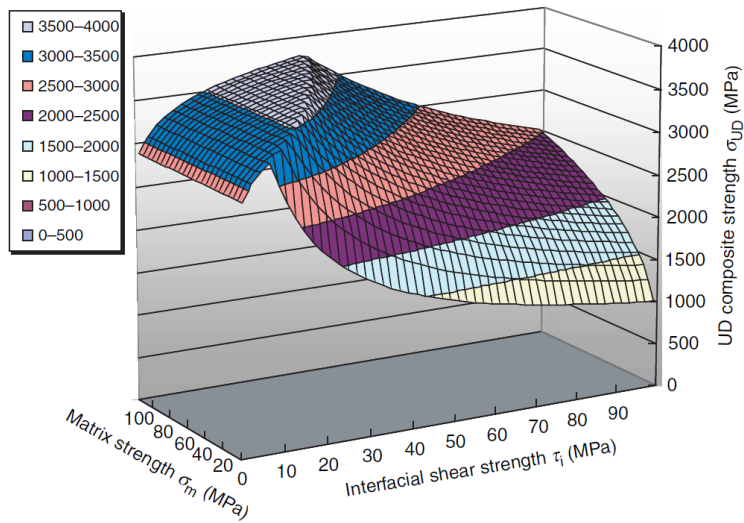
The comparison demonstrate the GLT has a good prediction capability for few of the considered UD composites, while for the majority it greatly overestimate the effective material strength. The same can be also appreciated among the tested FRP subset (materials from n° 1 to 4 in Figure 1.12(b)). Therefore, *Koyanagi et al.* proposed a modification of the model to also consider the effect of simultaneous fibres failure. It take into account when a weak fibre fails also some neigh-

bouring fibres can fail simultaneously, because of the propagation of the damage through the surrounding matrix. The proposed modification demonstrate improve the UD composite strength predictivity, although still based on a phenomenological approach. Anyway a relevant evidence emerged: the UD composite strength is greatly influenced by the fibre-matrix interface strength and by its mutual interaction with the matrix strength. In Figure 1.11(a), the strength as a function of the interfacial strength is reported for a group of UD carbon reinforced composite, manufactured with three different epoxy resins. The tensile strength of each resin is listed in the legend named as σ_m . It can be seen with the interfacial shear strength rising, the composite strength first increase up to a maximum, then starts to rapidly decrease. This is because on the left of the maximum, the composite damage initiate at the interface with the fibre debonding, while on the maximum right the damage initiate due to the matrix failure. This is also why the composite strength dependence to the matrix strength is visible only on the right branch of the curves, where the damage initiation actually depends on the matrix. Finally, in Figure 1.11(b) the UD composite strength is reported in form of surface in function of both the interface shear strength and matrix strength.

The effect of the temperature, on the interfacial normal strength, also was investigated in literature. *Koyanagi et al.* [27] characterized the fibre-matrix interface properties through macro-scale tests and a computational approach. UD carbon/epoxy specimens were tested in the direction transverse to the fibre, under tensile load, at various temperatures and strain rates. A 2D finite element model (FEM), representing a single fibre embedded into the resin, was developed. It allowed to estimate the stress concentration and the residual micro-stress field at the interface critical point, demonstrating a cohesive zone model (CZM) can be adopted to numerically modelled the interface behavior. The authors concluded the interface strength in normal mode is independent of temperature, because the experimentally measured



(a)



(b)

Figure 1.12: Unidirectional composite strength as a function of interfacial shear strength (a) and as a combination of interfacial shear strength and matrix strength (b) [43].

variation can be charged to the thermal residual stresses field. Also the strain rate was found not affect the interface properties. *Straub*

et al. [44] investigated a kevlar/epoxy interface properties adopting a micro-bond testing method. Different testing temperature and load application speed were probed. The authors declared the interfacial shear strength decrease with the temperature rising and the effect of testing rate is negligible. *Koyanagi et al.* [45], in a not so much more recent study than the previous one, adopted the cruciform specimen method to investigate the normal mode interface strength and its dependence on the temperature, in glass/epoxy composite. In this work, also two different resin polymerization temperature were investigated to estimate the effect of manufacturing process on interface properties. It was found the interface strength does not increase as temperature increases, while an increment in normal interfacial strength occurs when the composite is cured at an higher temperature. Therefore, the interfacial strength temperature independence, was obtained for the normal strength with macro-scale tests [36] and with micro-scale tests [45], while the opposite was for the shear strength, tested adopting a micro-scale experimental approach [44]. In all the presented studies, an estimation of the interfacial properties was attempted. Some of them inversely extrapolated an interface properties set consistent with the macro-scale UD composite failure evidences. Others tried experimentally measure the interface properties in normal or shear mode, adopting both macro-scale and micro-scale tests. In each of these cases, the results showed an high uncertainty and often produced conflicting results. This is partly because of the trouble in experimentally measure the fibre-matrix interface properties. Since no unified testing procedures are available and the literature proposed tests resulted ineffectual both on micro than in macro scale. And partially because the understanding of the interface bond formation, on the molecular scale, at the chemical and physical level results still very restricted.

1.7 Motivation and objectives of the work

As discussed, application of UD FRP in the field of industry and particularly in aerospace became rapidly widespread since their introduction. The lightweight, high rigidity and strength, together with the opportunity to tailor the mechanical properties on the specific application requirements, made composites a flagship of innovation. Since the market's increasingly stringent demands for safety, performance and pollutant emissions, composite components and structures requirements in terms of structural response and certification gradually raised. In this innovation process, analytical and numerical tools, as well as experimental and technological procedures, widely established in the design of such components and structures, began to show some limitations. As detailed highlighted in this introduction, in FRP damage definition and characterization, both the experimental methods and numerical approaches resulted to be largely insufficient to define robust standardized procedures. This is because a full understanding of the phenomenon on all the scales is still missing and limited to the opportunity to perform ever more complex and detailed investigation about micromechanical aspects. The regulated experimental procedures date back to the early beginnings of these studies and the computational methodologies are basically based on phenomenological models. In recent years many studies investigated new procedures for FRP characterization, leading to innovative approaches to modelling. However, because of the uncertainty and complexity of these new tools, they are still not applied to composite industrial design and production world. Nevertheless, the importance of thoroughly understand and systematically measure the FRP micro-scale properties, such as the fibre-matrix interface, emerged. It was proved it plays a central role in the macroscopic response we appreciate and sometime we are not able to justify.

For these reasons, with the purpose of minimally contribute to the

knowledge about the topic, in this work a never attempted experimental methodology is tuned and integrated with a computational method. So a novel approach to the fibre-matrix interface properties characterization of UD FRP is proposed.

1.8 Dissertation structure

In the following chapters, the adopted experimental and numerical methodologies are presented and thoroughly justified. A never applied before in composite, testing experimental procedure, is introduced and the specimen preparation detailed. Then the performed campaigns of tests are deepened. Afterwards the proposed numerical model development and validation process is discussed and the computational methodology it is based on described. The experimental and numerical results are presented and the interface properties identification process explained. Finally the found interface properties are presented in the light of the literature available ones for the investigated material.

Chapter 2

Experimental Methods

2.1 Micro-cantilever test introduction

In recent years, the deformation of small volumes of material has been of great interest to the scientific community. This because of the miniaturizing of mechanical components in application fields such as bio-engineering, nano-actuation, micro electro-mechanical systems, functional thin film deposition etc. Classical continuum theory is the most broadly used tool to predict the structural behavior of materials and reflect it in structural analysis and design. As the dimension of the structure decreases, the stiffness predicted by classical continuum theory becomes lower than that of the real structure. This is because material properties begin to deviate from bulk scaling laws as characteristic dimensions become small. This means the bulk properties can no longer be applied to the micro scale systems and the specimen size effect of the mechanical properties at micro scale range is critical [46]. Since the application of conventional testing methods to the micro scale range presents significant limitations, a variety of micro-testing methods have been developed. The majority of the growing nano-scale data-set of materials and geometries are tested in compression, via nano indentation and micro pillars. These results to be the easiest

tests to perform. Other methodologies such as tensile and cantilever bend micro testing, have been utilised to a lesser extent to test material response under different stress states, particularly tensile stresses.

The novel experimental approach to the fibre to matrix interface characterization, presented throughout this dissertation, was made possible thanks to the IMDEA Materials Institute, with the help of the Structural Composite Group. The experimental specimen preparation and testing campaigns were conducted at the IMDEA laboratories adopting their facilities. Also the tested material was provided by, and prepared at, the IMDEA materials institute.

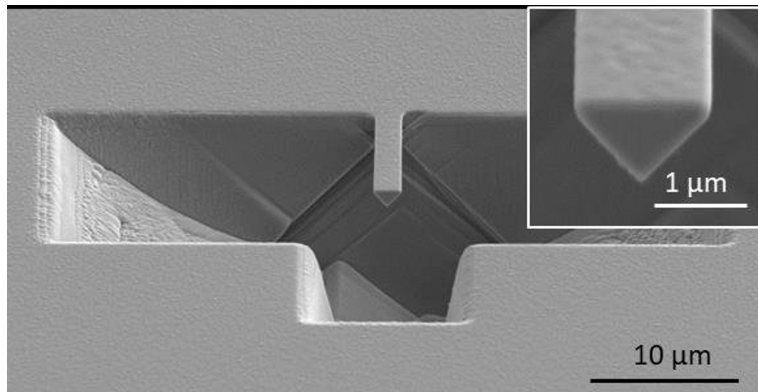


Figure 2.1: Literature SEM image of a MoS₂ micro-cantilever beam, into the inset a beam cross section detail is reported [47].

The micro-cantilever test (MCT) consists in a typical free-standing cantilever beams loaded with a force on the extremity. The peculiarity is that the specimen is microscopic. The induced strain is a mix of bending and shear. Since the specimen is milled from a macroscopic block of material and the load is simply applied through a nano-indenter tip, this test overcomes many of the difficulties of gripping and constraining the specimen that limits the performance of non-compression microscopic tests. In Figure 2.1 a literature example of micro-cantilever beam is reported. It is a scanning electron microscope (SEM) image of a molybdenum disulfide micro beam in frontal view. A beam cross section detail is reported into the inset [47].

MCT method was widely adopted in literature. *David E.J. Armstrong et al.* [48] experimentally investigated the Young's modulus anisotropy of polycrystalline copper through MCT. They found at the microscopic scale a dependency of the Young's modulus on the crystals orientation exists. The MCT resulted to be a useful approach to measure this effect. *Jae-Hoon Choi et al.* [49] adopted MCT to understand the size effect in gradient elasticity. MCT on cantilevers with various thicknesses were performed to demonstrate increase in the bending rigidity with decrease in beam thickness. They evidenced, unlike beam solution from classical continuum theory, the effective elastic modulus measured from micro-scale experiments was not a constant. The MCT method was also adopted in thin coating films characterization. *Dongil Son et al.* [46] estimated Young's modulus and tensile strength of Aluminium and Gold coating film through in-situ MCT. The results showed to correctly estimate the searched material properties if compared with literature data obtained by nanoindentation test. Furthermore, they also evidenced a correlation between the coating film micro-morphology and the measured properties. MCT method was also adopted in interface properties characterization. *J. Schaufler et al.* [50] tested in-situ the interface fracture strength and toughness of hydrogenated carbon coatings on steel substrate. The authors found, under slight difference in the adhesion layer properties, totally different interface failure behavior.

Despite the large number of MCT application which can be found in literature, to the best of the author knowledge, this type of experimental method has never been applied to FRP.

2.2 Material

The novel experimental and computational methodologies presented throughout this work were tested on the *IM7-8552* UD CFRP materials with the collaboration of the Composite Material Group of IMDEA materials institute. It is a well known material, extensively adopted in aerospace industry and deeply investigated in scientific publications. Therefore it is perfect to validate the novel micromechanical testing and computational modelling methodologies developed in this work. The *HexTow IM7* is an high performance intermediate modulus carbon fibre widely applied in aerospace industry. The *Hexcel 8552* resin is an amine-cured epoxy containing polyethersulphone. This is a tough resin that has been used for aerospace applications for many years. The *IM7-8552* system is very popular and its properties and performance are well known to the industry. The material was supplied in form of unidirectional fibres prepreg, with areal weight of $268g/m^2$. The mounted samples, in which the micro-cantilever specimens were carved, were extracted from 4 plies $[0^\circ/90^\circ]$ laminate. It was manufactured by hand lay-up, vacuum pressed and then cured in an autoclave at $180^\circ C$ for 135 minutes, with a heating/cooling rate of $2^\circ C/min$. A pressure of 7 bar was applied during heating, curing and cooling. The resulting single ply thickness was equals to $0.25mm$ and the nominal fibre volume fraction was the 60 %. The *IM7-8552* mechanical properties were extensively studied in literature. *Rueda Ruiz* [2] in his dissertation performed both macro and micro mechanical characterization thereof. He also tested the fibre and neat matrix standalone. Other authors estimated the same properties for *IM7* fibres and *8552* resin manufactured with different production technologies and tested under different strain rates. In Table 2.1 the elastic properties adopted in the present work for *IM7* fibres and *8552* resin are reported.

According to literature evidence the *8552* resin is considered as isotropic, while the *IM7* fibre is transversely isotropic. The reference

Table 2.1: *IM7* fibres and *8552* resin estimated elastic properties.

IM7 properties					
E_1 [GPa]	$E_2 = E_3$ [GPa]	$\nu_{12} = \nu_{13}$	ν_{23}	$G_{12} = G_{13}$ [GPa]	G_{23} [GPa]
275.69	24	0.23	0.46	36.6	4.7
8552 properties					
		E_m [GPa]	ν_m		
		4.2	0.25		

system adopted for the fibre is oriented so that the local 1 axis matches the fibre longitudinal axis, while the remaining axes 2 and 3 lie on the fibre cross-section plane. The best mechanical properties are expressed along the direction 1, while along the other two axes the properties are lower and comparable. The values considered in this work represents an average among the literature proposed ones. To confirm those correctly describe the elastic behaviour of considered materials, a sensitivity study has been conducted on the numerical proposed model which are going to be presented in the following Chapter 3.

2.3 Specimens design and manufacturing

The MCT applicability to UD FRP interface testing was evaluated. Characterize the fibre-matrix interface through MCT in a UD FRP, means mill the beam inside a single carbon fibre so that the interface surface represents the connection between beam and surrounding matrix material. In this way the testing condition presented in 2.1 are fulfilled. The test configuration results similar to a cantilever beam connected to a deformable block. The beam and the block results to be made of different materials and straddling these two is the interface surface, positioned close to the constrained end of the beam. Given the average diameter of a single carbon fibre in the range $5 \div 20\mu m$, the

difficulty in specimen machining is evident. The micro-cantilevers fabrication was performed in a combined dual beam equipment, equipped with a SEM and a focused ion beam (FIB) system, available at the IMDEA materials institute. The electron and ion beams intersect at a coincident point with an angle $\alpha = 52^\circ$ allowing simultaneous SEM imaging and FIB milling. By carefully controlling the energy and intensity of the ion beam, it allows to mill the material surface with nanometric precision. In Figure 2.2 a schematic representation of the dual beam equipment is reported. In addition to the two beams a gas injection device is also represented. It enable gaseous media such as argon, hydrogen or other noble gases to be injected close to the sample surface

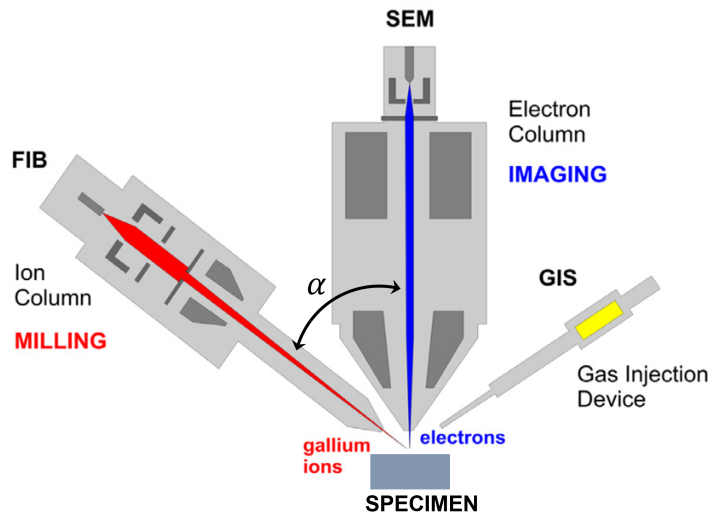


Figure 2.2: Schematic representation of a dual beam equipment

The machining needs to be performed under vacuum conditions to prevent material oxidation and undesired beam interactions with the atmosphere. The UD FRP sample is thus placed in a vacuum chamber where the milling is executed. The specimens were obtained by eroding material on a surface section, perpendicular to the fibres direction, of a UD CFRP laminate. A clean and regular machining surface portion

is identified, through live SEM imaging. Then, one of the randomly disposed in the matrix fibres should be selected. It is important in this choice the fibre is sufficiently spaced from the others surrounding. Thus guaranteeing a defined fibre-matrix interface available and avoiding the presence of fibres clusters could affects the tests execution.

Table 2.2: FIB parameters for *IM7-8552* milling process.

	Milling	Current	Voltage	Depth
Step I	Ga^+ ion beam	9.3 nA	30 Kv	8 μm
Step II	Ga^+ ion beam	0.79 nA	30 Kv	5 μm
Step III	Ga^+ ion beam and assisting gas ($MnSO_4$) $7H_2O$	2.5 nA	30 Kv	/

A systematic methodology leading to regular micro-cantilevers, through three milling and a final finishing steps, was developed and following reported:

Step I - a horse-shoe shaped pattern, embracing the fibre, is defined and the first milling performed eroding material in the fiber direction. The milling interests a depth equals to $8\mu m$ and the FIB was set at a voltage of $30Kv$ and a current of $9.3nA$.

Step II - the FIB is tilted of its maximum angle ($\alpha = 52^\circ$) to undercut the specimen side and obtain the cantilever. The machining is repeated on the other specimen side by rotating the FIB 180° around the specimen beam axis. This milling steps, interesting a depth of $5\mu m$, is performed adopting a current reduced to $0.79nA$ and maintaining the same voltage value. The tilted milling direction is the reason of the characteristic *upside down house* shape of the cantilever section, as graphically reported in Table 2.3.

Step III - in this milling phase the former steps are retraced to refine the cantilever shape and sharpen its edges. This phase is conducted with maganese sulfate heptahydrate assisting gas and the FIB working parameters set according to Table 2.2. The adoption of gas assistance is due to the need to reduce the thermal injuries the process produce on the material near the milling region. It also allows to increase the cutting quality by sharpening the cutting edges. On the other hand it needs a much higher cutting time.

In Figure 2.3 a schematic representation of the described milling steps is reported. Cutting pattern and milling steps outcomes are reported for both Step I (Figure 2.3(a)) and Step II (Figure 2.3(b)), together with the related milling direction. A fully processed micro-cantilever beam representation is showed in Figure 2.3(c) with the fibre-matrix interface highlighted.

An SEM image of a ready to be tested specimen is here reported in Figure 2.4. In it can be seen the cantilever beam carved straddling a single fibre and a matrix portion, the interface between them and the surrounding fibres and matrix.

A total of 54 micro-cantilever samples were carved during 6 experimental preparation campaigns. In each campaign the fabricated specimens were classified by numbering them individually and measured via live SEM imaging. Since the handcraft nature of the production process, the cantilever length and the section shape may differ among the campaigns. Thus the statistical analyses to derive the specimens characteristic measurements, were conducted by campaign. As reported in Table 2.3, the average and deviation values, of cantilever length (L) and section geometrical measurements (H, B, W, Area), were computed. These statistical information are going to be adopted to the computational model design and validation. The nomenclature system adopted in the present dissertation identifies each preparation campaign with the letter C followed by a number from 1 to 6. Further,

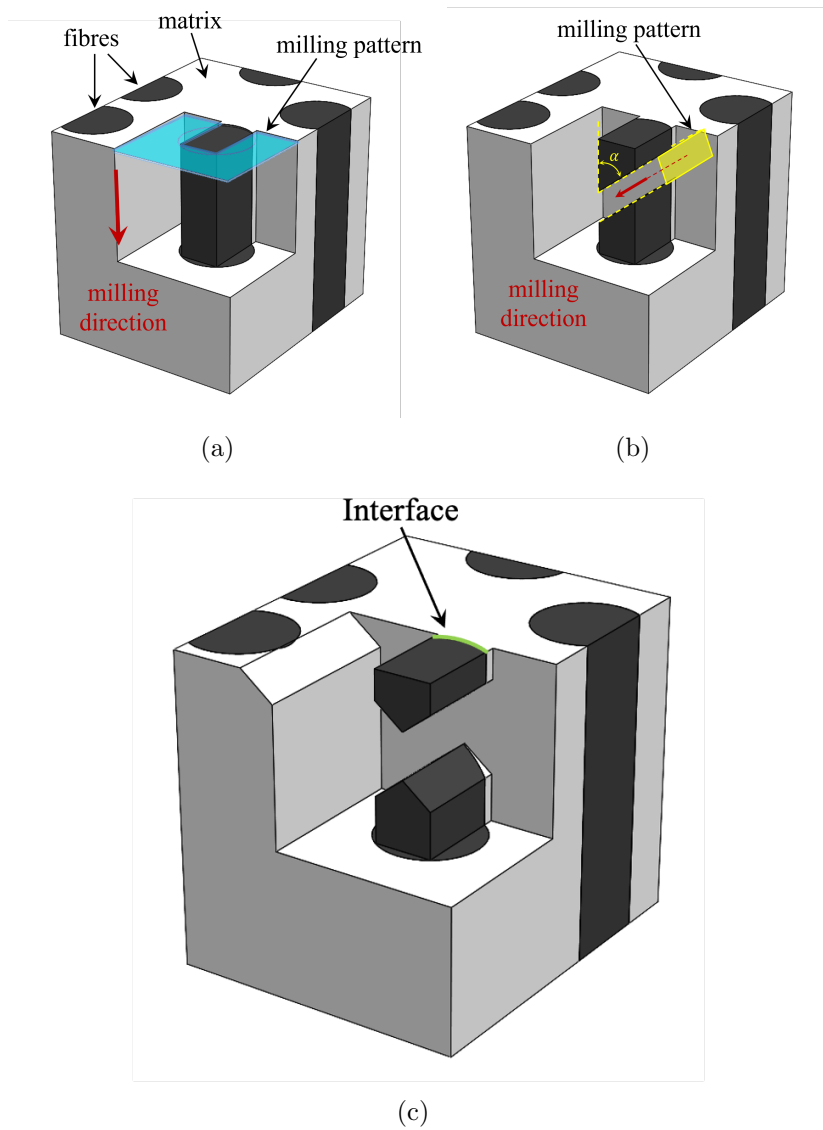


Figure 2.3: Schematic representation of milling patterns and cut outcomes for Step I (a), Step II (b) and fully processed micro-cantilever sample (c) with fibre-matrix interface highlighted.

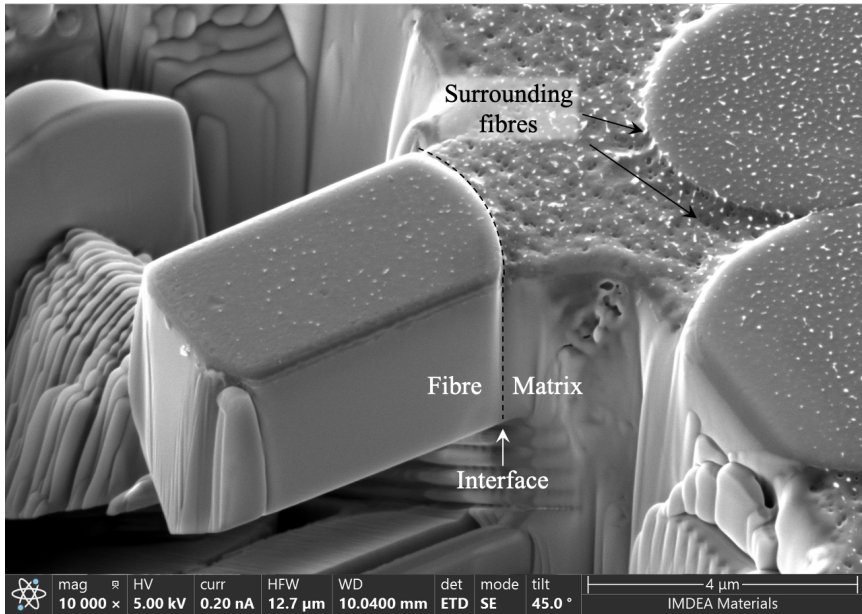


Figure 2.4: SEM image of a ready to be tested micro-cantilever beam

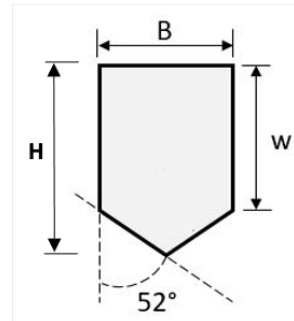
all the samples in each campaign are numbered so that C3.1 uniquely point the first specimen of the third campaign. To comprehensively explore the feasibility of testing the interface via MCT, different cantilever beam proportion and testing mode were verified. With this purpose the specimens differs as follow:

- C3, C4 and C6 were fabricated with a more than halved cross section height (H) respect to the remaining C1, C2 and C5 campaigns. This allowed to investigate the effect of different section shape on the tests outcomes. The reduced height section, referred as *Slim* section, promotes more bending over shear if compared to the other *Regular* one.
- C5 was fabricated with a reduced cantilever average length (L), to evaluate its effect on results. It was referred as *Short* cantilever.

- a notch was carved along the C2 specimens upper edge of the fibre-matrix interface, with the purpose to promote the debonding initiation and guide the propagation. A C2.3 specimen details can be seen in the SEM image of Figure 2.5.
- C6 represented a benchmark specimens group, they were manufactured from the matrix alone. There was neither fibre nor interface. They were tested to characterize the matrix fracture response and discern, on the other test results, a proper fibre-matrix debonding to a crack propagation kinked into the matrix.

Table 2.3: Cross section geometrical and cantilever length measurements, reported as average value μ and standard deviation Σ for each of the performed experimental preparation campaigns.

Camp.	L [μm]	H [μm]	B [μm]	W [μm]	Area [μm^2]	Cross section geometry
C1	μ	4.861	3.883	2.793	2.248	8.562
	Σ	0.151	0.309	0.082	0.197	0.574
C2	μ	4.938	4.687	2.803	2.916	10.658
	Σ	0.213	0.465	0.289	0.379	1.748
C3	μ	4.293	2.567	2.532	1.168	4.731
	Σ	0.337	0.095	0.107	0.217	0.245
C4	μ	4.735	2.313	2.049	1.128	3.527
	Σ	0.149	0.187	0.115	0.067	0.379
C5	μ	3.802	4.072	2.912	2.401	9.426
	Σ	0.211	0.115	0.368	0.081	1.29
C6	μ	4.523	2.581	1.984	1.091	3.643
	Σ	0.116	0.211	0.212	0.117	0.529



2.4 Testing mode

Since the main aim of the present work is the interface characterization both in mode I and II, a proper way to isolate each failure mode was proposed. The shear load was promoted by testing the specimens adopting a flat tip nano-indenter, with a diameter equals to $3\mu m$. In

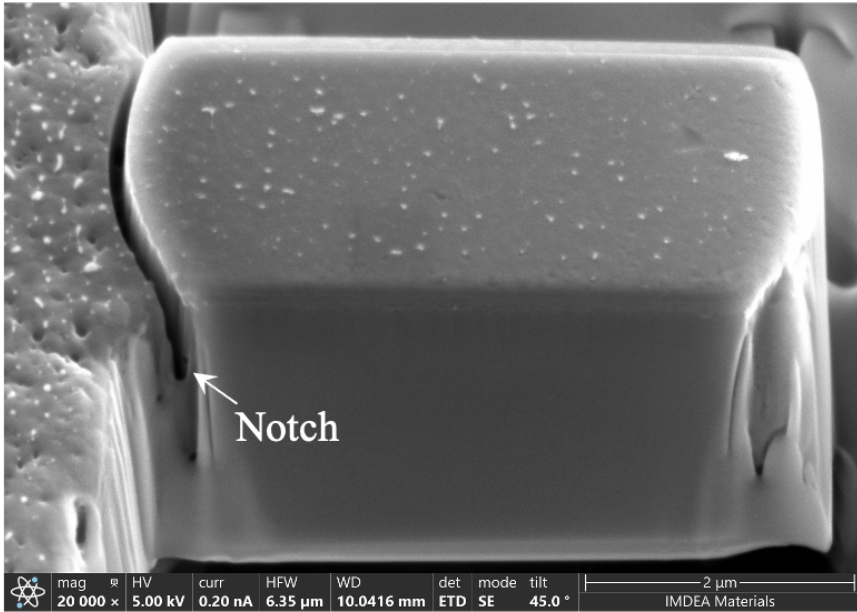


Figure 2.5: SEM image of C2.3 specimen with the notch highlighted

this way the pressure resultant force is applied close to the cantilever interface section, reducing bending and increasing shear. On the other hand, to perform a mode I characterization, an opening strain must arise at the interface. This occurs at the upper region of the interface surface, when a bending moment is applied. Despite it is not a pure opening, it results to be the only way to perform a mode I test on this geometry, since the whole specimen dimensions prevent the adoption of any alternative clamping of the cantilever free end. The mode I characterization was performed by applying the load as far as possible from the interface surface, by adopting a cube corner tip to concentrate the load at one application point. A schematization of both the test configuration is reported in Figure 2.6.

The micro-cantilevers were tested in a *Hysitron TI950* nano-indenter machine. The nano-indenter position was operated via atomic force microscope (AFM). It is a widely applied scanning probe microscope technique to obtain topographic features of sample surfaces in a height image on both insulating and conducting structures with a nanome-

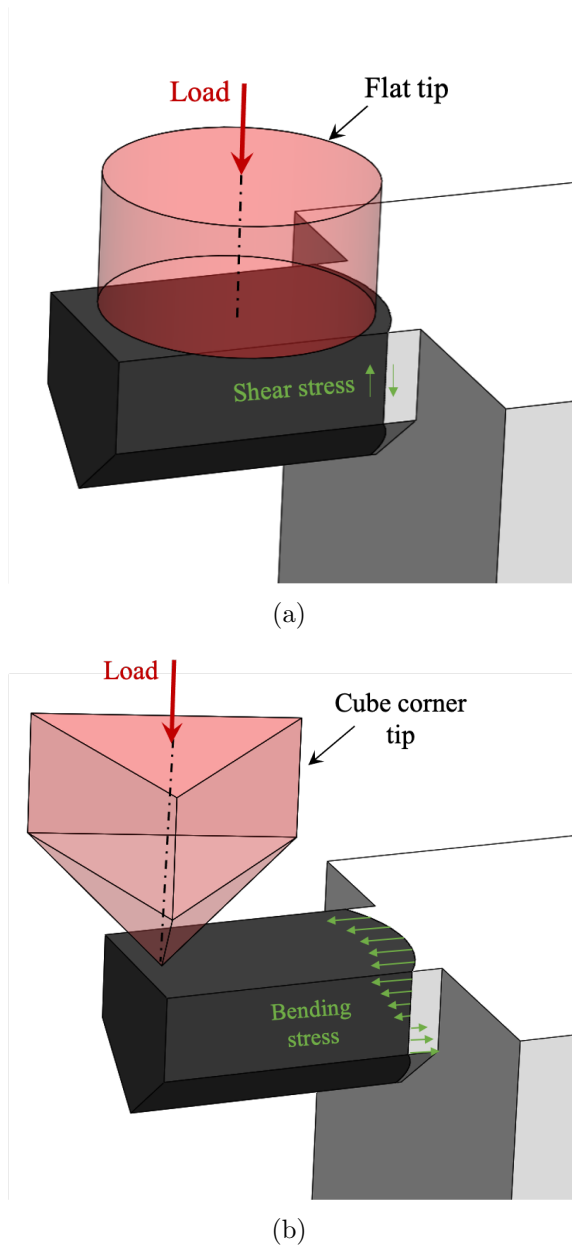


Figure 2.6: Schematic representation of mode II test configuration (a), with flat indenter tip and shear stress at interface, and mode I test (b) with cube corner indenter tip and bending stress distribution.

ter resolution. Also for the texts execution the specimens grouping by campaign was followed. In Table 2.4, for each campaign the number

of tested specimens, the testing mode and the section and cantilever characteristics were reported.

Table 2.4: micro-cantilever test groups

Camp.	Test n°	Testing mode	Section	Samples description
C1	12	Mode I	Regular	/
C2	12	Mode I	Regular	Notched
C3	6	Mode I	Slim	/
C4	16	Mode II	Slim	/
C5	4	Mode II	Regular	Short beam
C6	4	Mode I	Slim	full matrix

The tests were performed under displacement control and, to monitoring the debonding progress, a group of tests was performed by cyclically increasing the displacement. The indenter velocity was set to 5 nm/min . According to the *Rueda Ruiz* [2] findings about strain rate effect on *IM7-8552* mechanical response, the imposed velocity represents a quasi-static loading condition. The experimental outcomes were collected according to specimens campaign production and reported in form of measured load average value and deviation vs. imposed indenter displacement.

Chapter 3

Experimental Results

3.1 Mode I test results

The experimental campaigns conducted to characterize the mode I interface debonding, involved the specimens groups from C1 to C3. These represents the group of specimens tested by cyclically increasing the load and by adopting the cube corner tip. Following the experimental outcomes are presented. First the results of some sample tests will be discussed, on these the failure mechanism will be explained and some critical issues highlighted. Then the cumulative results of the whole mode I testing campaign will be presented. In Figure 3.1(a) the SEM image of the C1.3 tested specimens is reported and the debonded fibre-matrix interface highlighted. The debonding initiated at the upper interface edge and properly propagated on its surface, thus the test was considered successfully executed. The corresponding measured force over indenter depth curve is depicted in Figure 3.1(b). The effect of cyclical displacement load application is clearly visible (blue curve). It shows a first linear force trend, corresponding to the pre-debonding phase, whose slope K represents the specimen initial stiffness. Then a load drop, produced by the debonding initiation, can be seen. The following force plateau is representative of the interface damage stable

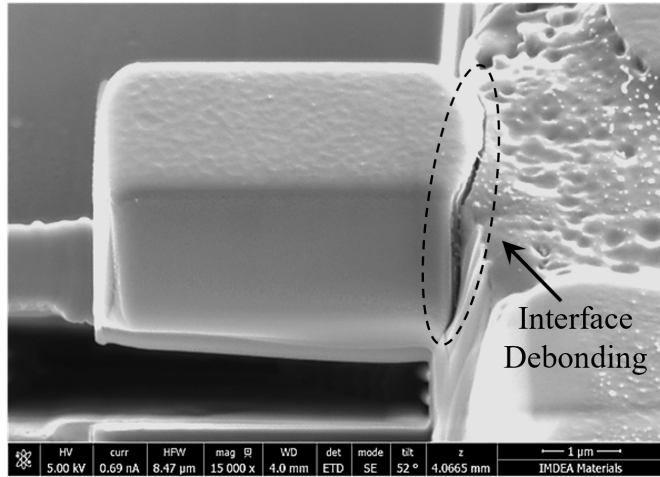
propagation phase. The red dotted line indicates the load vs depth, in pre-initiation and stable propagation conditions, under not cyclically applied displacement.

As mentioned in presenting the experimental campaign classification, a group of specimens were manufactured by milling a notch on the upper edge of the interface with the purpose to promote a proper debonding initiation. The C3.2 specimen was among them and resulted in a correct debonding. A clean and clear debonding process can be seen (Figure 3.2(a)) on both the fibre and matrix surfaces, as well as the indentation produced by the cube corner tip on the microcantilever beam top surface is visible. It may also be appreciated from the SEM image a matrix crack localized on the side edge of the interface. This parasite matrix damage resulted to be a quite frequent phenomenon. It is due to a stress concentration in that regions which can be ascribed to the shape of both the interface surface and specimen geometry. The respective experimental load over depth curve, reported in Figure 3.2(b), shows the same trend of the below described C1.3 test.

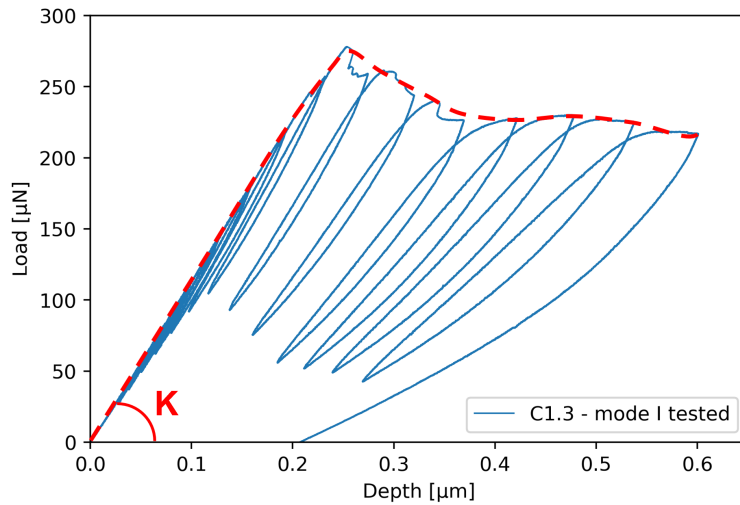
Most critical respect to the tests success was the kinking of whole the debonding front inside of the matrix. This phenomenon resulted quite frequent in the slim section mode I tested specimens. In these cases the debonding correctly initiates at the upper interface edge, but at the beginning of the stable propagation, a matrix crack is triggered. Thus the test proceeds on a favorable, 45° oriented, crack path. Since the migration of the whole debonding front into the matrix, these were considered failed tests, contrary to the tests where the matrix cracking interested only a small region close to the interface surface side edges (i.e. C3.2). An example of invalid test outcome is reported in Figure 3.3, it is the C3.4 specimen. The matrix crack propagation is clearly visible and it interests all the specimen width.

The related experimental curves showed both a much higher maximum force and depth, respect to the properly proceeded tests.

As below reported for the two tests C1.3 and C3.2, the experimen-

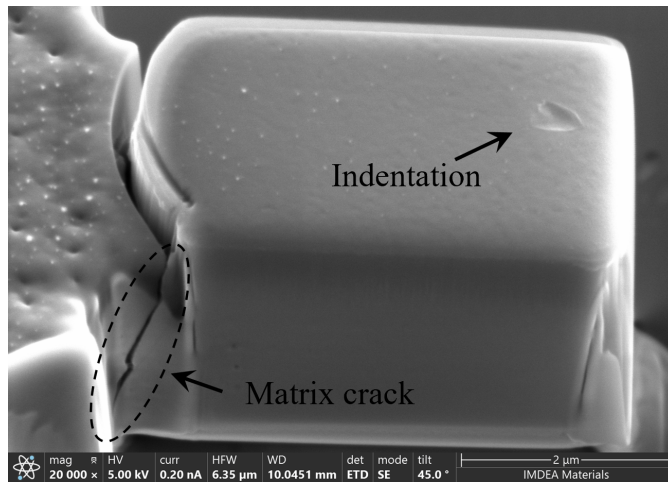


(a)

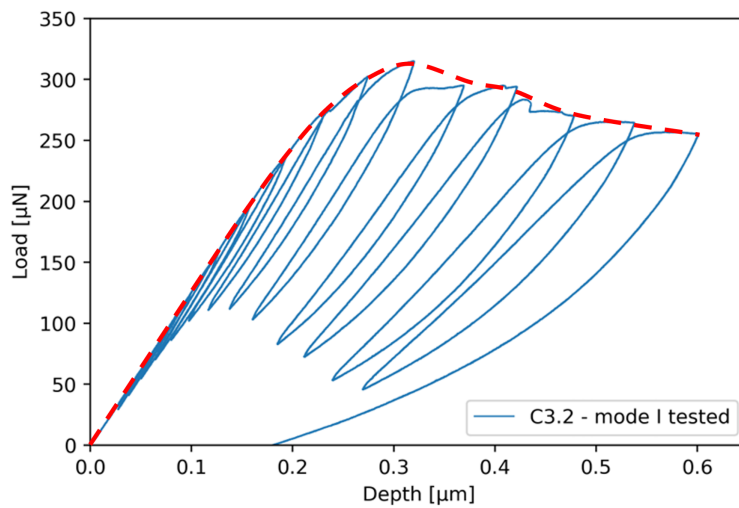


(b)

Figure 3.1: C1.3 mode I tested specimens, with interface debonded highlighted (a) and the respective experimental load vs depth curve (b)



(a)



(b)

Figure 3.2: C3.2 mode I tested notched specimens, with parasite matrix crack and cube corner indentation highlighted (a) and the respective experimental load vs depth curve (b)

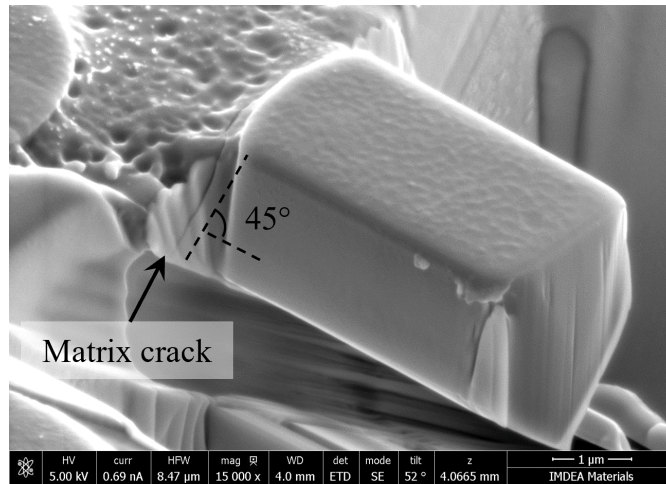


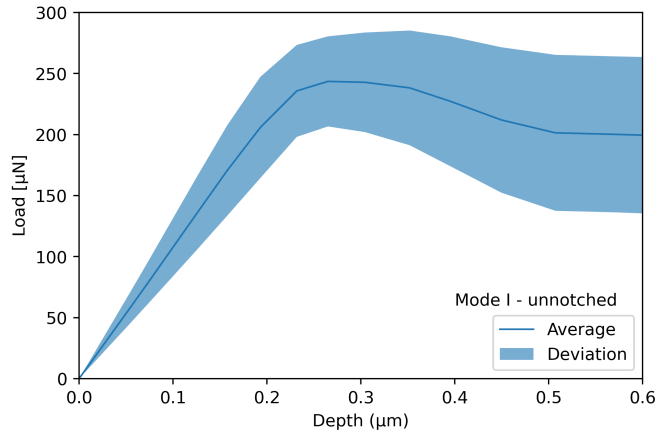
Figure 3.3: SEM image of C3.4 specimen with whole debonding front kinked and propagated into the matrix.

tal outcomes related to mode I testing conditions were analyzed and post-processed. The properly debonded specimens were identified and the correspondent measured load over continuously applied depth retrieved. A statistical calculation, namely the average and the standard deviation of the load over the depth, was made.

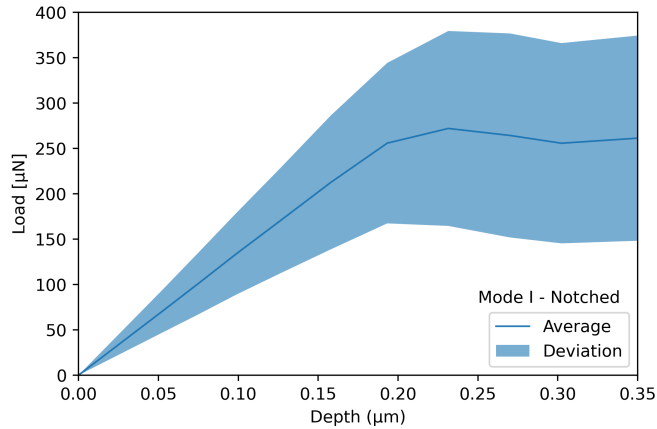
The unnotched specimens results are reported in Figure 3.4(a), while the notched specimens results in Figure 3.4(b). The absolute value of the average maximum force resulted quite similar, while the corresponding depth is higher for the unnotched specimens.

To better understand the effectiveness of the notch presence on the tests execution success and repeatability, a comparison between the notched and the unnotched specimens test results were conducted. Since the two specimens type were manufactured in different preparation campaign, they presented difference in cross-section dimensions, which were instead found to not significantly affect the specimens within the same campaign. To conduct the comparison, the results were normalized respect to the effective cross-section area. Thus, the normalized load over depth was considered and reported in Figure 3.5.

The two group of normalized results showed the same initial stiff-



(a)



(b)

Figure 3.4: Average and standard deviation of applied load over depth, for unnotched (a) and notched (b) specimens, tested in mode I.

ness and a similar trend in the debonding evolution. The notched specimens resulted instead in a lower maximum force, probably due to the presence of the notch itself. However, the most significant results emerged from the comparison, is related to the amplitude of the standard deviation. The presence of the notch appears to lead a greater results dispersion, if compared to that one of the unnotched specimens. Since the presence of the notch did not lead to an higher number of succeeded tests, its adoption was discarded as a functional solution to

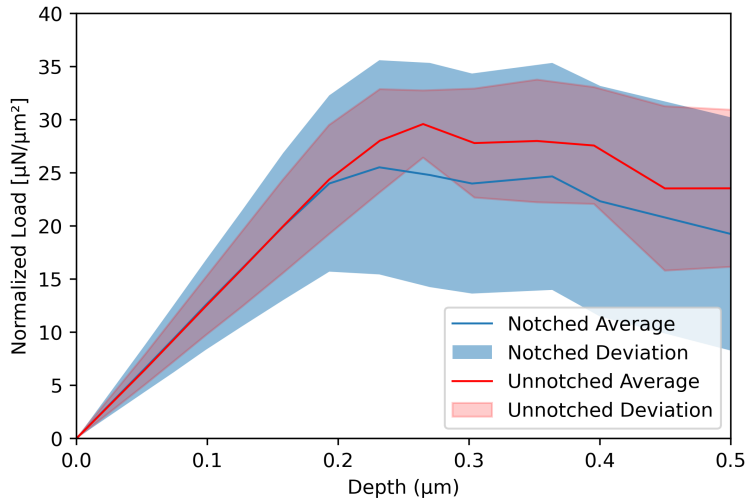


Figure 3.5: Normalized with respect to the cross-section area load over depth, for the unnotched and notched specimens tested in mode I.

include in the proposed experimental methodology. Similarly the results provided by the C3 campaign showed the slim section produced more chance of kinking of the debonding into the matrix. Therefore the most accurate results were obtained from the C1 group of specimens which were considered for the mode I calibration and validation of the numerical model.

3.2 Matrix carved specimens results

As mentioned, the presence of matrix crack resulted frequent over the conducted interface testing. In some cases the phenomenon extent was easy to identify, while in other cases the tested specimen SEM images were inadequate to identify the proper or the improper tests outcome. Thus, the purpose in testing specimens made of matrix without any interface, was to investigate the matrix crack behaviour. It led to extrapolate a benchmark to identify those tests, among the other campaigns, where the matrix crack was the dominated damage mechanism. This class of tests represented the C6 preparation campaign, tested un-

der mode I condition adopting the cube-corner indenter tip. All the tested specimens resulted in the same damage mechanisms, here reported in Figure 3.6 for the C6.4. The damage naturally initiate close to the constrained micro-beam section and then propagates on a path 45° oriented as seen in some not succeeded interface tests.

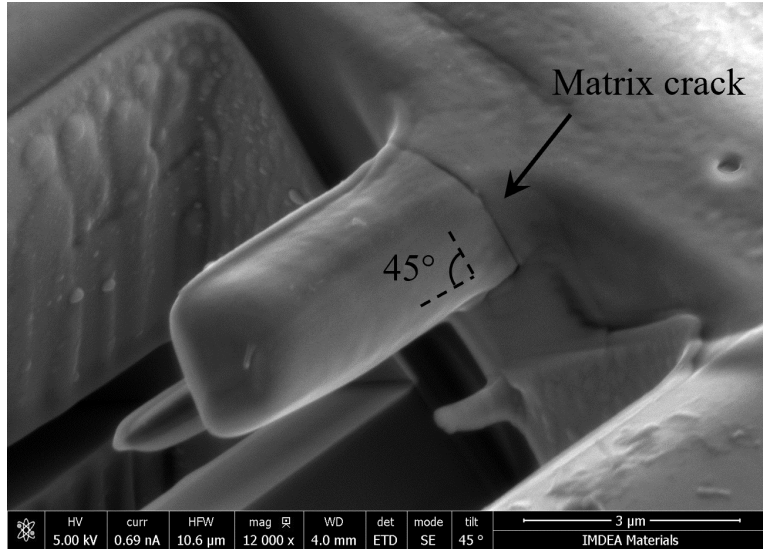


Figure 3.6: C6.4 tested specimen with matrix crack highlighted.

The outcomes in term of load over displacement curves are collected in the form of average values and standard deviation in Figure 3.7. The trend of load vs depth looks quite linear, showing a smooth change of slope around the $0.3\mu\text{m}$ of depth. It is probably due to a combination of crack initiation and plastic deformation of matrix. A detailed discussion about the contribution of both will be presented in the numerical results section. The crack propagation results to be quite rapid, since no reduction in load can be detected before its drop to zero.

The presented results about matrix carved specimens failure, were compared to the interface tested specimens exhibited an improper failure. These latter showed the same damage mechanisms detected in the matrix carved C6 specimens. It suggests for the considered *IM7-8552* the mode I interface strength results to be comparable with the matrix

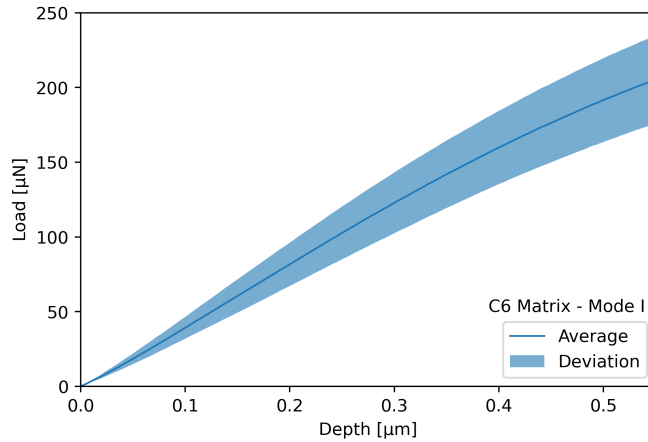


Figure 3.7: Average and standard deviation of applied load over depth for C6 specimens made of matrix.

strength.

3.3 Mode II test results

The experimental campaigns conducted to characterize the mode II interface debonding, involved the specimens groups C4 and C5. The C5 specimens group were the first attempt to estimate the mode II behaviour. They were tested by adopting the cube corner indenter tip and, presenting a reduced micro beam length, were tested by applying the load as close to the interface as possible. The load was also imposed in form of cyclical displacement increments. The preliminary results showed the cube corner sharp tip induced an improper test outcomes, by mean the indenter penetrated the micro beam surface not inducing a proper debonding. The effect of this test configuration can be appreciated in Figure 3.8. The punctual load, applied close to the fibre-matrix interface, produced a specimen damage leads to a destructive test outcome.

The related load over depth curve (Figure 3.9), showed a distinctive rising load trend over the entire test execution. Only a load drop strad-

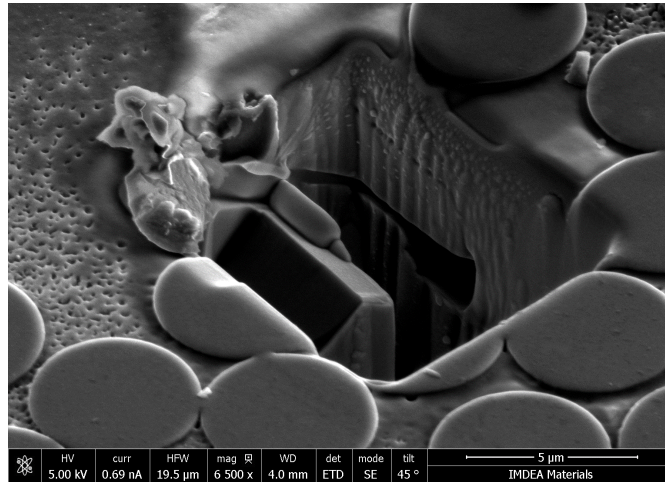


Figure 3.8: C5.1 specimen failed mode II test, conducted adopting the cube corner indenter tip positioned close to the fibre-matrix interface.

ding $0.2\mu m$ of depth was visible. It matched to a damage initiation which produced a reduction in the curve slope (from K to K'), but no propagation followed this drop. The test instead continued with the new slope up to the termination caused by the excessive load reaching ($1400\mu N$). The author presumes the described behaviour indicates the specimens did not deform as expected, thus the curve slope is not only the specimen stiffness, but it is also the hardness offered to the indentation. Further, the cyclic loading ramps, identified by the black lines in Figure 3.9, do not showed the characteristic slope reduction, indicating the specimen compliance increase due to the damage propagation.

To successfully complete the tests, the indenter needs to be positioned far from the interface. The average distance of the load application point from the interface, estimated via AFM measurements, leading to a proper tests outcomes was estimated as equals to $1.806 \pm 0.947\mu m$. The remaining C4 group specimens were thus tested in this last configuration by cyclically applying the load. The related experimental load over depth curves, are showed in Figure 3.10 in the form of peak trend curve.

In this modified test configuration a reasonable outcome is reached.

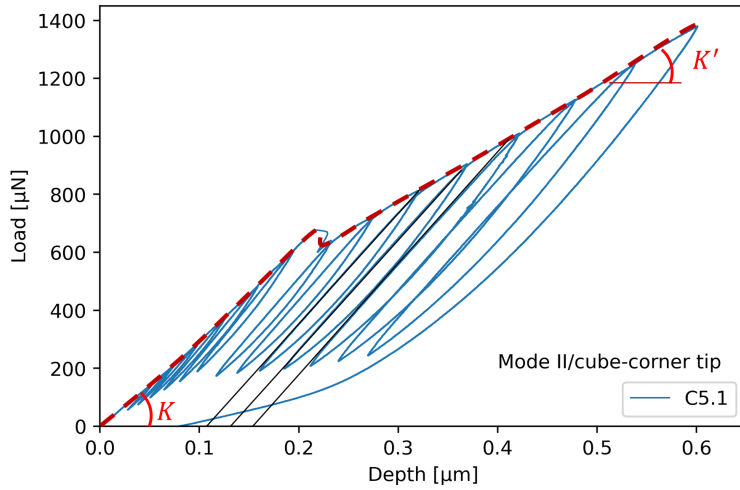


Figure 3.9: C5.1 specimen load over depth curve, with highlighted the cyclic loading ramps (black lines) and the whole tests stiffness K and K' .

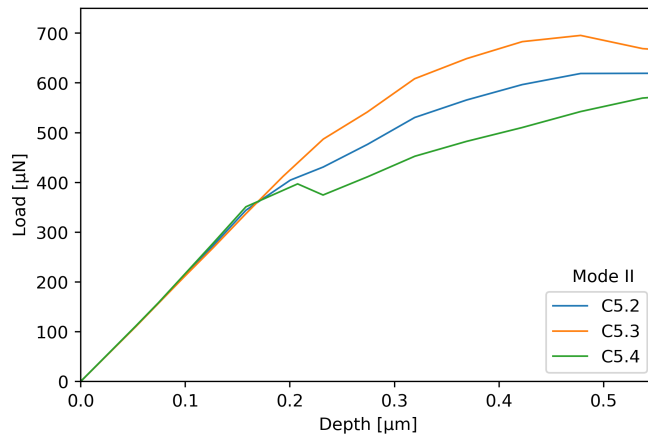


Figure 3.10: C5.2 to C5.4 specimen test results in term of load over depth curve, the tests ere conducted by adopting cube-corner tip and applying the load as closer to the interface as possible.

The remaining specimens from C5.2 to C5.4, showed the same initial stiffness and a linear path extending up to a load value of $350\mu N$. Then a progressive slope reduction is always visible and the average maximum force of $600\mu N$ looks to be a feasible value. However, The amount of successfully tested specimens do not allows to perform sta-

tistical calculation or evaluate the configuration repeatability. Further, the induced stress fields resulted to be a combination of mode I and mode II, since the value of load application point distance from the interface. Therefore this testing configuration was discarded and the mode II tests on C4 specimens group executed by adopting the flat tip rather than the cube corner tip.

The adoption of the indenter flat tip, as discussed in section 2.4, allowed both to avoid undesired indenter penetration and apply the load closer to the interface border. The 16 tests performed with this configuration resulted successful. They showed a trend quite similar to the properly performed C5 specimens, here reported in form of average and standard deviation load over depth in Figure 3.11.

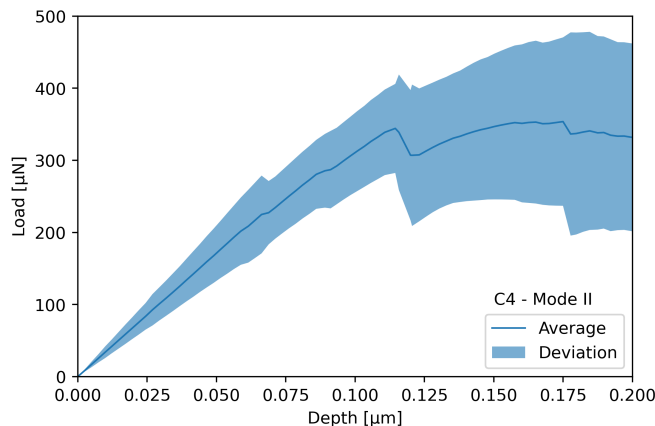
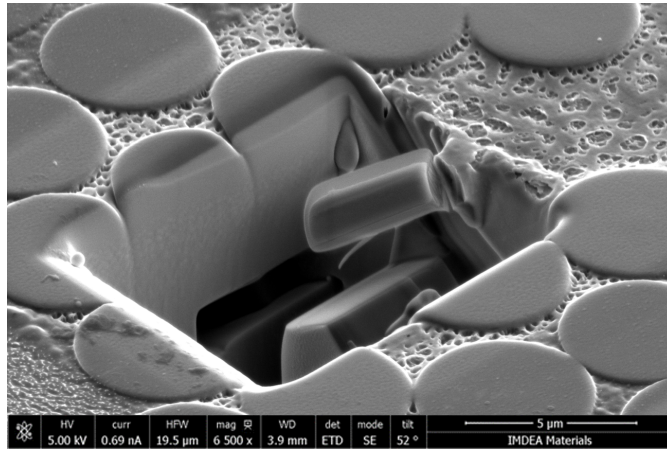
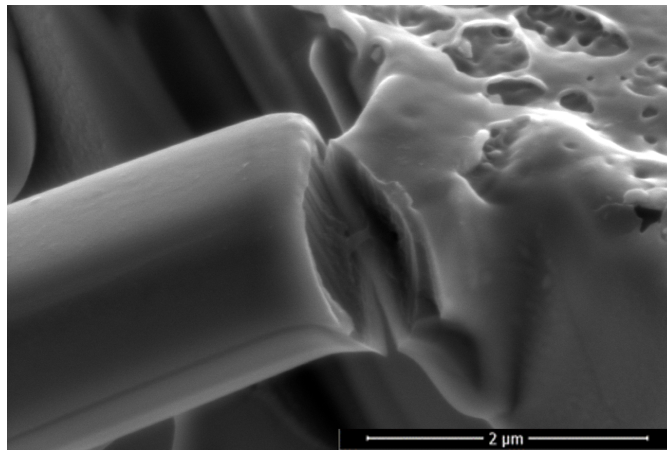


Figure 3.11: Average and standard deviation of load over depth for C4 specimens group, tested in mode II and adopting the flat indenter tip.

Under these testing condition the linear section of the curves stretches until a load drop close to a load equals to $350 \pm 50 \mu N$. Then the curve proceeds with the same slope that quickly decreases until the abrupt failure. All the tested specimens resulted in the complete detachment of the micro beam from the resin interface, as visible in Figure 3.12(a) for the C4.11 specimen. It also produced a clean and searchable debonded surface on both the fibre and the matrix (Figure 3.12(b)).



(a)



(b)

Figure 3.12: SEM image of mode II tested C4.11 specimen, the complete micro beam detachment is visible (a) as well as a detail of the debonding surface (b).

Chapter 4

Computational Methods

4.1 Introduction

Similarly to the interface testing methods presented in section 1.6.2 and adopted in literature, the proposed MCT only provide direct measurements of indenter displacement and corresponding force (section 2.4). This is because of the reduced dimension of specimens and the difficulties in test performing. These results are largely inadequate to investigate the interface debonding phenomenon. Furthermore, as shown in section 6.1, the analytical background presents a limited range of applicability since the approximation in the description of the phenomenon and the limitation of continuum mechanics approach to the pre-debonding status. Combination of numerical tools and experimental activities is a well-established practice. Many of the previously mentioned scientific works enforced computational methodologies to deepen several aspects of the problem otherwise unknowable. In this work the interface properties of *IM7-8552* were identified via FEM, on the base of the proposed experimental methodology results. In this chapter the numerical model implementation and its calibration, based on the literature available material properties and the conducted experimental outcomes, are reported. The model geometry and compu-

tational settings are detailed and a brief theoretical background about CZM principles presented. Thus the CZM implementation into the FE model is described.

4.2 Numerical model

The experimentally proposed microcantilever test was numerically implemented on *Abaqus/Standard* FEA software. A 3D geometry of the single fibre cantilever beam, embedded in a matrix block and subjected to the indenter, was reproduced. The cantilever beam dimensions were assigned according to the measurements experimentally acquired via SEM and reported in Table 2.3. Separate models were realized for each of the examined preparation campaigns (section 2.3). An illustrative image of the obtained FEM is here reported in Figure 4.1, in it are also showed the local fibre reference system (1, 2, 3) and the global model reference system (x, y, z). It should be emphasized the fibre material properties, reported in Table 2.1, are referred to the local reference system. The material properties were implemented into the model by imposing an isotropic behaviour for the matrix and a transversely isotropic response for the fibre. The fibre element reference system was also oriented according to the fibre properties orientation.

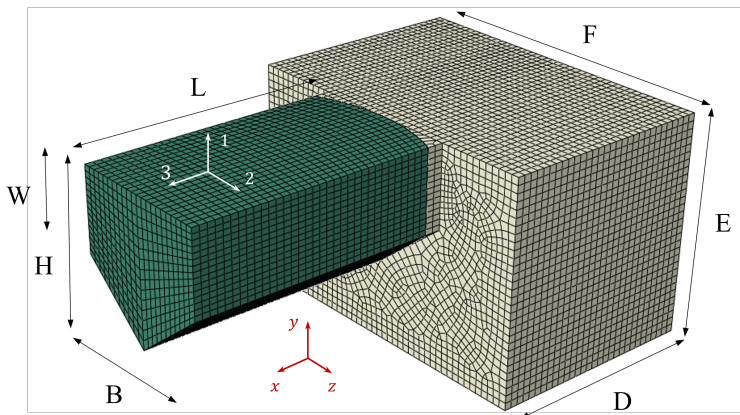


Figure 4.1

The whole model was meshed by adopting fully integrated eight node linear brick (C3D8) elements and a uniform element size equals to $0.1\mu m$ was imposed. This resulted to be the highest possible mesh refinement, since a smaller element size requires infeasible computational effort. A structured mesh generation strategy was imposed. The boundary conditions, representing the reactions of the surrounding material not reported into the model, were applied to the matrix block sides. Each of the block faces was constrained by suppressing all the in-plane displacements. The two examined experimental methodologies, namely mode I and mode II tests, were reproduced. The indenters described in Figure 2.6 were modelled as analytical rigid surfaces and positioned over the cantilever beam according to the AFM experimental measurements. The sharp tip characterizing the cube corner indenter, could promote calculus convergence problems. To avoid these difficulties, it was approximated to an hemispherical surface with a diameter equals to $2\mu m$. Each indenter was rigidly fixed to a control node, which was constrained by suppressing all the degrees on freedom, less than the displacement on the loading direction (y axis). The load condition, represented by the indenter displacement was imposed in the form of velocity and set equals to $5nm/min$, according to the experimental procedure. For the indenter tip to fibre contact interaction a frictionless surface-to-surface contact was enabled by selecting the indenter rigid surface as master. The resulting problem mathematics dimensions were collected in Table 4.1.

Table 4.1: Computational problem size

Number of elements	124918
Number of nodes	136181
Total number of variables	401292
Calculation time*	193.5 hours

*The simulations were run on the *IMDEA Material institute* cluster system, on a 20-core 4.5 Ghz *Intel Xeon* processor with 128 Gb of RAM available.

4.3 Cohesive zone model

The debonding phenomenon was implemented into the numerical model by applying a CZM on the fibre and matrix in contact surfaces. Following a description of the adopted cohesive algorithm operating principles is reported. The fibre-matrix interface cohesive behavior was implemented in *Abaqus* in form of available cohesive contact type. It allows to model contact interactions between specific surfaces in a model.

4.3.1 Contact detection

Contact interactions between bodies can be enabled in the FEA ambient through a class of algorithms enforced to the superficial nodes of the involved in contact bodies. The aims of which is address whether two or more bodies are in contact, where the contact location is, the amount of contact forces interesting the contact surface and any relative interface motion after contact. The contact condition is classified as a boundary nonlinearity, because of the discontinuity in contact forces at the beginning of the contact and at the transition between sticking and sliding in frictional contact. The initiation is mathematically formalised by the punctual mutual tangency between two in contact surfaces.

From that limit condition the contact proceeds involving an increasing number pairing nodes. Since the solid are discretized, the surfaces consists in a succession of small plane region or, in the case of bidimensional problems, in a succession of segments linked by nodes. This intrinsic irregularity, plus the possible different surface curvatures, preclude a perfect matching of the surfaces during contact. This leads to contact penetration and gaps all over the surface that needs to be managed by the software to return a proper response of the touching bodies. This capability is enforce in form of small-sliding or the finite-sliding models. The small-sliding formulation poses the contacting surfaces can undergo only small relative sliding while ar-

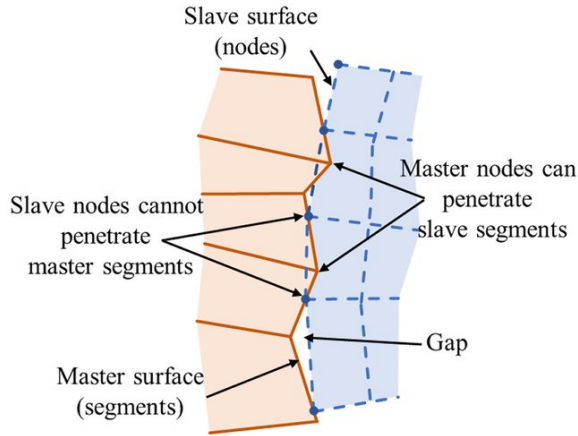


Figure 4.2: Schematic representation of a 2D master-slave surface contact interaction.

bitrary rotations of the bodies are permitted. A kinematic constraint that the slave surface nodes do not penetrate the master surface is then enforced. The small-sliding formulation is appropriate if the relative motion of the two surfaces is less than a small proportion of the characteristic length of the elements faces. On the other hand, the finite-sliding allows any arbitrary motion of the surfaces in contact, resulting computationally more expensive than small-sliding contact and resulting in a less efficient analysis. These approaches need to define a *master* (contact guiding) and a *slave* (guided) surfaces. As graphically reported in Figure 4.2 for a bidimensional case, the slave surface nodes cannot penetrate the masters surface segments, while no restriction are imposed to the master surface nodes in penetrating the slave surface segments. The enforcement of this principle can be punctually made, by controlling each slave node independently (node to surface), or globally made by averaging over a regions nearby slave nodes (surface to surface). In node to surface formulation the contact direction is based on the master surface normal and the only information needed about slave surface is the location and surface area associated with each node. The direction of the slave surface normal and slave surface curvature are not relevant. Thus, the slave surface can be defined as a

node-based surface. The surface to surface instead considers the shape of both the slave and master surfaces in the region of contact. The averaging regions, for contact control, are approximately centered on slave nodes, so each contact constraint considers a group of adjacent slave nodes. Some penetration may be observed at individual nodes, however large penetrations of master nodes into the slave surface do not occur with this discretization [51].

4.3.2 Contact pairing algorithms

The formalization of contact interactions between surfaces in *Abaqus* needs the definition of a constitutive model describing the normal and sliding contact behaviour. The normal behaviour is defined through a contact pressure p , function of the gap h between the contact involved surfaces and in any point normal to it. The adopted in the present work *hard contact* algorithm, can be expressed as reported in (4.1). It postulate the gap zeroing produce a not null pressure. No overclosure are permitted in this contact formulation ($h \not\geq 0$).

$$h < 0 \rightarrow p = 0 \quad \cup \quad h = 0 \rightarrow p > 0 \quad (4.1)$$

The sliding behaviour was set governed by an Coulomb frictional model. It assumes no relative motion occurs if the equivalent frictional stress τ_{eq} is less than the critical stress τ_{cr} . If the equivalent stress is at the critical stress slips can occurs. The frictional stress is proportional to the contact pressure p via the frictional coefficient μ (4.2), which is user assigned and can be also defined as function of other variables (i.e. temperature, slip rate etc.).

$$\tau_{eq} = \sqrt{\tau_1 + \tau_2} = \mu \cdot p \quad (4.2)$$

The effective computational implementation of the described Coulomb model is not strictly rigorous, since the condition is not applied point-

wise but weighted over a small area. This non-local friction model condition, punctually allows small relative sliding also before τ_{cr} is reached. The frictional stress is governed by a stiff elastic behavior, with the stiffness κ computed observing a condition of maximum allowable sliding γ_{cr} at critical stress reaching, so that results $\kappa = \tau_{cr}/\gamma_{cr}$. Under isotropic friction conditions, the slip and the frictional stress direction coincide and the slip amount γ in frictional sliding regime is governed by the slip rate $\dot{\gamma}$. The critical slip value may be user specified, otherwise it is set by default to 0.5% of the average length of all contact elements in the model. A described model refinement can be operate by adopting a Lagrange multiplier method to ensure the relative motion in absence of slip is precisely zero. The perfect sticking constraint, resulting from this implementation, has an increased adherence to the physical problem but produces the analysis cost rising and may prevent the Newton algorithm convergence.

4.3.3 Cohesive model theoretical approach

In this subsection governing equations of a debonding elastic solids under a small strain deformation regime are presented. For simplicity a static two dimensional solid with an internal interface is considered and schematically represented in Figure 4.3. The computational domain $\Omega \subset \mathbb{R}^2$ and its boundary $\Gamma \equiv \partial\Omega$ can be defined. We assume there is only one internal interface denoted by $\bar{\Gamma}$ that split the solid into two halves $\Omega_{m=1,2}$ so that $\Omega = \Omega_1 \cup \Omega_2$. The interface surfaces outwards unit normal are denoted as n_1 and n_2 .

Before decohesion, the two subdomains are perfectly bonded by means the displacement field is continuous across $\bar{\Gamma}$. If a failure criterion is satisfied, discontinuities in the displacement field across $\bar{\Gamma}$ are allowed to model the decohesion. Governing equations for the stages prior and after debonding initiation are following discussed.

Prior to debonding initiation, the governing equation of linear elas-

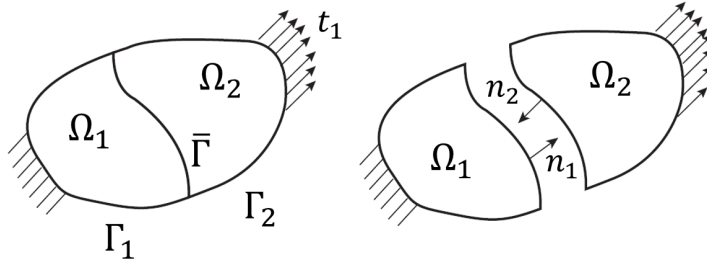


Figure 4.3: Computational domain with an internal interface.

tic problem are following reported in equations from (4.3a) to (4.3e).

$$-\nabla \cdot \boldsymbol{\sigma}_m = \mathbf{b}_m \quad \text{on} \quad \Omega_m \quad (4.3a)$$

$$\mathbf{u}_m = \bar{\mathbf{u}}_m \quad \text{on} \quad \Gamma_m \quad (4.3b)$$

$$\boldsymbol{\sigma}_m \cdot \mathbf{n}_m = \bar{\mathbf{t}}_m \quad \text{on} \quad \Gamma_m \quad (4.3c)$$

$$\mathbf{u}_1 = \mathbf{u}_2 \quad \text{on} \quad \bar{\Gamma} \quad (4.3d)$$

$$\boldsymbol{\sigma}_1 \cdot \mathbf{n}_1 = -\boldsymbol{\sigma}_2 \cdot \mathbf{n}_2 \quad \text{on} \quad \bar{\Gamma} \quad (4.3e)$$

Where $\boldsymbol{\sigma}_m$ and \mathbf{u}_m are respectively the stress and displacement fields. $\bar{\mathbf{u}}_m$ and $\bar{\mathbf{t}}_m$ the prescribed displacements and traction. The last two equations (4.3d) and (4.3e) ensure the displacements and traction continuity across $\bar{\Gamma}$.

Once the debonding initiated, the continuity of the displacement field across $\bar{\Gamma}$ is missing and the interface interaction is governed by a cohesive law. Mathematically it means the last two equations (4.3d) and (4.3e) are replaced by the relation reported in equations (4.4a) and (4.4b).

$$-\boldsymbol{\sigma}_1 \cdot \mathbf{n}_1 = \boldsymbol{\sigma}_2 \cdot \mathbf{n}_2 = \mathbf{t} \quad \text{on} \quad \bar{\Gamma} \quad (4.4a)$$

$$\mathbf{t} = \mathbf{t}(\boldsymbol{\delta}, \boldsymbol{\zeta}) \quad \text{on} \quad \bar{\Gamma} \quad (4.4b)$$

Where $\mathbf{t}(\boldsymbol{\delta}, \boldsymbol{\zeta})$ is the cohesive traction vector, $\boldsymbol{\delta}$ is the relative displacement between the no more in contact nodes of the interface surface and $\boldsymbol{\zeta}$ denotes a set of history variables modeling the irreversibility of the debonding process. The presented continuum mechanics problem is then retrieved into the FEA software. The solid is discretized into volumetric elements and zero-thickness interface elements along the interface path, as graphically reported in Figure 4.4(a). The cohesive algorithm operate as a spring, of stiffness \mathbf{K} , linking the initially in contact nodes of the $\Omega_{m=1,2}$ solid partitions.

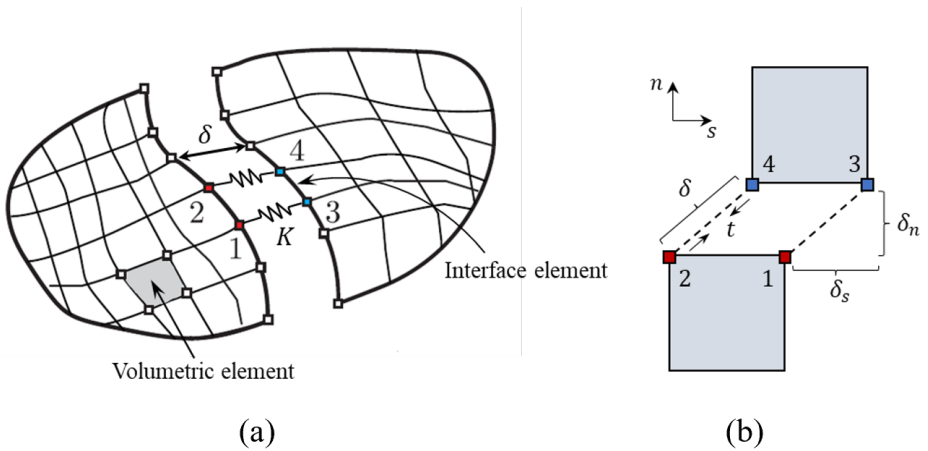


Figure 4.4: FE problem discretization (a), with interface elements and cohesive interaction stiffness K , and schematization of two couples of nodes experiencing a cohesive contact (b) with the relative displacement components δ_n and δ_s .

A schematic representation of two couples of nodes experiencing a cohesive contact, is reported in Figure 4.4(b). The local reference system (n, s, v) has the n axis oriented according to the outward unit normal to the contact surface, and the s and v axes lying on the contact surface. In this reference system δ can be split in three components:

- the normal separation δ_n is defined as positive under the impenetrability principle of bodies experiencing the contact.

- the two shear separation δ_s and δ_v that are the two in plane sliding displacements.

The relative displacement modulus δ can be obtained as a function of the introduced components as reported in (4.5). The Macaulay bracket $\langle \cdot \rangle$ indicates ($\langle \delta_n \rangle = \delta_n$ if $\delta_n > 0 \cup \langle \delta_n \rangle = 0$ if $\delta_n < 0$)

$$\delta = \sqrt{\langle \delta_n \rangle^2 + \delta_s^2 + \delta_v^2} \quad (4.5)$$

The decohesion initiation and propagation is defined in the model by a traction-separation law. It relates the cohesive stress t to the relative displacement δ by assuming an initially linear elastic behavior followed by the initiation and evolution of damage. The initial elastic behaviour can be written as reported in (4.6). Where the K_{ij} are the components of the elastic constitutive matrix \mathbf{K} which represents the penalty stiffness of the cohesive algorithm before damage. The t_{ij} and δ_{ij} are cohesive stress and relative displacements components. By assuming the traction-separation behaviours, in the n, s, v directions uncoupled, all the components $K_{ij, i \neq j} = 0$.

$$\mathbf{t} = \begin{Bmatrix} t_n \\ t_s \\ t_v \end{Bmatrix} = \begin{bmatrix} K_{nn} & K_{ns} & K_{nv} \\ K_{sn} & K_{ss} & K_{sv} \\ K_{vn} & K_{vs} & K_{vv} \end{bmatrix} \cdot \begin{Bmatrix} \delta_n \\ \delta_s \\ \delta_v \end{Bmatrix} = \mathbf{K} \cdot \boldsymbol{\delta} \quad (4.6)$$

The value of the penalty stiffness must be high enough to prevent both interpenetration of the debonded faces and artificial compliance from being introduced into the model by the cohesive elements. Several guidelines were proposed in literature to estimate the penalty stiffness of a cohesive law. In any case it is needed the compliance of the bulk material is much larger than the initial cohesive law compliance. Therefore, as default, the software set the K_{ij} values as equal to at least one tenth of the adhering material elastic modulus divided by its volume elements characteristic length l_c .

Under these assumptions the traction-separation laws for both nor-

mal (mode I) e shear (mode II) modes can be graphically represented on a traction vs relative displacement diagram (Figure 4.5). The mode II traction-separation law, here reported for the shear direction s , is equally applicable to the other shear direction v . As mentioned for mode I a cohesive response is possible only for positive normal displacement δ_n and traction t_n components. The shear mode II, instead, also allowed for negative sliding displacement δ_s and shear stress t_s components.

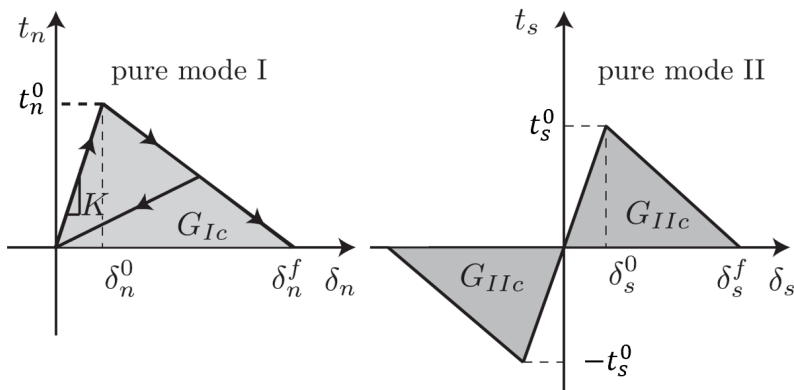


Figure 4.5: Traction-separation laws for normal mode I and the shear mode II.

For the generic mode i the cohesive stress t_i depends on the relative displacements δ_i and to the corresponding stiffness K_{ii} . This is until the cohesive strength t_i^0 is reached, then the decohesion process initiates. It is represented by a scalar damage variable D , which may be defined through a variety of relative displacement dependent functions. The linear and the exponential form are the most widely adopted, in this work a linear $D(\delta)$ softening was assumed (It can be seen in Figure 4.5 also the traction-separation law following the strength reaching results to be linear). The mathematical expression of the described traction-separation law is here reported in (4.7).

$$t_i = \begin{cases} K_{ii} \cdot \delta_i & \text{if } t_i < t_i^0 \\ (1 - D) \cdot K_{ii} \cdot \delta_i & \text{if } t_i \geq t_i^0 \end{cases} \quad (4.7)$$

The linear formulation of the damage variable, is instead reported in (4.8). It depends on the displacement at complete cohesive interaction degradation δ_i^f , the displacement at damage initiation δ_i^0 and to the actual displacement value δ_i . It results in the range between zero, in pre-damage initiation condition ($t_i \leq t_i^0$), and one when the maximum displacements δ_i^f is reached.

$$D = \frac{\delta_i^f (\delta_i - \delta_i^0)}{\delta_i (\delta_i^f - \delta_i^0)} \quad 0 \leq D \leq 1 \quad (4.8)$$

The area under the curve, denoted as G_{Ic} and G_{IIc} respectively for mode I and mode II, represents the critical strain energy per unit area. It is physically the needed energy to completely eroded the cohesive connection between two bonded unitary surfaces. If a generic mode is loaded and then unloaded prior the strength is reached, the deformation recovery occurs on the same path as the loading phase and no modification are make to the stiffness matrix. If the load produce the damage initiation, the stiffness is updated to $(1 - D) \cdot K_{ii}$ and the deformation recovery, as well as any other subsequent new elastic loading phase, occur according this new reduced stiffness. Also the strength value is updated to the value corresponding to the intersection between the softening curve and the updated elastic ramp. The amount of energy, corresponding to the area between the original and the updated stiffness values, represented the amount of energy per unit area spent to erode the cohesive contact.

The described procedure involves all the three detachment modes but in an uncoupled way. It means the effect of a simultaneous damage occurring in more than one mode is not covered. However, the experimental evidence demonstrates a simultaneous partial loading on

multiple modes can cause a early failure even if in none the initiation is the reached. To also consider this coupling effect, among the different damage mechanisms, a variety of mixing modes algorithms were proposed. They aim to combine the different loading stress and partial damage progression in an equivalent global damage criterion. In this work, the combined damage initiation was imposed according to a quadratic nominal stress criterion, whose formulation is reported in (4.9). It postulates the damage is triggered when the sum of the quadratic stress components ratios, in the principal directions, reaches the unity. The $t_{i=n,s,t}^0$ are the strength in the principal directions, while $t_{i=n,s,t}$ refer instead to the actual stresses.

$$\left(\frac{\langle t_n \rangle}{t_n^0}\right)^2 + \left(\frac{t_s}{t_s^0}\right)^2 + \left(\frac{t_t}{t_t^0}\right)^2 = 1 \quad (4.9)$$

The Macaulay bracket $\langle \rangle$ implies a pure compressive normal stress does not initiate damage ($\langle t_n \rangle = t_n$ if $t_n > 0 \cup \langle t_n \rangle = 0$ if $t_n < 0$). The equation identifies the combined stress initiation locus.

The subsequent damage evolution was set according to an energy based mode mix measure techniques, proposed by Benzeggagh-Kenane (BK). It results particularly useful in those cases when the two shear modes critical fracture energies are identical, as deemed to be the examined case. The BK criterion is here reported in (4.10). The global critical released energy per unit area G_c is obtained in function of the critical energies in the two normal G_{Ic} and shear G_{IIc} modes, the actual released energies G_I and G_{II} and the material parameter exponent $\beta = 1.45$.

$$G_c = G_{Ic} + (G_{IIc} - G_{Ic}) \cdot \left(\frac{G_{II}}{G_I + G_{II}}\right)^\beta \quad (4.10)$$

A graphical representation of the mixing mode adopted principle is reported in Figure 4.6. It can be seen the traction is reported on the vertical axis and the magnitudes of the normal and the shear separa-

tions along the two horizontal axes. The identified reference system identifies the two planes $(t; \delta_n)$ and $(t; \delta_s)$ on which the unshaded triangles represent the response under pure normal and pure shear deformation, respectively. Any intermediate planes, contain the vertical axis, represents the damage response under mixed mode conditions with different mode mixes. The dependence of the damage evolution on the mode mix is analytically defined by the BK model. Unloading subsequent to damage initiation is always assumed to be linear toward the origin of the traction-separation plane. Further reloading also occurs along the same linear softened path, as already described for pure mode softening (Figure 4.5).

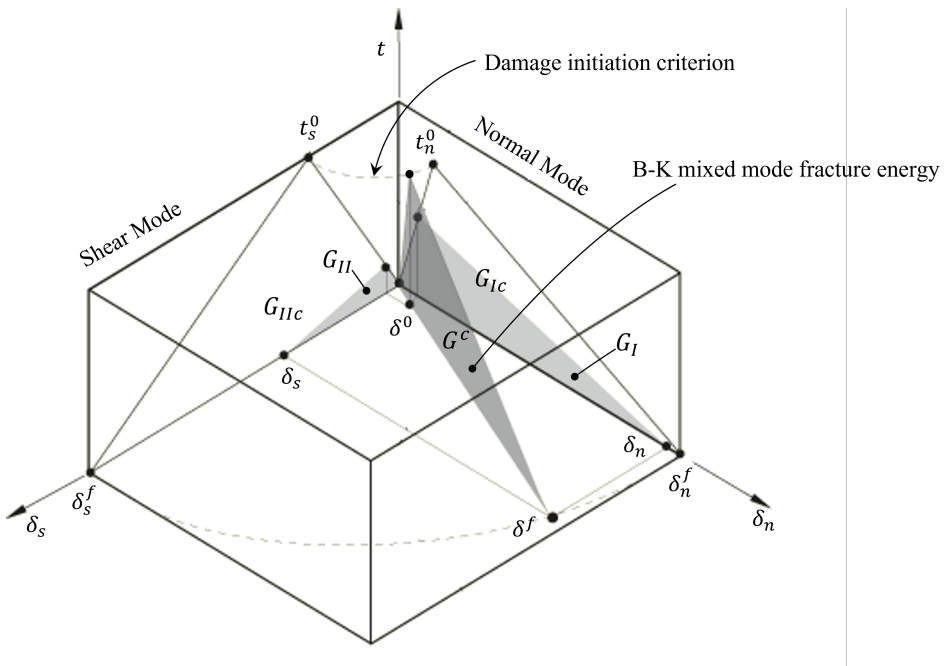


Figure 4.6: Graphical representation of cohesive response mixing mode, with stress governed initiation locus and BK energetic damage evolution highlighted.

Modelling the propagation of a pre-initiated decohesion, do not generally leads to convergence difficulties. On the other hand, the transition between the elastic pre-initiation and the damage propaga-

tion phases, when the cohesive zones is also used to model the nucleation, results to be more critical in terms of analysis convergence and stability. These problems are known to emerge from an elastic snap-back instability occurring immediately after the cohesive interface strength is reached. A simple technique to avoid these convergence issues, consists in the introduction of a viscosity parameter η into the CZM constitutive equations. It represents a relaxation time and affects the cohesive response stiffness by introducing a transient in which the viscous damage variable D_η converges to the non-viscous damage variable D . This regularization process is defined through the evolution equation reported in (4.11).

$$\dot{D}_\eta = \frac{1}{\eta} \cdot (D - D_\eta) \quad (4.11)$$

Small values of viscosity, compared to the time increment, improves the convergence of the model in softening regime. However, it must be checked the resulting traction-separation response corresponds to the imposed non-viscous cohesive law and no overestimation of traction and displacement resulted. With this purpose, a reduced viscosity parameter, if compared to the simulation time increment, aids to improve the softening regime convergence rate without compromising results.

4.3.4 Cohesive model definition

The cohesive behaviour was implemented in the computational model in form of surface-to-surface contact algorithm with small-sliding formulation enabled. The interface fibre and matrix surfaces were identically meshed and selected for the contact pairing by imposing the first as master surface. A slave nodes position adjustment depth was specified as equals to 0.01. In this range of depth the slave surface nodes can be moved by the software to avoid master surface penetration or gap, thus guaranteeing an improved contact surfaces matching. An hard-contact type pressure overclosure managing algorithm was im-

plemented. The effect of both frictionless and isotropic penalty friction models was considered during model validation. A variety of friction coefficient were tested and the influence of friction on the whole model response estimated.

The framework in which the cohesive properties identification was conducted was following described. The initial traction-separation stiffness were let software assigned, according to the framework presented in section 4.3.3, while for the damage initiation a quadratic traction criterion (eq.(4.9)) was adopted. A linear damage evolution and the BK energy based mixing mode were enabled. A viscous damage stabilization model avoided contact convergence problems, the corresponding viscosity coefficient was set as equals to $\eta = 1 \cdot 10^{-4}$. The cohesive properties were set by providing to the software the initiation strength in the three local directions $t_{i=n,s,v}$ and the respective toughness $G_{(j=I/II)c}$.

In order to fit the fibre-matrix debonding initiation as well as the resulting damage propagation, a cohesive interface properties parametrical study was conducted. The outcomes of this procedure allowed the identification of the interface properties.

Chapter 5

Computational Results

5.1 Numerical model validation

5.1.1 Boundaries condition verification

The proposed numerical model aims to reproduce the experimentally performed MCT. Despite it faithfully reproduce the testing condition, it only represents a reduced material portion enclosing the region of interest. Since the actual microcantilever proportion, compared to the whole CFRP laminate in which it is manufactured, are several orders of magnitude smaller, the specimen can be assumed as embedded in an indefinitely extended material block. Thus the effect of this condition on the numerically modelled specimen compliance must be respected. For this purpose, the matrix block dimensions (D , E , F in Figure 4.1) were defined as a result of a sensitivity analysis. The purpose of this study was to verify no boundary effect affects the model results. This implies ensuring the boundary constraints reactions do not influences the stress and strain fields close to the interface and the matrix block dimensions are properly chosen to avoid improper specimen compliance values. The analysis was performed in condition of perfectly bonded interface and linear elastic materials behavior, under the experimentally verified heaviest scenario which resulted to be the mode I loading

configuration in condition of onset debonding. Rising values of matrix block dimensions were investigated. The first tentative dimensions were assigned according to the set, referred as *S1*, here reported in Table 5.1. It confers an overall volume to the matrix of two times the micro cantilever. Then a scale factor equals to three was imposed to each of the block dimensions one at a time, in this way the effect of the material volume distribution on the specimen response can be appreciated. The illustrated block sizes are respectively reported in Table 5.1 referred as sets from *S2* till *S4*.

Table 5.1: Matrix block dimensions

Set	$D[\mu m]$	$E[\mu m]$	$F[\mu m]$
S1	3	3	4
S2	3	9	4
S3	9	3	4
S4	3	3	9
S5	5	6	5

Simulations were run by adopting the proposed dimension sets and the testing configuration of the C1 specimen group. Then the results, in terms of load vs depth curve, were compared to the related experimental results. As expected the matrix block size increase produces a specimen whole stiffness reduction.

Since this magnitude in specimen stiffness dependency to the matrix block size do not produced substantial modifications in the model compliance, the reaction force and deformation gradient extinction distance was assessed. It was verified a good trade-off, in terms of reaction force extinction distance as well as matrix compliance saturation, was reached by assigning the following reported (Table 5.1) matrix dimensions.

5.1.2 Material properties verification

Once the numerical model was refined a materials properties verification was conducted. The literature available properties, reported in Table 2.1 and extensively discussed in section 2.2, were implemented. Then a series of simulations were run to derive the pre-debonding elastic specimen response and so confirm the accuracy of the estimated properties. This results a necessary step, since the material properties available in literature were estimated on *IM7-8552* laminates manufactured with different process parameters and technologies. Further, not all the properties were directly obtained through micro and nano testing technique, but often are retrieved from macro scale tests. Some other properties like the shear moduli are instead analytically derived from the continuous mechanics relations, starting from the remaining experimentally measured properties. Particularly with regard to the fibre, which on the scale of interest is anisotropic and not strictly an homogeneous material, this led to a degree of uncertainty about the correct material properties estimation. Anyway, the properties presented in Table 2.1 represent the most reliable ones, as they are derived from laminates obtained from exactly the same materials and technology as those used for the tests proposed in this work.

The *8552* Epoxy resin was experimentally characterize by *Rueda Ruiz* through micromechanical in situ testing techniques and directly on the laminate where the micro-cantilever beams were carved [2]. Other authors in literature reported measurements showing a variation in the resin Young's modulus value in the range of $\pm 7\%$, if compared to the value adopted in the present work. Thus, the *8552* Epoxy resin was proved to show a quite repeatable response. To verify the matrix characterization accuracy, the experimental campaign, related to the C6 matrix carved specimens, was numerically reproduced in term of specimen geometry and loading condition. A simulation in purely elastic pre matrix cracking initiation was run. In Figure 5.1 the numerical

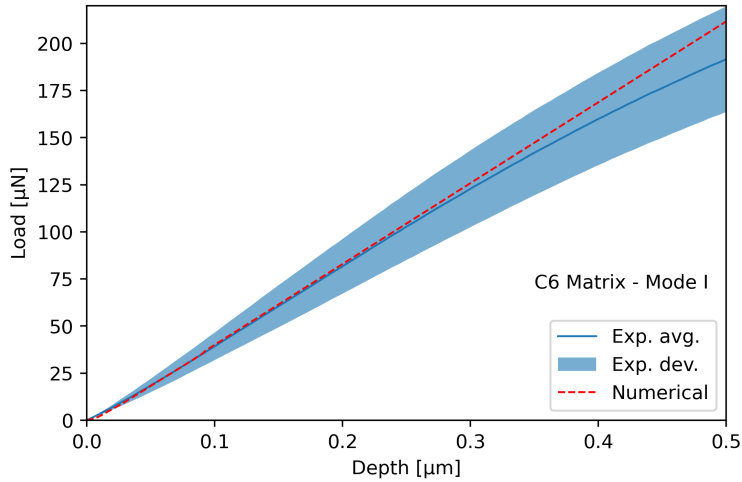


Figure 5.1: Numerical and experimental matrix carved micro-cantilever specimen response in pre cracking elastic regime.

results, in form of force over depth curve, are compared to the related experimental findings. It can be seen, the initial linear response is properly predicted by the model with an error in the specimen stiffness in the range of displacement up to $0.3\mu m$ lower than 5%. In the light of the presented results the resin properties were considered accurate enough.

As regard the literature available data about the single fibre properties, they present a greater uncertainty because of the difficulty in measuring them experimentally on the microscale. A direct fibre properties verification was impossible. While for the matrix it was possible to manufacture a dedicated specimen typology, the reduced fibre diameter did not allow for the same. Thus, the verification of the fibre adopted properties accuracy was performed on the base of the C1 specimens group, which presented both the fibre micro beam and the matrix. Numerical simulation, adapting the geometry and the load application point to the experimental reference, was run. The fibre-matrix interface was set as tied and the elastic model response computed by imposing an indenter displacements equals to $0.1\mu m$. The numerical

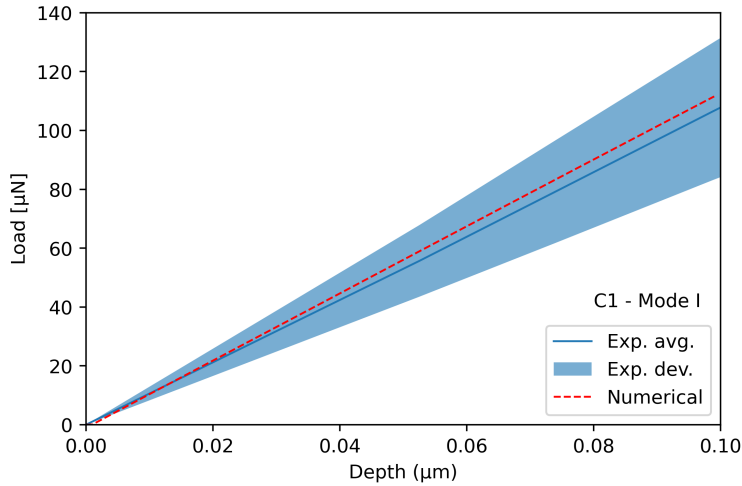


Figure 5.2: Numerical and experimental micro-cantilever specimen response under initial elastic deformation regime.

outcomes, reported in Figure 5.2, showed to slightly overestimate the rigidity. The whole system resulted to be the 8% stiffer than the average experimental specimens response. This finding is not only dependent by the fibre properties, but it is representative of the cumulative effect of also the matrix properties and the geometrical characteristics of the model respect to the real specimen. Also taking into account the scatter the experimental outcomes showed, the exposed results lead the author to retain the numerical model representative of the effective specimen experimental response. Therefore the assumed material properties correctly describe the materials behaviour.

5.1.3 Indenter positioning uncertainty effect

As exposed, the MCT execution is an delicate procedure due to the extremely reduced size of the specimens. Although performed through an AFM, the indenter positioning is also a complex procedure and not inaccuracies free. This because of the resolution obtainable in the acquisitions and the typical irregularities of the material surface. Thus, the determination of the effective load application point position was a

steps as important as it was delicate. In some testing configuration (i.e. test C3.2 reported in Figure 3.2(a)), the adoption of the sharp cube corner tip, produced a visible local fibre micro beam indentation that made the identification of the load application point position easier. In these cases an ex-post measurements through SEM was possible. This was not always the case, even among the tests adopting the cube corner tip, as visible in Figure 3.3 for the C3.4 specimen test. With regard to the tests performed with the flat tip, it was never possible to identify by SEM images any marks indicating the actual position of the punch. Consequently, for a large number of tests, the estimation of the load application point and thus the load lever arm, was performed exclusively from the topographic images acquired by AFM. Following, the specimen topographical scanning allows to assign the position of the punch by means of a pointer. An example is reported in Figure 5.3 where the C1.9 specimen AFM scan is reported. The image consists in the projection of the specimen surface on a bidimensional plane, the surface height variations are reported in form of colour scales. The fibre micro beam top surface was highlighted (dotted lines) as well as the fibre-matrix interface position and the microscope pointer were indicated.

Despite before each test, the pointer calibration was conducted to avoid misalignment between that and the effective indenter tip positioning, the process is still affected by a degree of inaccuracy in the tenths of micron order. Since the load configuration of the specimen and the representativeness of the numerical model depend on the position of the punch, it was essential to verify the effect of this uncertainty. With this purpose a series of elastic numerical simulations were performed by moving the load application point from the AFM nominal position along the micro beam x axis direction. The effect of this simulated indenter positioning error, was estimated by comparing the load over depth numerical curves with the corresponding experimentally estimated ones. Resulting the most affected by this issue, the

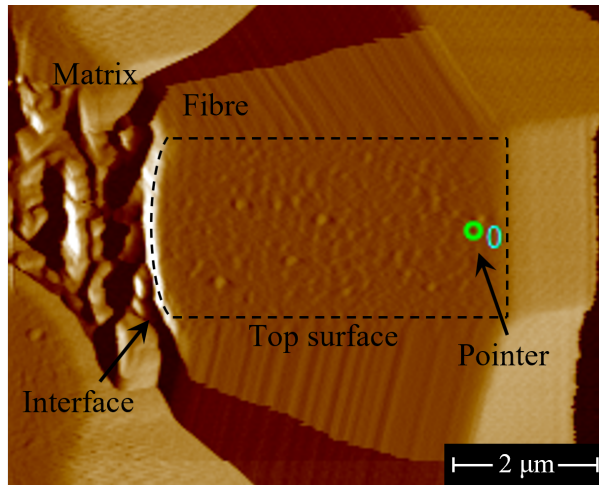


Figure 5.3: AFM topographic image of the C1.9 specimen surface, with the microscope pointer highlighted.

C4 specimens group, tested in mode II with the flat tip indenter, was adopted as experimental reference.

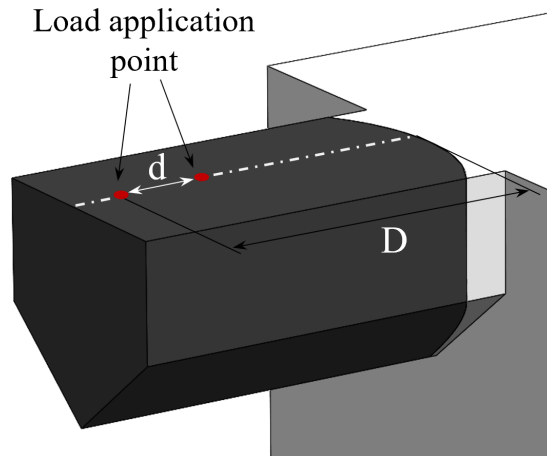


Figure 5.4: Schematic representation of the load application point moving procedure.

In Figure 5.4 a schematic representation of the followed procedure is reported. The nominal position of the load application point D representing the distance between the AFM pointer position and the

fibre-matrix interface surface is the reference configuration. The load application point is then moved from its nominal position, toward the interface, of a steps series of $0.05\mu m$.

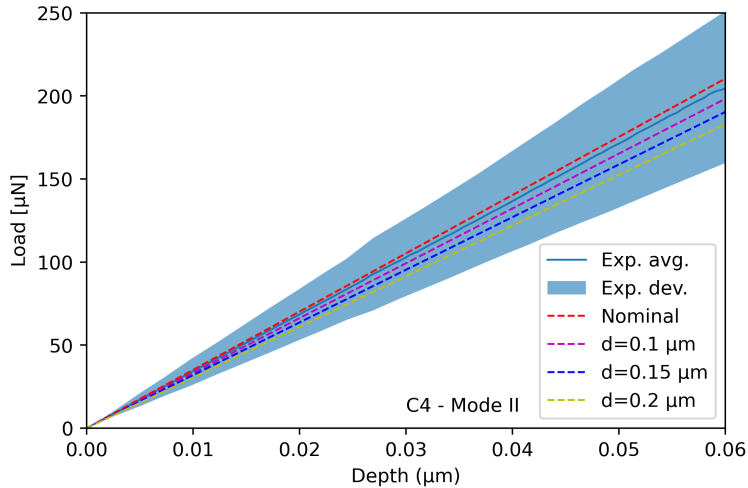


Figure 5.5: Effect of punch position error on the whole specimen response, in term of load vs depth curves for experimental C4 tests group and the numerical results related to the nominal punch position and three different positioning errors d .

The effect of punch position error on the whole specimen response is reported in Figure 5.5. The experimental C4 tests group results, in term of load vs depth curves, are compared to the numerically computed ones. The nominal punch position ($d = 0\mu m$) and three different error distance values d equals to $0.1\mu m$, $0.15\mu m$ and $0.2\mu m$ were numerically investigated. The simulation with nominal punch position produced an overestimation of the average experimental specimen stiffness equals to 2.45%. The application of the first offset value $d = 0.1\mu m$ produced a stiffness reduction of about 9.42%, while the following increments of $0.05\mu m$ corresponded in reduction of 4.75% each. All the simulated positioning errors produced results largely belonging to the experiments standard deviation. Therefore, the effect of an improper load application point positioning, was considered to not significantly affect the computational results, since it is within the

order of magnitude of the error produced by the material data and the geometrical approximation.

5.2 Interface properties identification

Once the model was proved to properly predict the elastic response of the micro cantilever specimens before debonding initiation, with reduced effect of material properties and punch position uncertainties, the cohesive model was activated and the debonding response studied. Starting from literature available interface properties, a series of simulations were run to properly fit the experimental load vs depth debonding propagation region, both under mode I and II conditions. The cohesive properties sets, following reported in Table 5.2 were investigated. The P1 set was proposed by *Rueda* [2] in his dissertation about the *IM7-8552* CFRP. The interface properties he adopted were mainly the results of an inverse identification process, in fact only the longitudinal shear strength (t_s^0) were experimentally measured through in situ push-in micromechanical testing. The remaining values were inferred according to literature guideline as following summarized. According to *Naya Montàs* [20] the transverse shear strength t_v^0 was assumed as equals to the longitudinal shear strength. The interface strength in normal direction t_n^0 was estimated as the 2/3 of the abovementioned shear strength, as recommended by *Ogihara et al.* [52]. The interface fracture energies adopted by *Rueda* were literature available values, since no suitable experimental methods were available to calibrate them. They were indirectly estimated by the convergence of a numerical model on a series of micromechanical transverse and in-plane shear tests.

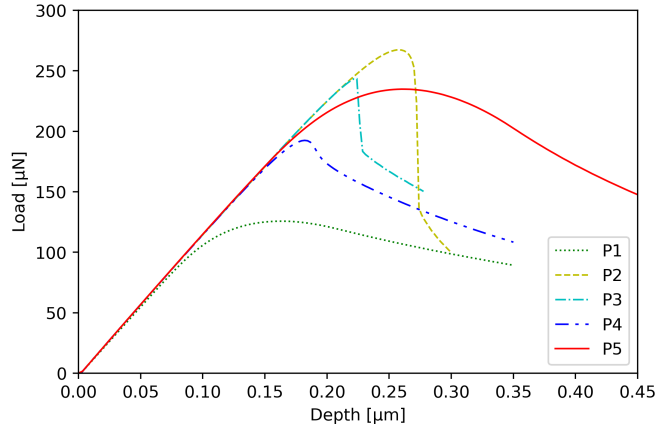
The geometrical and testing condition measured in C1 specimens mode I tested and C4 specimens mode II tested, were numerically reproduced and a series of simulations run with the purpose to appreciate the effect of the proposed interface values and fit the experiments. The

Table 5.2: Cohesive interface properties sets.

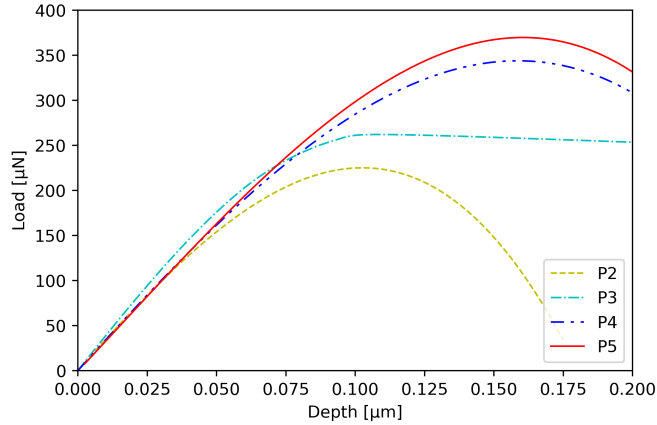
Set	t_n^0 [MPa]	$t_s^0 = t_v^0$ [MPa]	G_{Ic} [J/m ²]	$G_{IIc} = G_{IIIc}$ [J/m ²]
P1	49	74	2	6
P2	150	74	2	6
P3	120	74	2	100
P4	100	120	30	120
P5	100	135	11	100

simulation outcomes are following discussed. The mode I load vs depth curves for the interface parameters from P1 till P5 are reported in Figure 5.6(a). It can be seen the effect of cohesive strength increase produce the maximum load rising. If the elastic strain energy at damage initiation is close to the toughness, a sudden failure occurred. Otherwise a plateau region, indicating a stable debonding propagation, arises. It can be clearly appreciated by comparing the curves from P1 till P3 which have the same toughness and rising strengths. Same condition can be detected in curves from P3 till P5 which have rising toughness and quite similar strength. The greater the energy the higher the maximum load and wider the stable propagation plateau. The mode II load vs depth curves, here reported in Figure 5.6(b), interested the parameter sets from P2 till P5 since the P1 was already discarded due to the low values of maximum load reached for the mode I experiments fitting. Also in this case, bigger the strength or the toughness higher the maximum load. By comparing the results of P2 and P3 properties, it can be seen the increase in toughness at the same strength produce both an higher maximum load and a plateau region. Curves P4 and P5 have much higher strength and quite similar toughness values. The identification process converged on the P5 cohesive properties set, both for the mode I and mode II simulations. Following a comparison between the experimental results and the numerical outcomes is reported.

The comparison between C1 specimens mode I tested and the nu-



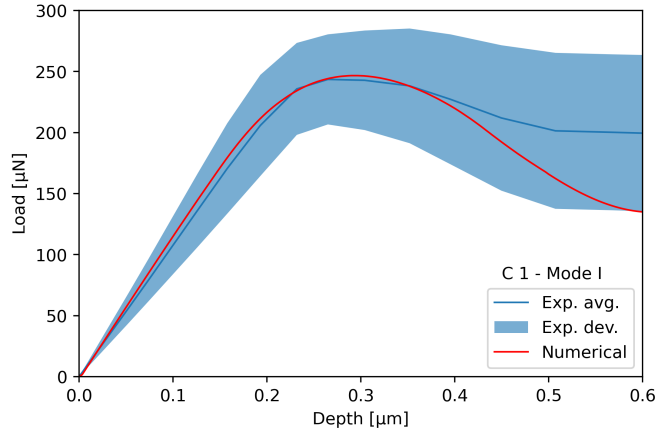
(a)



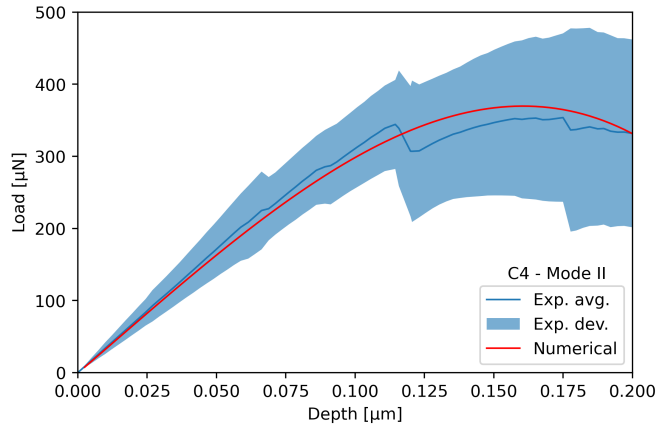
(b)

Figure 5.6: Numerical mode I load vs depth curves for interface parameters from P1 till P5 (a) and mode II for interface parameters from P2 till P5 (b)

numerical P5 curves is reported in Figure 5.7(a). It can be seen the proposed model properly reproduce the elastic pre-initiation specimen deflection, as below already discussed, as well as the initiation and first propagation phase. Then, for depth values from $0.35\mu m$ the numerical solution tends to diverge from the experimental average curve, showing a more pronounced load drop. The comparison between C4 specimens mode II tested and the numerical results showed, instead,



(a)



(b)

Figure 5.7: Numerical and experimental results comparison for C1 mode I (a) and C4 mode II (b) testing conditions.

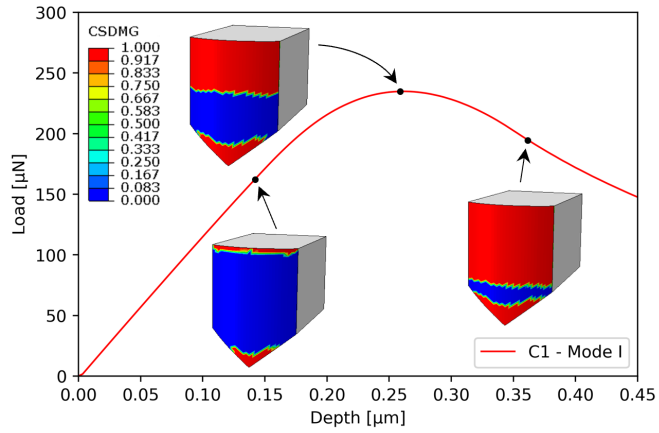
a good correlation over the entire range of depth. Despite the experiments present, in a large number of tested specimens, a sudden load drop immediately after the linear curve section, condition that cannot be predicted by the software. The reported results represents the best curve fitting. With regard to the poor matching of mode I curve in condition of extensive debonding, the author deems it could be a consequence of the matrix cracking phenomena arising under advanced propagation conditions. As described in Section 3.1, this parasite ma-

trix damage, affecting almost exclusively the mode I tests, could add up to the proper debonding propagation leading to an additional dissipated energy.

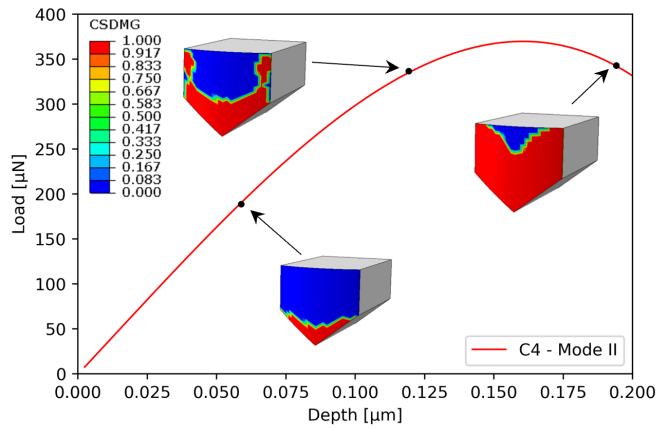
The proposed numerical model with implemented the identified cohesive parameter set (P5), reproduces the experimental results with adequate accuracy.

5.3 Damage modes contribution

A crucial aspect for the interface properties identification, was represented by the damage modes contribution balancing. The experimental methodology assumes the mode I and mode II damage behaviour can be properly isolated through the two proposed testing configurations. However no experimental evidence can confirm or disprove this assumption. Thus a numerical investigation was conducted and following presented, with the purpose to check which was the predominant damage mechanisms in each of the two test type. The debonding initiation and propagation for the mode I and mode II simulations were analyzed to highlight the differentiating characteristics. The damage variable D was thus plot on the fibre interface master surface, it was reported among the software output named as CSDMG. Its evolution in the mode I simulation load vs depth curve is reported in Figure 5.8(a), for three different debonding progression states. The initiation, meaning the quadratic stress criterion fulfillment, arises on the upper edge of the surface as well as on the lower sharp region ends. Then a progressive downward propagation of the upper front occurs, while the lower debonded region remains unaltered. The damage variable gradient on the propagation front results to be reduced, indicating once the initiation condition is reached, a sudden progression of the damage occurs. A different damage progression can be appreciated in mode II results, showed in Figure 5.8(b). The damage initiates only at the sharp bottom region of the interface and thence propagates toward the interface



(a)



(b)

Figure 5.8: Cohesive damage progression over the load vs depth curves for mode I (a) and mode II (b) numerical simulations.

top edge. Also in this case a reduced damage variable gradient can be appreciated on the front. The presented numerical propagation mechanisms looked to be consistent with the experimental evidences. The C1 specimens always presented a partial damage interesting the top region of the interface and also the matrix crack kinking suggested a downward propagation. With regard to the C4 specimens tested in mode II, the bottom region of the interface resulted to be hardly inspectable via SEM to confirm or disprove the debonding progression numerically obtained. However none of the partially damaged mode II tested specimens showed a debonded phenomenon on the upper region of the interface. This suggests the numerically obtained propagation is plausible. The damage mode contribution was evaluated for both the tested configurations. This has been achieved by considering some reference nodes on the debonding surfaces. For each of those, the dissipated energy fractions, due to the different damage modes, were computed. The study was conducted in the early phases of the numerical interface properties identification process, thus the corresponding set of cohesive properties was that referred as $P1$ in Table 5.2. However, it will be shown in the following discussion, the results are extendable to the identified $P5$ set. It should be emphasised the considered components of cohesive stress were the normal stress due to the opening displacements and the shear stress due to the cohesive slip in the direction referred as mode II in the present dissertation. No sliding phenomena were detectable, in terms of damage triggering, in the direction parallel to the beam section rotation axis. The node selected in mode II simulation was referred as S followed by the node ID number, while for the mode I selected nodes were adopted the N followed by the node ID number. For the mode II tested specimens simulation, a node on the beam symmetry plane was selected. This because in that region the effect of opening displacements is maximum while the shear is quite uniformly distributed in the section width. For the mode I simulations, were rather considered three nodes. Two were selected on

the beam symmetry plane, each pertaining to one of the two bonding fronts simultaneously occurring in this type of simulation. While the third was on the upper debonding region and placed on the side of the interface section.

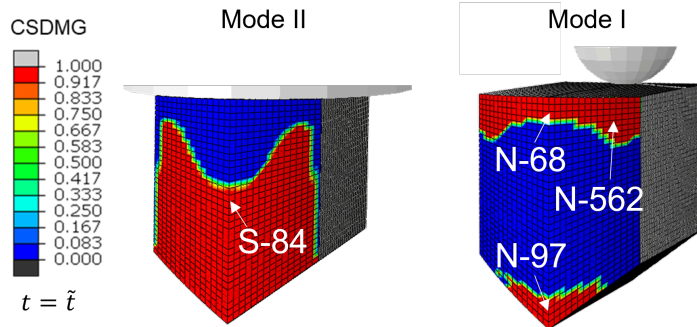
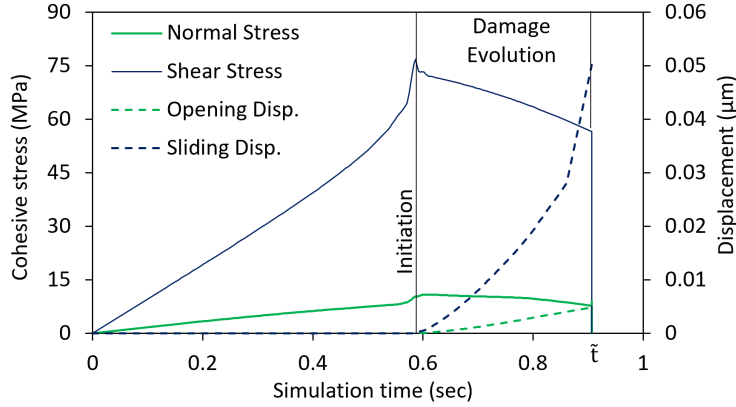
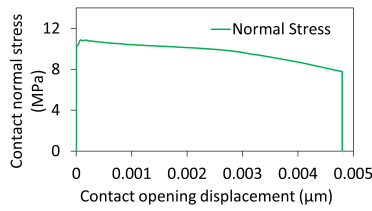


Figure 5.9: Selected control nodes for damage contribution identification in both mode I and mode II load configurations.

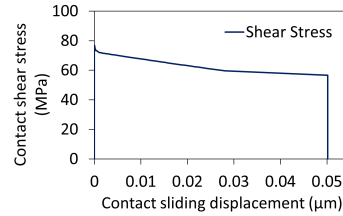
In Figure 5.9 the fibre micro-beam interface section is shown and the considered nodes are highlighted for both the loading configurations (flat indenter tip for mode II and cube-corner indenter tip for mode I). The stress outcomes, as well as the contour plots, were considered for an arbitrarily selected time of simulation, referred as \tilde{t} , in which the selected nodes achieved the complete erosion of the cohesive properties. The evolution of S-84 node cohesive stresses, together with the corresponding cohesive opening and sliding displacements, are reported over the simulation time in Figure 5.10(a). Also the damage initiation time and the damage evolution period are highlighted. For the same node the abovementioned normal and shear stresses are reported over the corresponding contact displacements in Figure 5.10(b) and Figure 5.10(c). It should be noted the area under these last two curves represents the energy release rate dissipated for each mode at the complete debonding. These values of released energy were calculated, by integrating the stress curves, and compared to the correspondent B-K mixing mode toughness (4.10). The resulting contribution values, following reported in the form of percentage contribution to total



(a)



(b)



(c)

Figure 5.10: S-84 node cohesive stresses and displacements evolution over simulation time (a) together with the normal stress (b) and shear stress (c) over the corresponding displacement.

damage in Table 5.3, shows as the damage dissipated energy is quite completely due to the shear.

Table 5.3: Contribution of opening and shear damage to the total interface damage in mode II tests for S-84 node.

Dissipated energy at damage [N/m]	
G_I	G_{II}
6%	94%

This results is also corroborated by the combination of load on the interface surface under this testing condition. In addition to the shear, it is present a bending which produce opening on the top region of the interface while in the bottom region, where the damage starts and

propagates, has an effect of closing. This condition tends to prevent the initiation of a mode I damage propagation. The same considerations presented for the mode II damage contribution analysis were enforced for the mode I. The cohesive stresses and the corresponding contact displacements were acquired and the dissipated energy for each damage mode was computed. The results in terms of single damage percentage contribution to total damage are reported in Table 5.4.

Table 5.4: Contribution of the opening and shear damage to the total interface damage in mode I tests for N-68, N-97 and N-562 nodes.

Dissipated energy at damage [N/m]			
Node	N-68	N-97	N-562
G_I	> 95%	10%	87%
G_{II}	< 5%	90%	13%

The presented results showed as the upper debonding front was characterized by a predominant damage due to the opening mode. In fact, the N-68 node, placed on the section symmetry plane, experienced a not relevant amount of shear and the N-562 node, on the side region of the section, presented a larger but still small dissipation of energy due to the shear was. This was due to the interface geometry which is not flat and thus tends to favour sliding phenomena on its side regions. However the overall behaviour of the upper debonding front experiences a dissipation energy largely dominated by the opening damage. On the other hand, the results related to the N-97 node evidenced as the damage on the lower region of the section is dominated by the shear mechanisms. This is due to a combination of the sharp geometry of the interface section in that point, which promote the stress concentration accelerating the initiation of damage, and to the bending applied on the section which produce a closure preventing the opening damage mechanisms. Despite this, the shear dominated damage, once occurred at the early stages of the load application, do not propagates during the simulations.

The presented results, describing the contribution of the damage mechanisms in the total energy dissipation, evidenced as both the mode I and mode II testing configuration resulted in a good effectiveness in producing the desired loading condition on the fibre-matrix interface independently from the investigated interface properties set.

5.4 Effect of friction

The presented numerical models were all developed by assuming a friction-less behaviour among the in contact bodies. While the influence of friction, between the indenter tip and the fibre micro-beam, do not affect the results related to the interface cohesive behaviour, the contact between the debonded surfaces at the interface could play a relevant role. Major frictional phenomena could influence the experimentally measured load over depth, thus making unrealistic the results of a friction-less approach for the numerical model. With the purpose to verify the influence of frictional sliding between the debonded interface surfaces during the tests, a series of numerical model were prepared. A first verification was conducted to check the effective response of the model to the concurrent application of cohesive interaction and friction interaction between in contact surfaces. A numerical model consisting in two rigid blocks in contact, forced to slide and under a contact closure force, was realised. The blocks consisted in a 5 by 5 *mm* discrete rigid shell geometry meshed adopting quadrilateral elements of size 0.5*mm*. a pressure $p = 1000MPa$ was applied on the upper surface of one block while the other one was constrained by suppressing all the bottom surface degrees of freedom. The upper block was then forced to slide by imposing a slip equals to 1*mm*.

On this framework three different simulations were conducted:

- **Friction** - a kinematic friction coefficient μ equals to 0.3 was assigned to the interaction.

- **Cohesive** - a cohesive contact behaviour was enabled with random cohesive properties
- **Friction + Cohesive** - both the abovementioned condition were applied together.

The results in terms of force over slip displacement are reported in Figure 5.11. It can be seen, under the described conditions, the friction model produce a constant load due to the friction which is proportional to the applied closure pressure and to the whole area in contact.

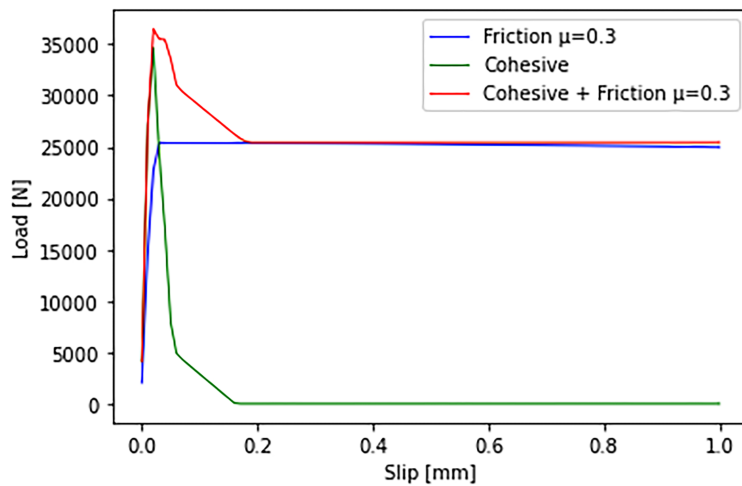


Figure 5.11: Example of load over depth curve for two block in contact with a frictional contact enable, with a cohesive contact and with both friction and cohesive enabled.

The cohesive model produces the characteristic load trend consisting in a first peak of force due to the cohesive contact strength achievement, followed by a cohesive properties erosion producing the load reduction up to the complete debonding with a null value of load. The friction plus cohesive model returns a load trend representing a combination of the abovementioned cases. The load first reaches a maximum value corresponding to the cohesive strength, then decrease to the constant value due to the frictional resistance. In this case the slope of the cohesive damage evolution has a smaller slope, since the

slip value at the complete damage have to be unchanged. To take into account the presented effect of friction on the force resulted in the micro-cantilever numerical results, a group of simulation was integrated with a kinematic frictional model and different value friction coefficient were investigated. As for the damage contribution, also this study was conducted in the early stage of the project so the adopted cohesive properties were those referred as $P1$ in Table 5.2. However the presented results are independent from the considered cohesive properties.

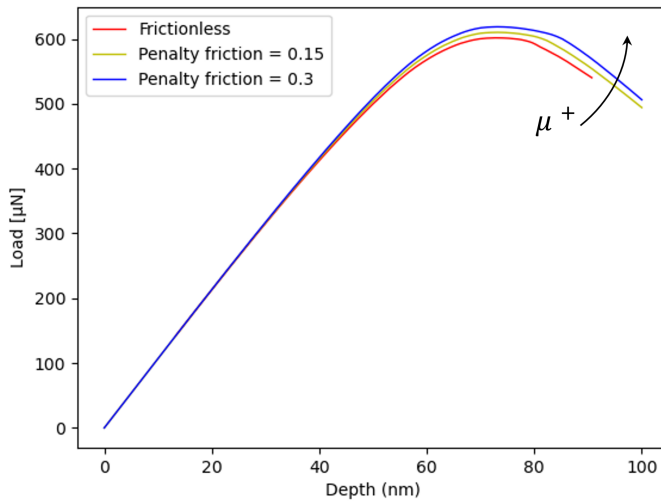


Figure 5.12

The influence of friction was estimated both for the mode I and mode II testing configuration. The mode I tests, achieved adopting the cube-cornet indenter tip, resulted to be insensitive to the friction. This is because the progression of the debonding is always combined with the opening of the surfaces, thus no contact pressure results and the occurring sliding has always a negligible friction dependency. On the other hand, the characteristic debonding mechanism related to the mode II testing condition, promotes the presence of a positive contact pressure on the debonded sliding surfaces. This condition tends to be friction sensitive, therefore simulations with friction coefficient μ equals

to 0.15 and 0.3 were run. The comparison between the friction-less model results and the investigated frictional models is here reported in Figure 5.12. It can be seen the presence of the friction produces an increase in the load magnitude. However the deviation respect to the friction-less model results is reduced to few percentage points. This is because, despite the compressive pressure between the debonded surfaces, the sliding amount is very low as well as the correspondent force. Despite a frictional effect exists in this load conditions, its effect on the whole model outcomes results to be negligible and thus the friction-less approach was considered to properly describe the investigated problem.

Chapter 6

Analytical Method

6.1 Theoretical approach

As above discussed, MCT was already adopted for interface characterization of coating layers, metallic inter-phases, inclusion and so on. Nevertheless a comprehensive mathematical description of the problem is still missing. The definition of an analytical approach would be particularly useful as it would allow a direct determination of the interface properties from the experimental results without going through long and time costly numerical simulations.

In the present chapter a theoretical description of the induced specimen deformation field are going to be presented to better understand the way this experimental methods allows the interface testing. The analytical proposed formulation will be validated on the base of the numerical results. Then an analytical methodology to estimate the interface strength and the fracture energy will be proposed and assessed on the experimental evidences. In particular, the proposed calculation method will be applied to the experimental results for test C1.3 as an example, although the method is completely general.

6.1.1 Beam deformation field

According to the classical elastic bending theory, under the effect of the applied load, the micro-beam is subjected to a constant shear force and a bending moment that linearly increase along the beam axis toward the constrained section. A micro-cantilever beam elastic scheme with shear force and bending moment distribution are reported in Figure 6.1(a). The shear stress τ and the bending moment stress σ amounts depend on the elastic and geometrical properties of the beam (i.e. cantilever length, section moment of inertia, material elastic modulus etc.). These are represented in Figure 6.1(b), where a section side view of the micro beam is reported. Within certain limits of beam geometry and deflection, the Eulero-Bernoulli and Timoshenko theories, provide a complete analytical description of the elastic problem before the interface debonding initiation.

Between them, the Timoshenko beam theory resulted to be the most accurate for the examined conditions, since also the shear deformation is considered in addition to the bending deformation. Under these assumption the cross-sectional planes rotate by losing the condition of orthogonality with respect to the beam axis. As known the shear stress distribution is variable over the cross-section (i.e. it is parabolic over a rectangular cross-section). However for the Timoshenko theory it is assumed an equivalent constant shear stress acting on the cross-section. Thus, the shear stress only depends on the section position along the beam axis. In the reference system adopted in Figure 6.1(a), the beam axis correspond to the x direction and the load P is applied in the negative y direction. The shear stress of interest is then $\tau_{xy}(x)$. This constant shear stress results from the shear force, acting on an equivalent cross-sectional area A_s , according to (6.1).

$$\tau_{xy}(x) = \frac{P_y(x)}{A_s} \quad (6.1)$$

The relation between the shear area A_s and the actual cross-section

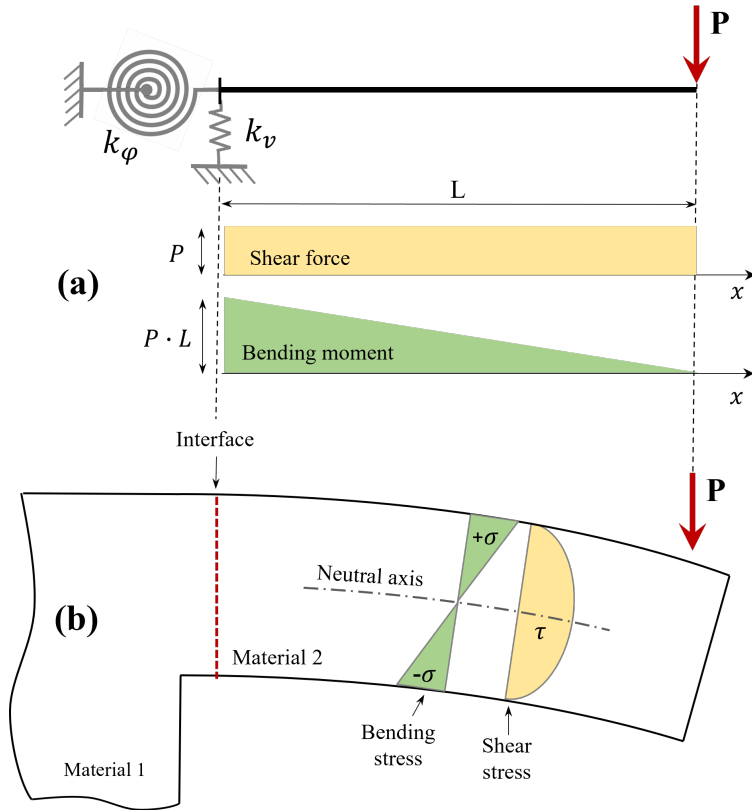


Figure 6.1: Micro-cantilever beam elastic scheme with elastic constraints (a) and a section side view of the micro beam with stress distribution and interface positioning (b)

area A is referred to the shear correction factor k_s defined in (6.2).

$$k_s = \frac{A_s}{A} \quad (6.2)$$

The analytical determination of the correction factor is not unique. However, the most adopted assumption to calculate it, is by imposing the equality between the elastic strain energy computed with the equivalent and the actual shear stress. This is a relatively easy calculation for regular section geometry, but it is difficult to determine for more complex geometries. For the sake of brevity, in Table 6.1, the fundamental relations of continuum mechanics and the boundary

conditions for the cantilever beam problem are collected.

Table 6.1: Continuum mechanics fundamental relations and cantilever beam problem boundary conditions

Relation	Equation
Constitution	$\sigma_x(x, y) = E_x \varepsilon_x(x, y); \tau_{xy}(x) = G_{xy} \gamma_{xy}(x)$
Kinematics	$\varepsilon_x(x, y) = -y \frac{d\varphi_z(x)}{dx}; \varphi_z(x) = \frac{du_y(x)}{dx} - \gamma_{xy}(x)$
Equilibrium	$\frac{dP_y(x)}{dx} = 0; \frac{dM_z(x)}{dx} = -P_y(x)$
Boundaries	$x = 0 \rightarrow \begin{cases} \varphi = 0 \\ u = 0 \end{cases}$

In the proposed bidimensional schematization of the cantilever beam problem, the stress fields σ_x and τ_{xy} can be related to the corresponding strains ε_x and γ_{xy} through the constitution equations involving the Young's modulus E_x and the transverse modulus G_{xy} . This last is related to the Young's modulus and to the Poisson's ratio as in (6.3), for a transversely isotropic material.

$$G_{xy} = \frac{E_{xy}}{2(1 + \nu_{xy})} \quad (6.3)$$

The kinematics relation link the strain fields to the displacement u_x and rotation φ_z through a differential way. While the equilibrium differential equations, specialized for the considered load configuration, summarise the relation between bending moment M_z and shear load P_y and the shear load continuity over the beam length. Lastly the boundaries conditions formalise the constraint full fixity.

$$M_z(x) = P_y \cdot x = E_x I_z \frac{d\varphi_z(x)}{dx} \quad (6.4a)$$

$$P_y(x) = k_s A G_{xy} \left(\varphi_z - \frac{du_y(x)}{dx} \right) \quad (6.4b)$$

According to the presented relations, M_z and P_y are reported, in the function of the material properties and cross section geometry, as a function of u_x and φ_z in equations (6.4a) and (6.4b). Integrating by parts the last expressions and collecting the terms, u_x and φ_z can be write as follow (6.5a), (6.5b).

$$\varphi_z(x) = \frac{x \cdot P_y}{E_x I_z} \left(\frac{x}{2} - L \right) \quad (6.5a)$$

$$u_y(x) = \frac{x \cdot P_y}{k_s A G_{xy}} + \frac{x^3 \cdot P_y}{2 E_x I_z} \left(L - \frac{x}{3} \right) \quad (6.5b)$$

The found analytical expressions allow to completely define the stress and strain fields in a cantilever beam fully fixed at one end section and loaded with a punctual force P_y on the other end. However, the mentioned formulations was developed for homogeneous and isotropic materials, conditions not always verified in the practical cases. Thus its applicability in the proposed case must be verified.

Further complications arise when an interface surface is also present within the specimen. This represents a discontinuity often connecting two different materials. As reported in Figure 6.1(b), in those cases where the purpose is to test an interface, the specimen is manufactured so that it is located close to the beam most stressed section. This is to induce a pure interfacial failure avoiding further crack initiation within the material. Under the described conditions, the interface failure is promoted by a combination of opening mode (Mode I), due to the tensile stress σ normal to the interface plane, and a sliding

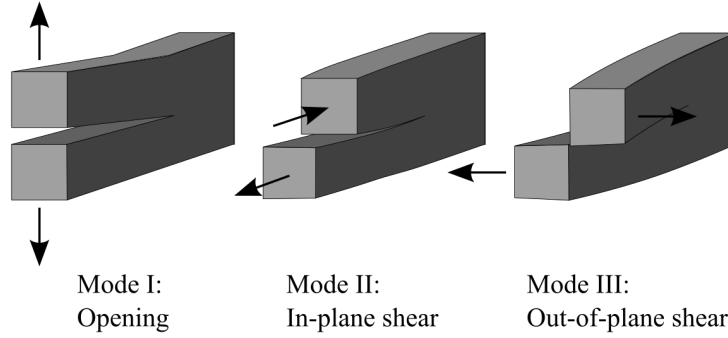


Figure 6.2: The three different modes of interface failure, discerned according to the direction of the applied load with respect to the interface plane.

mode (Mode II), due to the shear stress τ , acting on the interface plane. The interface failure modes are here reported in Figure 6.2, discerned according to the direction of the acting load with respect to the interface plane. As mentioned, the concurrence of shear and bending stress induces a combination of mode I and II at the interface. The isolating of a pure debonding mode can be attempted by properly selecting the geometrical properties of the beam section and the load application mode and position.

6.1.2 Analytical solution adaptability

It should be also considered the constraint conditions are different from the ideal full fixity, so that their schematization resulted to be particularly complex. Since the microcantilever specimen is manufactured by milling the beam in a continuum material block, the specimen whole compliance also depends on the material surrounding the beam. This can be schematized by considering the beam elastically constrained. Thus the linear and rotational springs in Figure 6.1(a), respectively having stiffness k_φ and k_v , represent the effect of material block compliance, regardless of whether the beam and block material is the same.

$$\varphi_z(x) = \frac{x \cdot P_y}{E_x I_z} \left(\frac{x}{2} - L \right) + \frac{P_y L}{k_\varphi} \quad (6.6a)$$

$$u_y(x) = \frac{x \cdot P_y}{k_s A G_{xy}} + \frac{x^3 \cdot P_y}{2 E_x I_z} \left(L - \frac{x}{3} \right) + \frac{P_y}{k_v} \quad (6.6b)$$

Since the applicability of the superposition principle, the suggested constraint modification can be integrated to (6.5a) and (6.5b), in the form of additional terms reported in red color in (6.6a), (6.6b). This interpretation of the constraining condition is extremely simplifying, resulting in a potential large approximation of the specimen elastic response. However, since a more accurate analytical solution for the problem is still missing, the above proposed formulation can provide an estimation of the whole specimen elastic response in condition of perfectly bonded interface. Under these assumptions, the proposed model was verified on the base of the numerical results as following itemized:

- the effectiveness of the timoshenko beam theory, when applied to the geometrical and material anisotropy conditions, proper of the proposed MCT, was numerically validated.
- the proposed adaptation of the theory, to the MCT constraining conditions, was then calibrated on the matrix block stiffness. An expression for the entire micro-cantilever specimen compliance as a function of the applied load was derived. Such an expression was validated on the experimental specimen stiffness in pre-debonding initiation conditions.
- a relation between the whole specimen compliance and the debonding front advance was numerically identified through a series of simulations. This allowed to derive the debonding front advance from the experimental specimen compliance drops, obtained through the incremental repetition in the load application.

- finally an analytical estimation of the mode I critical energy release rate was performed and compared to that one retrieved from the numerical regression procedure.

The proposed procedures, while still partly adopting numerical procedure, results to be much more efficient in terms of time and computational costs if compared to the cohesive modelling approach. The needed simulations are those to retrieve the relation between the whole specimen compliance and the debonding front advance, which all together take a tenth of the time of a single simulation with the cohesive model implemented.

6.2 Theory applicability

6.2.1 Timoshenko Beam consistency

The timoshenko theory consistency respect to the considered problem, was verified by comparing the numerical and the analytical beam deflection curves. With this purpose, the fiber beam was numerically modelled as a stand alone entity, rigidly constrained at its end section and vertically loaded at the other end. Then the bending stress distribution was evaluated over a beam section far from both the constrained and the loaded sections. The neutral axis was so identified and the vertical displacements, oriented according to y direction and referred as U_2 , were plot over the nodes on the line obtained from the intersection between the $y - z$ symmetry plane and the section neutral axis plane. In Figure 6.3(a) a schematization of the deflection line identification procedure is reported, while in Figure 6.3(b) a contour plot of the U_2 displacements over the fibre beam is showed.

The displacements along the beam axis were also analytically computed, known the fibre properties and the beam geometry. The section moment of inertia was calculated as well as the neutral axis position

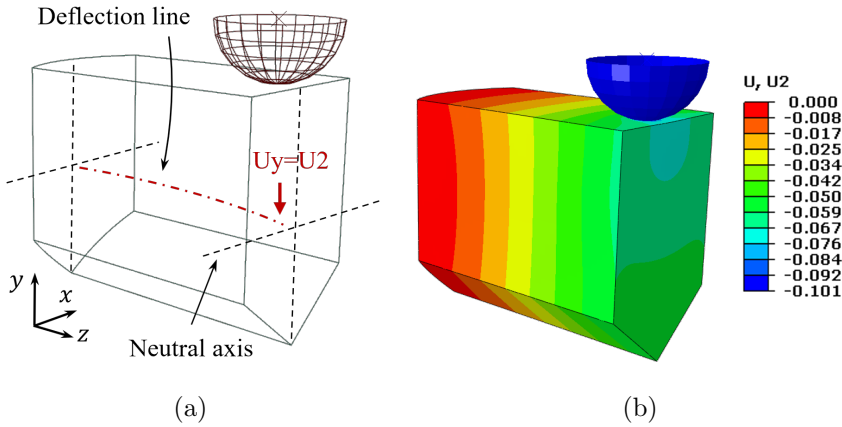


Figure 6.3: Schematization of the numerical deflection line identification procedure (a) and $U2[\mu m]$ displacements contour plot (b)

under the hypothesis of pure bending loading condition. Both the numerical model and the analytical procedure were calibrated, in terms of geometry, on the experimental tests. In the following chapter, the results of the described procedure will be presented as related to the C1.3 mode I tested specimen.

6.2.2 Adapted solution calibration

To analytically define the micro-cantilever specimen deflection curve, under the testing conditions, by mean taking into account also the effect of the matrix compliance, the elastic constraint stiffnesses k_φ (6.6a) and k_v (6.6b), were calibrated on the matrix block elastic response. A numerical simulation involving the entire micro-cantilever specimen allowed to measure the displacement Uy of the interface section centre of gravity as well as the average rotation of that section. Known the applied load and the geometrical dimensions, k_φ and k_v can be estimated, allowing to solve equations (6.6a) and (6.6b). Since the contact surface is not flat, the displacement field on its intersection with the deformation axis surface result not constant. Thus the displacement v was estimated as the average of the aforementioned intersection nodes

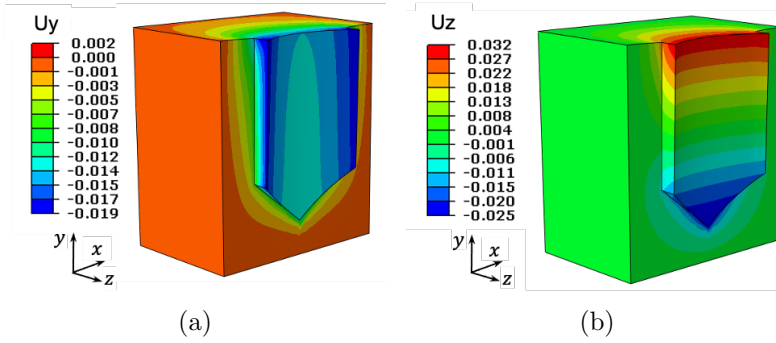


Figure 6.4: Interface section displacement fields Uy (a) and Uz (b) reported in $[\mu m]$.

displacement values. For the φ defining, the axial z displacements along the section height, were linearly interpolated and the slope of the fitting line was taken as a reference. The contour plots representing the displacements along the y axis and the axial z displacements are respectively reported in Figure 6.4(a) and Figure 6.4(b). It can be seen the Uy displacements have a reduced change over the interface front and the axial Uz displacements have an almost perfectly linear distribution along the section height. The load P , together with the computed values of v and φ are following reported in Table 6.2

Table 6.2: Applied load P and resulting displacement

$P[\mu N]$	$v[\mu m]$	$\varphi[rad]$
133	$1.90e - 2$	$1.38e - 2$

Known the corresponding applied load values, the lumped stiffnesses k_φ and k_v were then calculated from the last terms in red of equations (6.6a) and (6.6b). The resulting analytical relation between the applied load and the beam deflection was compared to the numerically computed specimen deflection. The results will be presented in the following chapter 7.1.

6.3 Interface strength calculation

Once the specimens deformation regime was proved to be equivalent to a bending beam, a regression to the interface strength properties can be made. Known the geometrical and inertial properties of the beam cross-section, the bending stress at the sections upper surface can be calculated according to the continuum mechanics equation reported in (6.7). The equation was specialized for the reference system adopted in Figure 6.3 and for the interface section of interests. I_z is the cross-section inertial moment around the baricentric z axis, y_{max} is the distance of the upper beam surface from the neutral axis and L is the distance between the interface beam section and the load application point. Finally \bar{P} represents the load values corresponding to the debonding onset. Thus, the resulting stress value $\bar{\sigma}_x$ can be intended as the interface strength.

$$\bar{\sigma}_x = \frac{\bar{M}_z}{I_z} \cdot y_{max} = \frac{\bar{P} \cdot L}{I_z} \cdot y_{max} \quad (6.7)$$

All the mentioned properties were already defined, less than the values of \bar{P} , which needed to be extrapolated from the experimental load vs depth curves. To enable this, an identification criterion has been defined. It was chosen to regress to this characteristic load value by considering the entire specimen stiffness trend. As known, in the pre-debonding initiation it results to be a linear function of the applied depth, while the damage onset and propagation produces a stiffness modification. Thus, the derivative of the load with respect to the depth, which punctually represents the specimen stiffness, was computed and reported as a function of the experimental applied depth. The first stiffness slope change was found and the corresponding experimental depth univocally identifies the desired load value \bar{P} . The computed strength value was compared to the numerically calculated one and the robustness of the analytical proposed approach discussed in the following chapter.

6.4 Interface toughness tracing

An analytical procedure, to trace back the interface properties from the experimental results, was proposed also for the toughness identification. It was permitted by the way a group of tests was performed. A process of partial unloading was, in fact, cyclically operated during the tests execution. As described in Chapter 2 each loading ramp was characterized by a load vs depth slope, representing the specimen stiffness at that stage. It can be observed the slopes result to be characterized by two different phases. In the first phase they are quasi-constant among the loading steps, while in the second phase a progressive slopes decrease can be observed. In the absence of other dissipation phenomena (i.e. plastic deformation, indenter tip sliding, indentation etc.), the debonding onset and propagation are the reasons of this progressive reduction in the specimen stiffness. Thus, the tracing back of the loading slopes decrease, can be helpful to focus the debonding progression stage. The described approach represents a widely adopted practice for the toughness estimation both in fracture and adhesive joint mechanics. As following briefly described, it is based on the Griffith energetic principles and it allows to compute the energy release rate known the testing load conditions, the geometrical configuration and the crack advancement. However, to the best of the author's knowledge, no examples of the application of this procedure to FRP materials are available in the literature. Further, the scientific publications and standards referring to this approach are in fact mostly focused on metallic or ceramic materials, both composite and non-composite, generally isotropic or very weakly orthotropic.

6.4.1 Griffith theory

In the field of fracture mechanics the energetic Griffith principle allows to describe the propagation of a fracture in a brittle material. It consists in an energy balance between the potential energy and the work

required to generate and propagate a crack. It refers to the generic configuration, here reported in Figure 6.5, consisting of a plane plate subjected to a constant traction load in which a crack of length $2a$ is made. The crack tips are considered as infinitely sharp. The plate

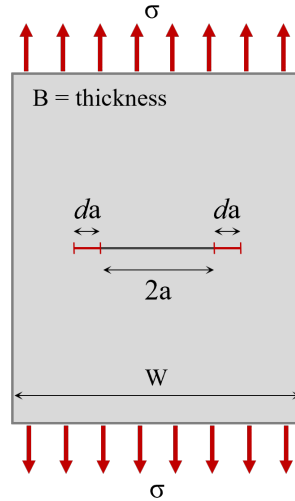


Figure 6.5: Through crack subjected to a propagation.

thickness is referred as B , while σ is the remote stress. Under these assumptions, a crack propagation of an infinitesimal amount da , produces a modification $d\Sigma$ in the total elastic energy, that can be estimated as following reported in (6.8).

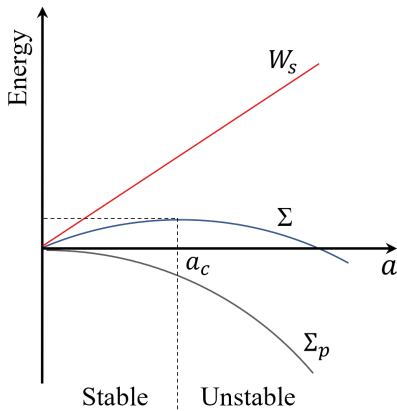
$$\frac{d\Sigma}{dA} = \frac{d\Sigma_p}{dA} + \frac{dW_s}{dA} \quad (6.8)$$

This plate energetic balance, between two stages of crack propagation, depends on the amount of potential energy Σ_p and on the work required to generate new fracture surfaces W_s at the considered stages. The derivative is weighted on the generated crack area $dA = B \cdot da$. Under equilibrium conditions the total elastic energy is constant and so the two terms results equals and opposite in sign (6.9). This means the work done to generate the fracture extension da is carried at the cost

of the potential energy.

$$-\frac{d\Sigma_p}{dA} = \frac{dW_s}{dA} \quad (6.9)$$

For the considered geometrical configuration both Σ_p and W_s can be easily computed. In (6.10a) the potential energy, given by the Inglis solution, is expressed as the difference between the potential energy of the un-cracked plate and the change in elastic strain energy due to the crack. This last terms is expressed as a function of the remote stress σ , the plate thickness B , the material Young's modulus E and the crack length a . With regard to the work to generate the surface fracture, it can be write as the product between the total fracture surface and the surface energy γ_s (6.10b). In Figure 6.6 the energy variation over the crack length is schematically reported. It can be observed W_s linearly depends from the length a , while Σ_p is a quadratic power of it. According to the equation (6.10c), the resulting elastic energy Σ trend shows a quadratic trend too.



$$\Sigma_p = \Sigma_{p,0} - \frac{\pi\sigma^2 a^2 B}{E} \quad (6.10a)$$

$$W_s = \gamma_s \cdot 4aB \quad (6.10b)$$

$$\Sigma = \Sigma_p + W_s \quad (6.10c)$$

Figure 6.6: Energy variation with corresponding crack length

A distinctive point, on the Σ curve is represented by the a_c value, computed as the crack length underlying an energy slope null value. For $a < a_c$ the crack propagation is stable, since the potential energy released is lower than the work needed for the crack propagation. Thus an external work have to be provided. On the contrary, for $a \geq a_c$ the potential energy exceeds the work needed, so producing

the unstable propagation of the crack.

6.4.2 Energy release rate definition

The Griffith energy balance was further improved by Irwin, through the definition of the energy release rate G notion. He identified in the equivalent terms of equation (6.9) an expression for the energetic configuration change, so that $G = -d\Sigma_p/dA$. The crack extension occurs when the applied energy release rate exceeds the material resistance to crack extension, represented by the energy release rate critical value G_c . If results $G > G_c$ the crack propagation is energetically favorable. Some materials show a constant G_c value, while for some other it results to be variable property. It can be reported as a function of the crack length a and the resulting plot takes the name of resistance (R) curve. To univocally identify a value of critical energy release rate, also in those cases of not constant G_c , a standard procedure was developed and reported in the international standards such as the ASTM E1820 [53] for a variety of brittle materials (mainly metals). For a specific load configuration, also G can be reported as a function of a and overlaid to the R-curve to verify if the considered load produce and unstable propagation.

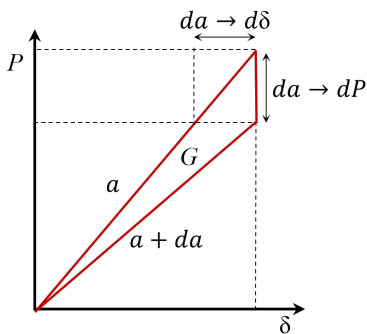


Figure 6.7: Load-displacement curves for a crack increment da .

The energy release rate can be easily computed from the experimental load over depth curves for a large variety of testing configurations.

$$G = \frac{P^2}{2B} \cdot \frac{dC}{da} \quad (6.11)$$

In fact, a crack length increase, from an amount a to $a + da$, produces a reduction in the specimen response stiffness, as shown in Figure 6.7. The area between the load ramp for the crack ex-

tension a and $a + da$ represents the released energy for the da length increase. This can be calculated for both load controlled and displacement controlled tests through the equation (6.11), where C is the experimental compliance computed as the inverse of the load P over depth δ curve slope. The exposed method assumes the load and the displacement as well as the crack length can be experimentally measured.

6.4.3 Energy release rate calculation

In the present work the energy release rate was computed not only on the basis of experimental evidence, but also through numerical simulations. This was because the crack length was not experimentally measurable over the tests. The partial unloading, interesting a group of experiments, was assumed as reference to compute the load over depth curve stiffness drop, similarly to the case presented in 6.4.2. In Figure 6.8 a schematization of the stiffness identification with the debonding progression is reported. According to the ASTM E1820 standard the pre-initiation ramps were excluded and the maximum load reaching cycle was assumed to compute the first stiffness K_0 to which corresponds the debonding length denoted as a_0 . So that, two generic subsequent load cycles present stiffnesses respectively equals to K_{i-1} and K_i and corresponding debonding length a_{i-1} and a_i . As mentioned the debonding length values, corresponding to the calculated stiffnesses, were not experimentally measurable. Thus a numerical identification process was conducted to extrapolate a mathematical law expressing $a(K)$ or its inverse, the compliance $C(a) = 1/K(a)$. With this purpose a numerical model reproducing the single experiment was prepared. As already described in section 5.1.1, a perfectly bonded fibre to matrix interface was considered by imposing a contact interaction constraint. But, in this case, to simulate an advanced debonding state, the constraint interested a reduced region of the interface sur-

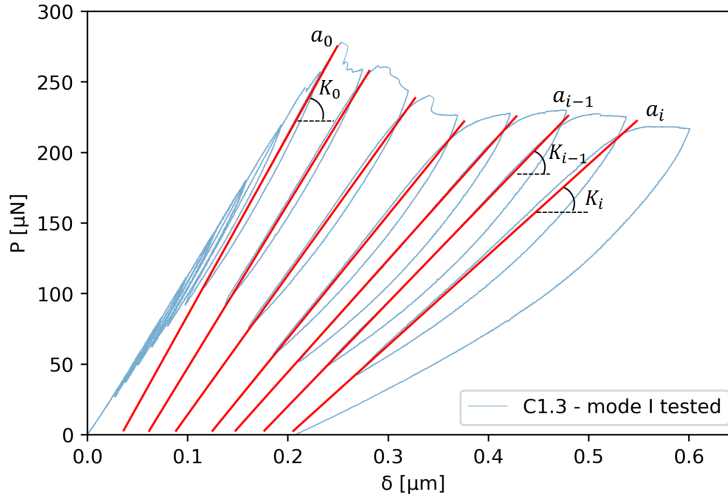


Figure 6.8: Schematization of the experimental stiffness identification with the debonding cyclic progression.

face, while the remaining was leave untied. The height of this untied region is actually the debonding length a . A schematization of the adopted model is here reported in Figure 6.9(a). The simulation were conducted by imposing the same loading condition adopted for the experiments. A verification between the numerical and the experimental stiffnesses was also conducted by comparing the pre-debonding initiation experimental outcomes with the numerical model results obtained adopting a perfectly bonded entire interface ($a = 0$). The experimental stiffness was computed as the average of the stiffnesses related to the loading ramps preceding that reached the maximum load. In Figure 6.9(b) a detail of the debonded region opening effect under load application is reported. To trace the specimen stiffness as a function of the debonding length, a series of untied surface height were imposed and the corresponding numerical output, in terms of indenter reaction force over depth, handled to compute the stiffness. The considered values of debonding length are the following:

$$a = \{0; 0.25; 0.5; 0.6; 0.8; 1; 1.2; 1.3; 1.5\}[\mu m]$$

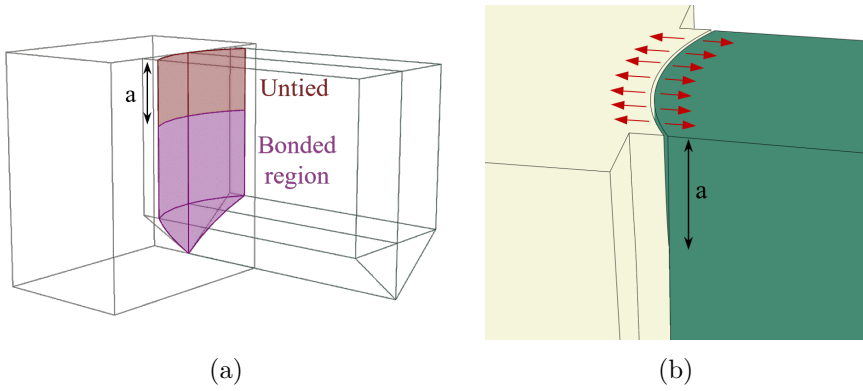


Figure 6.9: Schematization of the model with bonded and untied interface region highlighted (a) and detail of the debonded region opening effect under load application (b)

The simulations were performed by considering the same maximum indenter displacement as equals to $0.1\mu m$. The identified mathematical law was adopted to calculate the debonding length corresponding to the experimental measured stiffnesses. Then the equation (6.11) was solved in the discrete form reported as equation (6.12).

$$G_i = \frac{P_i^2}{2B} \cdot \frac{C_i - C_{i-1}}{a_i - a_{i-1}} \quad (6.12)$$

The obtained energy release rates and the corresponding debonding lengths, can be plot and interpolated with a polynomial function which is the R-curve. The definition of the critical value for the energy release rate was found according to the procedure reported in ASTM E1820 standard. The calculated value of toughness was compared to that numerically obtained and robustness of both the calculation methodologies were discussed in the following analytical results chapter.

Chapter 7

Analytical Results

7.1 Elastic solution validation

First the timoshenko theory consistency was verified for the case considered in 6.2.1. In Figure 7.1 the deflection (Uy) of the micro-beam made of fibre was reported over its axis (z) for both the numerical model and the analytical timoshenko formulation.

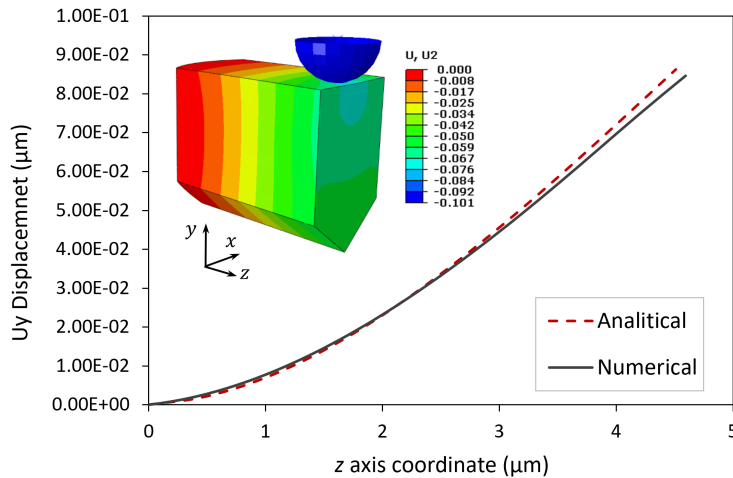


Figure 7.1: Analytical and numerical fibre micro-beam deflection curve comparison.

A very good agreement between the curves resulted from the com-

parison. This confirms, under the considered geometrical beam proportions, the timoshenko theory still provide a good description of the beam deflection, despite both the hypothesises of material isotropic behaviour and slenderness are not strictly respected.

Table 7.1: Analytical adapted solution lumped stiffnesses.

$k_v[\mu N/\mu m]$	$k_\varphi[\mu N \cdot \mu m]$
6990.63	385.17

In the second instance, the interface section y axis displacement v and rotation φ (Table 6.2) were adopted to calculate the lumped stiffnesses k_v and k_φ . These values, following reported in Table 7.1, allowed to completely solve the analytical adapted solution proposed for the MCT deflection line determination. A comparison between the numerical deflection of the specimen and the analytical results, is reported in Figure 7.2. The initial displacement value and curve slope, actually represent the estimation of v and φ . The proposed modification for the timoshenko solution prove a good specimen deflection prediction capability.

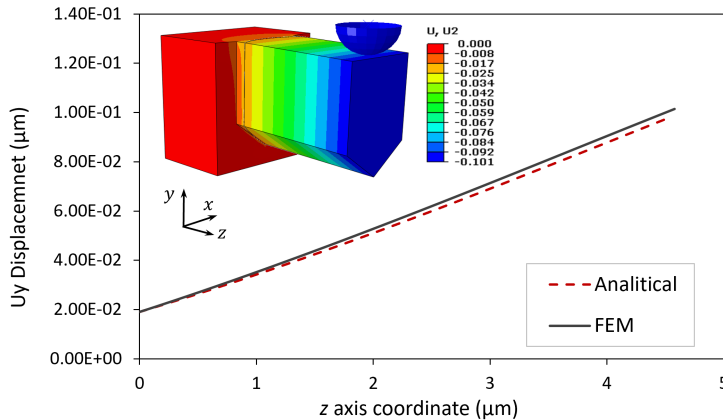


Figure 7.2: Analytical and numerical micro-cantilever specimen deflection curve comparison.

7.2 Interface strength determination

The interface strength determination was made by considering the average load over depth curve for the mode I testing experiments. As discussed in section 6.3, the derivative of the load was calculated. In Figure 7.3 its value over the depth is reported together with the average load P . It can be seen, for an initial amplitude of depth the load derivative results to be quasi-constant, then a rapid drop occurs.

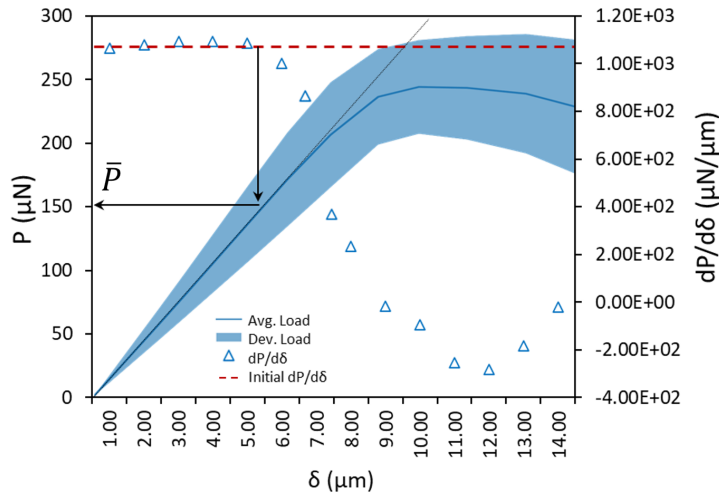


Figure 7.3: Average load vs depth curve for the mode I tested specimens , together with its discrete derivative and the mean value of the initial range where this last is constant.

The average value of the initial constant range of values was computed and reported in Figure 7.3 through the red dotted line. The depth value, corresponding to the first drop of the derivative value, was adopted to define the load value $\bar{P} = 153.4[\mu\text{N}]$ corresponding to the debonding onset. Equation (6.7) was then solved and the mode I interface strength value following reported:

$$\bar{\sigma}_x = 102.64[\text{MPa}]$$

The analytically calculated strength value will be compared to that

numerically traced in the following concluding chapter, where also the consistency between the two approaches will be extensively discussed.

7.3 Toughness calculation

7.3.1 Compliance vs debonded length relation

The toughness tracing process started from the identification of the compliance in function of the debonding length. A series of numerical simulations, with applied the debonding length specified in 6.4.3, were performed. The resulting specimen compliance-debonded length pairs were interpolated with a polynomial function.

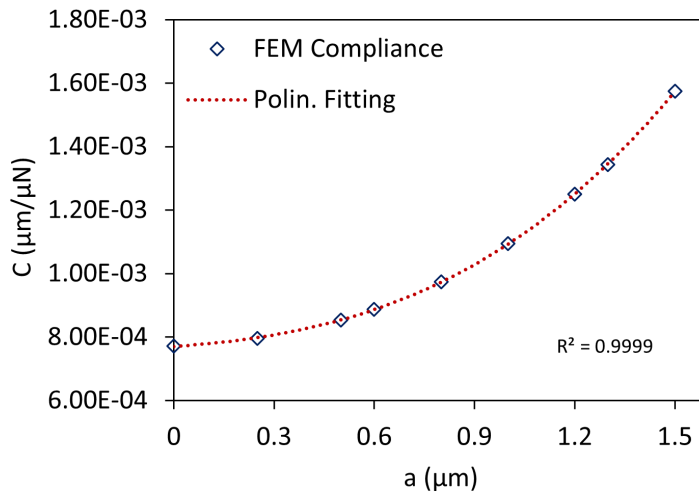


Figure 7.4: Numerically calculated compliance vs debonding length data and cubic polynomial fitting curve, together with the R-squared value.

The *MatLab non-linear fitting tool* was adopted to perform the interpolation. The data fitting quality was estimated through the coefficient of determination R-squared \mathbf{R}^2 . This statistical marker indicates the percentage of the variance in the dependent data set that the independent data set explain collectively. In a regression model it evaluates the scatter of the data points around the fitted regression curve. It is

in the range from zero to one, where the null value means the fitted curve and the data are not correlated, while the unit value means the fitting explains all the data variation around their mean. In the case of interest, the best fitting resulted from the adoption of a third order complete polynomial, here reported in general form in equation (7.1).

$$C(a) = A_1 \cdot a^3 + A_2 \cdot a^2 + A_3 \cdot a + C(a = 0) \quad (7.1)$$

In Figure 7.4 both the numerically calculated compliance vs debonding length data and the cubic polynomial fitting are reported, together with the related R-squared value. As expected, it can be seen the compliance of the specimen raises with the debonding progression. The fitting calculation provided the coefficients A_i reported in Table 7.2, they corresponds to a $\mathbf{R}^2 = 0.9999$.

Table 7.2: Compliance vs debonding length polynomial fitting coefficients.

A_1	A_2	A_3	$C(a = 0)$
$1.1668e - 04$	$1.3496e - 04$	$7.0310e - 5$	$7.7061e - 4$

It represents a very good correlation level between the numerically calculated compliance-debonded length pairs and the polynomial fitting model. It should be noticed the the coefficient multiplying the debonding length raised to the zero exponent (a^0), representing the intersection of the curve with the compliance axis, has a physical meaning. It is the value of the compliance for a completely bonded interface $C(a = 0)$, thus it should not be calculated by the fitting process.

7.3.2 Resistance curve definition

The resistance curve was estimated starting from the identification of the load vs depth curve cycles stiffnesses. A linear interpolation of the load ramps provided the K_i values, a total of $i = 14$ cycles were

performed in the considered C1.3 experiments. The related compliance values were then obtained and plotted over the load cycles repetition in Figure 7.5. It can be seen a first group of values, up to the the eighth cycle, produced a quite constant response in terms of compliance.

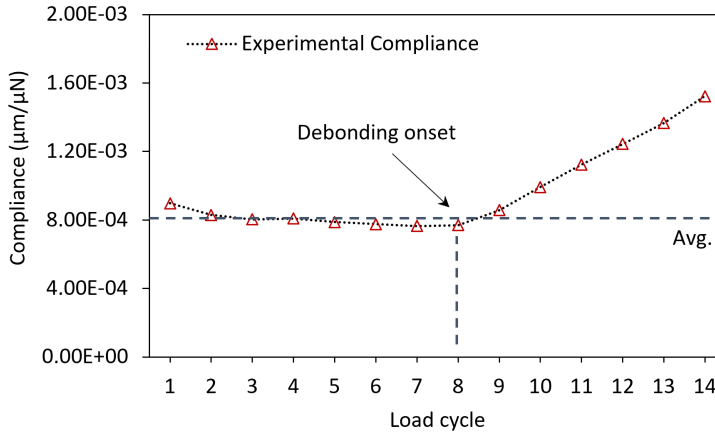


Figure 7.5: Experimental specimen compliance over the load cycles, together with the average compliance value

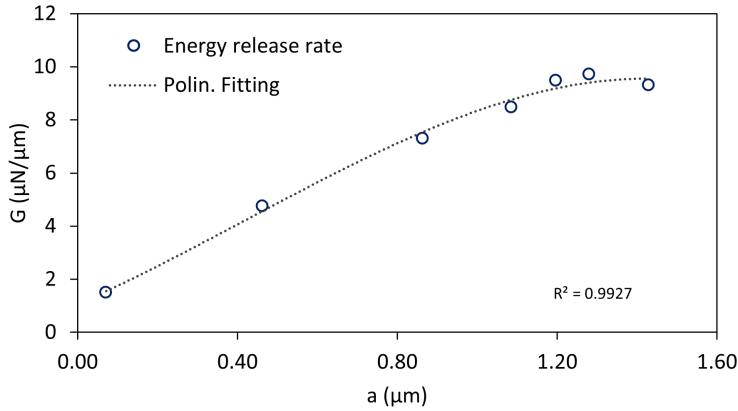
The maximum load recorded for these load cycles was always increasing, until the eighth cycle produced the highest absolute load value in the test. In the subsequent cycles a progressive increase in the compliance value is visible and the corresponding maximum load was found to be descending. This erosion of the specimen stiffness properties, can be ascribable to the interface debonding phenomenon. Thus the last value presenting a quasi constant compliance and the absolute maximum load value results to be that produce the debonding onset (cycles n°8 in Figure 7.5) The computed compliance over debonding length fitting curve (7.1) allowed to estimate the debonding length increment Δa for each of the compliance intervals experimentally defined. In Table 7.3, the debonding length a_i , for each cycle interested by the debonding, the correspondent compliance C_i and the maximum load value P_i are reported.

As extensively discussed in 6.4.3, the first group of cycles were not

Table 7.3: Debonding length a_i , compliance C_i and maximum load P_i for the load cycles i interested by the debonding.

i	8	9	10	11	12	13	14
$a_i[\mu m]$	0.0712	0.4622	0.8635	1.0855	1.1973	1.2803	1.4288
$C_i[\mu m/\mu N]$	$7.698e^{-4}$	$8.572e^{-4}$	$9.915e^{-4}$	$1.124e^{-3}$	$1.243e^{-3}$	$1.366e^{-3}$	$1.523e^{-3}$
$P_i[\mu N]$	278	262	241	226	228	228	220

considered and the energy release rate was calculated starting from the eighth cycle as. On the base of these presented data the energy release rate was calculated as exposed in equation (6.11). The resulting energy release rate values, for the seven couples of considered subsequent increments, are here reported in Figure 7.6. It can be seen, in the early debonding propagation phase, the energy release rate G linearly rise with the debonding advancement a .

**Figure 7.6:** Energy release rate G over debonding length a dispersion plot with a third order polynomial fitting.

Then, in the last phase of damage propagation, the G values tend toward a finite value. This upper limit for the energy release rate, is close to the value of $10\mu N/\mu m$. Since the load cycles, corresponding to this limit value, results to be those with the most stable propagation in terms of load vs depth curve, the found limit value was considered as the interface toughness. So that:

$$G_c \simeq 10[\mu N/\mu m]$$

Chapter 8

Conclusions and future work

8.1 Achievements

In the light of the presented methodologies and related results, the main achievements of the present dissertation are represented by a couple of experimental-numerical and experimental-analytical strategies for the identification of the fibre to matrix interface properties in a UD FRP. The proposed methodologies were implemented and validated on a laminate made of the *IM7-8552* carbon/epoxy unidirectional pre-impregnated skins.

An original experimental approach for the UD composites interface testing was proposed. A series of micro-cantilever specimens were carved on the laminate cross-section and tested to induce two different interface failure typology. To the best of the author's knowledge, this represents the first attempt of this approach on a continuous fibres polymeric composite, for the interface characterization. The experimental campaigns were supported by numerical simulations reproducing the testing conditions. The models were validated on the base of the experimental evidences and were adopted to identify the fibre to matrix interface properties. The validated models also allow to investigate the effectiveness of the proposed experimental approach

in consistently assess the interface characterization. The results confirmed the proposed methods properly isolate the interface debonding phenomenon and both an opening and a sliding loads can be almost independently induced at the interface.

An analytical framework to the problem was also proposed and verified on the base of the validated numerical model results. The timoshenko beam elastic theory demonstrated to properly address to the problem, once appropriately adapted. The proposed modifications allowed to take into account the presence of two deeply different materials constituting the specimen as well as the strongly anisotropic response of one of them. On this background an analytical procedure for the interface properties calculation was proposed. Starting from the experimental results, it allows to rapidly define the damage initiation strength and the interface toughness. To achieve this result a series of numerical procedures were adopted to tune a transfer function relating the whole specimen compliance to the debonding length advancement. The described procedure outcomes resulted perfectly aligned with the numerical findings, in terms of both strength and toughness of the interface.

8.2 Conclusions

Each of the proposed methods distinctly provides the interface properties when the interface is loaded in mode I (opening) and mode II (sliding). In Table 8.1, a comparison between the interface properties calculated by the author and the literature available data for the same combination of resin and fibre, proposed by *Rueda* [2], is reported.

Table 8.1: Identified and literature available [2] cohesive interface properties comparison.

	t_n^0 [MPa]	$t_s^0 = t_v^0$ [MPa]	G_{Ic} [J/m ²]	$G_{IIc} = G_{IIIc}$ [J/m ²]
Literature	49	74	2	100
Identified	100	135	11	100

It can be seen the calculated strengths, independently by the mode, results to be doubled if compared to the literature values. Also the toughness calculated in mode I results to be much higher than the literature one. On the contrary exactly the same value of toughness resulted for the mode II. As extensively discussed in the introduction - section 1.6.2, the mode II properties determination was already investigated in literature, through both micro-scale and macro-scale testing methods. On the contrary no consolidated experimental procedures are available to date for mode I. Thus the interface properties in opening are conventionally extrapolated in proportion to the mode II results. Assuming the degree of proportionality between the properties in the two modes, is the same as commonly found for macro-scale debonding and delamination tests [2, 16, 20]. This is to date neither certain nor provable and also it does not consider the scale effect. Particularly since, as comprehensively analysed by *Ast et al.* in their work of review [54], both the stress and toughness properties results to be a scale dependent quantity.

The reason why the methodologies proposed in the present dissertation, provides quite different results to those available in literature, can be explained by considering both the scale and the typology of the tests. The lower values of literature interface strength and toughness could results due to the presence of parasitic stresses and stress concentration effect, extensively discussed in the introduction and characteristic of the experimental methods adopted in literature.

8.3 Future work

The discussed achievements represent, of course, the preliminary results of a long and thorough study needed to confirm and consolidate the proposed method for the UD FRP interface characterization. They confirm the interface tightness is a complex phenomenon and show the chance it was on several scales. The effectiveness of the proposed ex-

perimental methods have to be proven on different matrix and fibres combinations as well as on different curing processes interesting the same FRP. Also the presence of other energy dissipation phenomena such as plasticity or severe matrix crack propagation needs to be deepened and quantified respect to the measured properties. Should this produce results encouraging and consistent with what is presented in the present dissertation, the proposed analytical-experimental procedure could be refined and proposed as both a quantitative and qualitative standard for the characterisation of fiber to matrix interfaces in polymer composites.

Bibliography

- [1] Rachid Hsissou et al. “Polymer composite materials: A comprehensive review”. In: *Composite structures* 262 (2021), p. 113640.
- [2] Mario Rueda Ruiz. “Experimental and computational micromechanics of fibre-reinforced polymer composites at high strain rates”. PhD thesis. Department of Material Science, Higher Technical School of Civil Engineers (Universidad Politécnica de Madrid), 2021.
- [3] Tushar Kanti Das, Prosenjit Ghosh, and Narayan Ch Das. “Preparation, development, outcomes, and application versatility of carbon fiber-based polymer composites: a review”. In: *Advanced Composites and Hybrid Materials* 2.2 (2019), pp. 214–233.
- [4] Christos Kassapoglou. *Design and analysis of composite structures: with applications to aerospace structures*. John Wiley & Sons, 2013.
- [5] Morten G Ostergaard et al. “Virtual testing of aircraft structures”. In: *CEAS Aeronautical Journal* 1.1 (2011), pp. 83–103.
- [6] Javier LLorca et al. “Multiscale modeling of composite materials: a roadmap towards virtual testing”. In: *Advanced materials* 23.44 (2011), pp. 5130–5147.
- [7] C González et al. “Structural composites for multifunctional applications: Current challenges and future trends”. In: *Progress in Materials Science* 89 (2017), pp. 194–251.

-
- [8] CS Lopes et al. “Multiscale virtual testing: the roadmap to efficient design of composites for damage resistance and tolerance”. In: *CEAS Aeronautical Journal* 7.4 (2016), pp. 607–619.
- [9] Leon Mishnaevsky Jr and Povl Brøndsted. “Micromechanical modeling of damage and fracture of unidirectional fiber reinforced composites: A review”. In: *Computational Materials Science* 44.4 (2009), pp. 1351–1359.
- [10] B Fiedler et al. “Failure behavior of an epoxy matrix under different kinds of static loading”. In: *Composites Science and Technology* 61.11 (2001), pp. 1615–1624.
- [11] AR Melro et al. “Micromechanical analysis of polymer composites reinforced by unidirectional fibres: Part II–Micromechanical analyses”. In: *International Journal of Solids and Structures* 50.11–12 (2013), pp. 1906–1915.
- [12] Lei Yang et al. “Microscopic failure mechanisms of fiber-reinforced polymer composites under transverse tension and compression”. In: *Composites Science and Technology* 72.15 (2012), pp. 1818–1825.
- [13] Danial Ashouri Vajari et al. “A numerical study of the influence of microvoids in the transverse mechanical response of unidirectional composites”. In: *Composites Science and Technology* 97 (2014), pp. 46–54.
- [14] Daniel Charles Drucker and William Prager. “Soil mechanics and plastic analysis or limit design”. In: *Quarterly of applied mathematics* 10.2 (1952), pp. 157–165.
- [15] Joseph F Labuz and Arno Zang. “Mohr–Coulomb failure criterion”. In: *Rock mechanics and rock engineering* 45.6 (2012), pp. 975–979.

-
- [16] F Naya et al. “Computational micromechanics of the transverse and shear behavior of unidirectional fiber reinforced polymers including environmental effects”. In: *Composites Part A: Applied Science and Manufacturing* 92 (2017), pp. 146–157.
- [17] M Herráez et al. “Computational micromechanics model for the analysis of fiber kinking in unidirectional fiber-reinforced polymers”. In: *Mechanics of Materials* 142 (2020), p. 103299.
- [18] TJ Vaughan and CT McCarthy. “Micromechanical modelling of the transverse damage behaviour in fibre reinforced composites”. In: *Composites Science and Technology* 71.3 (2011), pp. 388–396.
- [19] Carlos González and Javier LLorca. “Mechanical behavior of unidirectional fiber-reinforced polymers under transverse compression: Microscopic mechanisms and modeling”. In: *Composites Science and Technology* 67.13 (2007), pp. 2795–2806.
- [20] Fernando Naya Montans. “Prediction of mechanical properties of unidirectional FRP plies at different environmental conditions by means of computational micromechanics”. PhD thesis. Department of Material Science, Higher Technical School of Civil Engineers (Universidad Politécnica de Madrid), 2017.
- [21] Essam Totry et al. “Mechanisms of shear deformation in fiber-reinforced polymers: experiments and simulations”. In: *International journal of fracture* 158.2 (2009), pp. 197–209.
- [22] Essam Totry et al. “Effect of fiber, matrix and interface properties on the in-plane shear deformation of carbon-fiber reinforced composites”. In: *Composites Science and Technology* 70.6 (2010), pp. 970–980.
- [23] L Casado. “Experimental and computational micromechanical study of fiber-reinforced polymers”. PhD thesis. PhD thesis, Universidad Polite “cnica de Madrid, 2011.

-
- [24] JDH Hughes. “The carbon fibre/epoxy interface—a review”. In: *Composites Science and Technology* 41.1 (1991), pp. 13–45.
- [25] LT Drzal. “The role of the fiber-matrix interphase on composite properties”. In: *Vacuum* 41.7-9 (1990), pp. 1615–1618.
- [26] Serge Zhandarov and Edith Mäder. “Characterization of fiber/matrix interface strength: applicability of different tests, approaches and parameters”. In: *Composites Science and Technology* 65.1 (2005), pp. 149–160.
- [27] Jun Koyanagi et al. “Time and temperature dependence of carbon/epoxy interface strength”. In: *Composites Science and Technology* 70.9 (2010), pp. 1395–1400.
- [28] Stephan Schönen et al. “Insight into single-fiber push-out test of tungsten fiber-reinforced tungsten”. In: *Composite Interfaces* 26.2 (2019), pp. 107–126.
- [29] X-F Zhou, HD Wagner, and SR Nutt. “Interfacial properties of polymer composites measured by push-out and fragmentation tests”. In: *Composites Part A: Applied Science and Manufacturing* 32.11 (2001), pp. 1543–1551.
- [30] E Mäder et al. “Characterisation of the interfacial bond strength between glass fibre and epoxy resin using the pull-out and push-out techniques”. In: *Advanced Composites Letters* 9.3 (2000), p. 096369350000900304.
- [31] Ronald J Kerans and Triplicane A Parthasarathy. “Theoretical analysis of the fiber pullout and pushout tests”. In: *Journal of the American Ceramic Society* 74.7 (1991), pp. 1585–1596.
- [32] Liu Yang and JL Thomason. “Interface strength in glass fibre-polypropylene measured using the fibre pull-out and microbond methods”. In: *Composites Part A: Applied Science and Manufacturing* 41.9 (2010), pp. 1077–1083.

-
- [33] Subramani Sockalingam and Gaurav Nilakantan. “Fiber-matrix interface characterization through the microbond test”. In: *International Journal of Aeronautical and Space Sciences* 13.3 (2012), pp. 282–295.
- [34] Anthony Kelly and amd WR Tyson. “Tensile properties of fibre-reinforced metals: copper/tungsten and copper/molybdenum”. In: *Journal of the Mechanics and Physics of Solids* 13.6 (1965), pp. 329–350.
- [35] William A Curtin. “Theory of mechanical properties of ceramic-matrix composites”. In: *Journal of the American Ceramic Society* 74.11 (1991), pp. 2837–2845.
- [36] Jun Koyanagi et al. “Time-dependent reduction of tensile strength caused by interfacial degradation under constant strain duration in UD-CFRP”. In: *Journal of composite materials* 41.25 (2007), pp. 3007–3026.
- [37] Alfredo Balacó de Morais. “Prediction of the longitudinal tensile strength of polymer matrix composites”. In: *Composites Science and Technology* 66.15 (2006), pp. 2990–2996.
- [38] D Gary Harlow and S Leigh Phoenix. “The chain-of-bundles probability model for the strength of fibrous materials I: analysis and conjectures”. In: *Journal of composite materials* 12.2 (1978), pp. 195–214.
- [39] D Gary Harlow and S Leigh Phoenix. “The chain-of-bundles probability model for the strength of fibrous materials II: a numerical study of convergence”. In: *Journal of composite materials* 12.3 (1978), pp. 314–334.
- [40] William A Curtin and N Takeda. “Tensile strength of fiber-reinforced composites: I. Model and effects of local fiber geometry”. In: *Journal of composite materials* 32.22 (1998), pp. 2042–2059.

-
- [41] William A Curtin and N Takeda. “Tensile strength of fiber-reinforced composites: II. Application to polymer matrix composites”. In: *Journal of Composite Materials* 32.22 (1998), pp. 2060–2081.
- [42] Sung Kyu Ha, Kyo Kook Jin, and Yuanchen Huang. “Micro-mechanics of failure (MMF) for continuous fiber reinforced composites”. In: *Journal of Composite materials* 42.18 (2008), pp. 1873–1895.
- [43] Jun Koyanagi et al. “A comprehensive model for determining tensile strengths of various unidirectional composites”. In: *Journal of Composite Materials* 43.18 (2009), pp. 1901–1914.
- [44] Alexander Straub, Michael Slivka, and Peter Schwartz. “A study of the effects of time and temperature on the fiber/matrix interface strength using the microbond test”. In: *Composites science and technology* 57.8 (1997), pp. 991–994.
- [45] Jun Koyanagi and Shinji Ogihara. “Temperature dependence of glass fiber/epoxy interface normal strength examined by a cruciform specimen method”. In: *Composites Part B: Engineering* 42.6 (2011), pp. 1492–1496.
- [46] Dongil Son, Jeung-hyun Jeong, and Dongil Kwon. “Film-thickness considerations in microcantilever-beam test in measuring mechanical properties of metal thin film”. In: *Thin solid films* 437.1-2 (2003), pp. 182–187.
- [47] Guillaume Colas et al. “Strength measurement and rupture mechanisms of a micron thick nanocrystalline MoS₂ coating using AFM based micro-bending tests”. In: *Journal of the Mechanics and Physics of Solids* 128 (2019), pp. 151–161.
- [48] David EJ Armstrong, Angus J Wilkinson, and Steve G Roberts. “Measuring anisotropy in Young’s modulus of copper using mi-

- crocantilever testing”. In: *Journal of materials research* 24.11 (2009), pp. 3268–3276.
- [49] Jae-Hoon Choi et al. “Micro-cantilever bending tests for understanding size effect in gradient elasticity”. In: *Materials & Design* 214 (2022), p. 110398.
- [50] J Schaufler et al. “Determination of the interfacial strength and fracture toughness of aC: H coatings by in-situ microcantilever bending”. In: *Thin Solid Films* 522 (2012), pp. 480–484.
- [51] Abaqus User Manual. “Abaqus theory guide”. In: *Version 6.14* (2014), p. 281.
- [52] Shinji Ogihara and Jun Koyanagi. “Investigation of combined stress state failure criterion for glass fiber/epoxy interface by the cruciform specimen method”. In: *Composites Science and Technology* 70.1 (2010), pp. 143–150.
- [53] ASTM Standard et al. “Standard test method for measurement of fracture toughness”. In: *ASTM, E1820-01* (2001), pp. 1–46.
- [54] J. Ast et al. “A review of experimental approaches to fracture toughness evaluation at the micro-scale”. In: *Materials & Design* 173 (2019), p. 107762. ISSN: 0264-1275. DOI: <https://doi.org/10.1016/j.matdes.2019.107762>.

List of Figures

1.1	Evolution of structural composite materials applications in commercial and military aircraft and rotorcraft [2].	6
1.2	Comparison of stress-strain curves for the most common reinforcement fibres and steels with HS and HM carbon fibres [3].	8
1.3	Building block diagram scheme for aerospace composite structures certification [2].	13
1.4	Bottom-up multiscale approach numerical modelling and virtual testing building block diagram	15
1.5	UD FRP failure surface scheme for each of the possible loading configuration [2].	17
1.6	21
1.7	Push-in test interface stress field schematic during the elastic pre-debonding phase [28].	22
1.8	Optical image of a carbon fibre and epoxy resin microbond specimen (a) and SEM image of the tested specimen, with the knife print on the resin highlighted (b).	24
1.9	Fragmentation test at different stages and critical length scheme.	26
1.10	Cruciform specimen scheme.	28
1.11	Graphical comparison between experimental and GLT predicted strengths for several UD composites (a) and list of investigated UD composite (b) [43].	29

1.12	Unidirectional composite strength as a function of interfacial shear strength (a) and as a combination of interfacial shear strength and matrix strength (b) [43]. . .	31
2.1	Literature SEM image of a MoS ₂ micro-cantilever beam, into the inset a beam cross section detail is reported [47].	37
2.2	Schematic representation of a dual beam equipment . .	41
2.3	Schematic representation of milling patterns and cut outcomes for Step I (a), Step II (b) and fully processed micro-cantilever sample (c) with fibre-matrix interface highlighted.	44
2.4	SEM image of a ready to be tested micro-cantilever beam	45
2.5	SEM image of C2.3 specimen with the notch highlighted	47
2.6	Schematic representation of mode II test configuration (a), with flat indenter tip and shear stress at interface, and mode I test (b) with cube corner indenter tip and bending stress distribution.	48
3.1	C1.3 mode I tested specimens, with interface debonded highlighted (a) and the respective experimental load vs depth curve (b)	52
3.2	C3.2 mode I tested notched specimens, with parasite matrix crack and cube corner indentation highlighted (a) and the respective experimental load vs depth curve (b)	53
3.3	SEM image of C3.4 specimen with whole debonding front kinked and propagated into the matrix.	54
3.4	Average and standard deviation of applied load over depth, for unnotched (a) and notched (b) specimens, tested in mode I.	55
3.5	Normalized with respect to the cross-section area load over depth, for the unnotched and notched specimens tested in mode I.	56

3.6	C6.4 tested specimen with matrix crack highlighted. . .	57
3.7	Average and standard deviation of applied load over depth for C6 specimens made of matrix.	58
3.8	C5.1 specimen failed mode II test, conducted adopting the cube corner indenter tip positioned close to the fibre-matrix interface.	59
3.9	C5.1 specimen load over depth curve, with highlighted the the cyclic loading ramps (black lines) and the whole tests stiffness K and K'	60
3.10	C5.2 to C5.4 specimen test results in term of load over depth curve, the tests ere conducted by adopting cube-corner tip and applying the load as closer to the interface as possible.	60
3.11	Average and standard deviation of load over depth for C4 specimens group, tested in mode II and adopting the flat indenter tip.	61
3.12	SEM image of mode II tested C4.11 specimen, the complete micro beam detachment is visible (a) as well as a detail of the debonding surface (b).	62
4.1	65
4.2	Schematic representation of a 2D master-slave surface contact interaction.	68
4.3	Computational domain with an internal interface. . . .	71
4.4	FE problem discretization (a), with interface elements and cohesive interaction stiffness K , and schematization of two couples of nodes experiencing a cohesive contact (b) with the relative displacement components δ_n and δ_s	72
4.5	Traction-separation laws for normal mode I and the shear mode II.	74

4.6	Graphical representation of cohesive response mixing mode, with stress governed initiation locus and BK energetic damage evolution highlighted.	77
5.1	Numerical and experimental matrix carved micro-cantilever specimen response in pre cracking elastic regime.	83
5.2	Numerical and experimental micro-cantilever specimen response under initial elastic deformation regime.	84
5.3	AFM topographic image of the C1.9 specimen surface, with the microscope pointer highlighted.	86
5.4	Schematic representation of the load application point moving procedure.	86
5.5	Effect of punch position error on the whole specimen response, in term of load vs depth curves for experimental C4 tests group and the numerical results related to the nominal punch position and three different positioning errors d.	87
5.6	Numerical mode I load vs depth curves for interface parameters from P1 till P5 (a) and mode II for interface parameters from P2 till P5 (b)	90
5.7	Numerical and experimental results comparison for C1 mode I (a) and C4 mode II (b) testing conditions.	91
5.8	Cohesive damage progression over the load vs depth curves for mode I (a) and mode II (b) numerical simulations.	93
5.9	Selected control nodes for damage contribution identification in both mode I and mode II load configurations.	95
5.10	S-84 node cohesive stresses and displacements evolution over simulation time (a) together with the normal stress (b) and shear stress (c) over the corresponding displacement.	96

5.11	Example of load over depth curve for two block in contact with a frictional contact enable, with a cohesive contact and with both friction and cohesive enabled. . .	99
5.12	100
6.1	Micro-cantilever beam elastic scheme with elastic constraints (a) and a section side view of the micro beam with stress distribution and interface positioning (b) . .	104
6.2	The three different modes of interface failure, discerned according to the direction of the applied load with respect to the interface plane.	107
6.3	Schematization of the numerical deflection line identification procedure (a) and $U2[\mu m]$ displacements contour plot (b)	110
6.4	Interface section displacement fields Uy (a) and Uz (b) reported in $[\mu m]$	111
6.5	Through crack subjected to a propagation.	114
6.6	Energy variation with corresponding crack length . . .	115
6.7	Load-displacement curves for a crack increment da . . .	116
6.8	Schematization of the experimental stiffness identification with the debonding cyclic progression.	118
6.9	Schematization of the model with bonded and untied interface region highlighted (a) and detail of the debonded region opening effect under load application (b)	119
7.1	Analytical and numerical fibre micro-beam deflection curve comparison.	120
7.2	Analytical and numerical micro-cantilever specimen deflection curve comparison.	121
7.3	Average load vs depth curve for the mode I tested specimens , together with its discrete derivative and the mean value of the initial range where this last is constant. . .	122

7.4	Numerically calculated compliance vs debonding length data and cubic polynomial fitting curve, together with the R-squared value.	123
7.5	Experimental specimen compliance over the load cycles, together with the average compliance value	125
7.6	Energy release rate G over debonding length a dispersion plot with a third order polynomial fitting.	126

List of Tables

2.1	<i>IM7</i> fibres and <i>8552</i> resin estimated elastic properties.	40
2.2	FIB parameters for <i>IM7-8552</i> milling process.	42
2.3	Cross section geometrical and cantilever length measurements, reported as average value μ and standard deviation Σ for each of the performed experimental preparation campaigns.	46
2.4	micro-cantilever test groups	49
4.1	Computational problem size	66
5.1	Matrix block dimensions	81
5.2	Cohesive interface properties sets.	89
5.3	Contribution of opening and shear damage to the total interface damage in mode II tests for S-84 node.	96
5.4	Contribution of the opening and shear damage to the total interface damage in mode I tests for N-68, N-97 and N-562 nodes.	97
6.1	Continuum mechanics fundamental relations and cantilever beam problem boundary conditions	105
6.2	Applied load P and resulting displacement	111
7.1	Analytical adapted solution lumped stiffnesses.	121
7.2	Compliance vs debonding length polynomial fitting coefficients.	124

7.3	Debonding length a_i , compliance C_i and maximum load P_i for the load cycles i interested by the debonding. . .	126
8.1	Identified and literature available [2] cohesive interface properties comparison.	129